UNIVERSITY OF OKLAHOMA

GRADUATE COLLEGE

THE USE OF REMOTE SENSING AND EDDY COVARIANCE TECHNOLOGIES TO CHARACTERIZE CROPLAND, DROUGHT AND LAND MANAGEMENTS AND THEIR IMPACTS ON ECOSYSTEM DYNAMICS

A DISSERTATION

SUBMITTED TO THE GRADUATE FACULTY

in partial fulfillment of the requirements for the

Degree of

DOCTOR OF PHILOSOPHY

By

YUTING ZHOU
Norman, Oklahoma
2017

Downloaded from SHAREOK. Persistent Handle URL: https://hdl.handle.net/11244/50829

THE USE OF REMOTE SENSING AND EDDY COVARIANCE TECHNOLOGIES TO CHARACTERIZE CROPLAND, DROUGHT AND LAND MANAGEMENTS AND THEIR IMPACTS ON ECOSYSTEM DYNAMICS

A DISSERTATION APPROVED FOR THE
DEPARTMENT OF MICROBIOLOGY AND PLANT BIOLOGY

BY

_____
Dr. Xiangming Xiao, Chair

_____
Dr. Jeffrey Basara

_____
Dr. Yiqi Luo

_____
Dr. Jean Steiner

_____
Dr. Heather McCarthy

© Copyright by YUTING ZHOU 2017
All Rights Reserved.

This dissertation is dedicated to my wife Shengfang Ma, to my daughter Lisa M Zhou, to my parents and parents-in-law, for their unconditional love and support.

Acknowledgements

This dissertation would not have been possible without the guidance and the support of several individuals who in one way or another contributed and extended their valuable assistance in the preparation and completion of this study.

I would like to express my thanks and appreciation to my dissertation committee members, Drs. Xiangming Xiao, Jeffrey Basara, Yiqi Luo, Heather McCarthy, and Jean Steiner. I especially want to thank my advisor, Dr. Xiao, for his excellent guidance during my research and study at the University of Oklahoma. His patience and the great way to explaining things clearly and simply helped me during my Ph. D. study. Also my warm and sincere thanks go to other members of my advisory committee, for all advice through the development of my dissertation research.

I extend my heartfelt thanks to my fellow colleagues in the Earth Observation and Modeling Facility group for their help and company during this work. I would also like to thank several members of the crew in the Grazinglands Research Laboratory USDA-ARS, Drs. Prasanna Gowda, Pradeep Wagle, Patrick Starks, James Neel, and Brain Northup, for their help in field sampling and instrument maintenance.

I owe my loving thanks to my family; without their support, none of this would have been possible.

Last but certainly not least, I gratefully acknowledge research grants that made my Ph.D. work possible. I would like to express my full appreciation to the staffs of the Center for Spatial Analysis, especially Ms. Melissa Scott, and Ms. Leah Nash for their assistance.

Table of Contents

Acknowledgements iv

Table of Contents v

List of Tables x

List of Figures xi

Abstract xix

Chapter 1: Introduction 1

1.1 Research background 1

1.2 Overall research objectives 4

1.3 Organization of the dissertation 4

1.4 List of Publications from the Dissertation 5

Chapter 2: Mapping paddy rice planting area in rice-wetland coexistent areas through analysis of Landsat 8 OLI and MODIS images 7

Abstract 7

2.1 Introduction 8

2.2 Materials and methods 10

2.2.1 Study area 10

2.2.2 Data 12

2.2.3 Temperature-defined plant growing season 17

2.2.4 Phenology-based algorithm to identify paddy rice 20

2.2.5 Accuracy assessment 24

2.2.6 Comparison with other paddy rice datasets 25

2.3 Results 25

2.3.1 Spectral signature of major land cover types during and after paddy rice flooding stage 25
2.3.2 Paddy rice map of the Panjin Plain from Landsat 8 OLI data 27
2.3.3 Validation of the paddy rice map derived from Landsat 8 OLI data 28
2.4 Discussion 29
2.4.1 Advantages of the pixel- and phenology-based algorithm 29
2.4.2 Comparison of Landsat 8 OLI-derived rice map with other products 30
2.4.3 Sources of uncertainty and limitation 33
2.4.4 Future work and challenges 34
2.5 Conclusion 35
Supplementary materials 36
Chapter 3: Examining the short-term impacts of diverse management practices on plant phenology and carbon fluxes of Old World bluestems pasture 43
Abstract 43
3.1 Introduction 44
3.2 Materials and methods 47
3.2.1. Study site description 47
3.2.2. Eddy flux tower site and EC data processing 48
3.2.3. PhenoCam images and greenness index 50
3.2.4. MODIS images and VIs 51
3.2.5. Landsat images and VIs 52
3.2.6. Vegetation Photosynthesis Model 53
3.2.7. Statistical analysis 54

3.3 Results 55
3.3.1. Canopy dynamics and plant phenology in response to management practices as observed by PhenoCam, Landsat, and MODIS images 55
3.3.2. Carbon fluxes in response to management practices as observed by eddy flux tower 60
3.3.3. GPP in response to management practices and disturbance as estimated by VPM 63
3.4 Discussion 66
3.4.1. Necessity of utilizing multiple observations to study the impacts of management practices on plant phenology and carbon fluxes 66
3.4.2. Complexity of assessing the impacts of management practices 68
3.4.3. Importance of the examination of EC footprint 69
3.4.4. Implication and future steps 70
3.5 Conclusion 72
Chapter 4: Quantifying agricultural drought in tallgrass prairie region in the U.S. Southern Great Plains through analysis of a water-related vegetation index from MODIS images 74
Abstract 74
4.1 Introduction 75
4.2 Materials and methods 80
4.2.1 Study area 80
4.2.2 Data 81
4.2.3 Algorithms for mapping agricultural drought 83

4.2.4 Agricultural drought dynamics and comparison with other drought products 85
4.2.5 The relationship between precipitation and LSWI-based drought duration 86
4.3. Results 87
4.3.1 LSWI-based drought maps and comparison with ESI, VegDRI, and USDM 87
4.3.2 LSWI-based drought duration patterns in the SGP 91
4.3.3 Relationship between LSWI-based drought duration and precipitation..... 93
4.3.4 Validation of LSWI-based drought against forage production 96
4.4. Discussion..... 97
4.4.1 Comparison of the LSWI-based drought algorithm with other drought products 97
4.4.2 Importance of precipitation amount and distribution in the year 98
4.4.3 Future work and challenges..... 100
4.5. Conclusion..... 102
Supplementary materials 103
Chapter 5: Consecutive years of agricultural drought and heatwave drove the large losses of cattle production in the U.S. Southern Great Plains 109
Abstract..... 109
5.1 Introduction 110
5.2 Materials and methods..... 112
5.2.1 Study area 112

5.2.2. Data 113
5.2.3. Statistical analysis 115
5.3 Results 115
5.3.1 Spatial distribution and annual dynamics of cattle production in the SGP 115
5.3.2. Drought and heatwave conditions during 2000-2015 117
5.3.3. Dynamics of animal feed production for cattle 119
5.3.4. Dynamics of the cattle market 120
5.3.5. Statistical models between cattle production and driving factors over years 121
5.4 Discussion 123
5.4.1. Impacts of drought and heatwave on the cattle production 123
5.4.2. Model the dynamics of the cattle production 124
5.4.3. Other factors affecting the cattle production beside of droughts 125
5.5 Conclusion 127
Chapter 6: Conclusions and perspectives 128
References 131

List of Tables

Table 2.1. Landsat 8 images used in this study. Two tiles (Path120/Row31 and Path120/Row32) are combined to cover the study area. The cloud cover information of each image is given by the metadata. 12

Table 2.2. Phenology stages of major plants in the Panjin Plain, Liaoning Province, China. The phenology data of paddy rice, soybean, and corn were provided by China Meteorological Data Sharing Service System (http://cdc.cma.gov.cn/home.do). The phenology stages of reed wetland and deciduous forest were extracted from (Li et al. 2006) and (Yu and Zhuang 2006), respectively. 15

Table 2.3. The confusion matrix between the $Rice_{Landsat}$ in the Panjin Plain and ROIs derived from geo-reference field photos in the field survey and high resolution images in Google Earth..... 29

Table S2.1. The confusion matrix between the paddy rice map derived using ISODATA classification and ROSs from geo-reference field photos in the field survey and high resolution images in Google Earth. 40

Table S2.2. The confusion matrix between the paddy rice map derived using ISODATA classification and ROSs from geo-reference field photos in the field survey and high resolution images in Google Earth. 42

Table 3.1. Event based GPP statistics for iGOS W and iGOS WN 65

Table 5.1. Results from stepwise linear regression models for each state 121

Table 5.2. Livestock water withdrawals in 2005 and 2010. Values may not sum to totals because of independent rounding. 126

List of Figures

Figure 1.1. The research background of the dissertation..... 1

Figure 2.1. (a) Location of the field survey sites in the Panjin Plain, Liaoning Province, China. The total number of sites for paddy rice, reed wetland, and others (corn, soybean, water body etc.) were 86, 21, and 34. (b) Landsat tiles (path/row) for the study area and its location in Liaoning province. (P1), (P2), and (P3) are the photos that show the paddy rice, reed wetland and corn fields. 11

Figure 2.2. Daily mean and minimum temperature, precipitation and night time land surface temperature (LST_{night}) in the Panjin Plain. Temperature and precipitation data is from the weather station located at Jin Zhou City (41.08 ºN, 121.07 ºE) and collect collected from China Meteorological Data Sharing Service System (http://www.escience.gov.cn/metdata/page/index.html). LST_{night} data is from MOD11A2 product for the pixel where the weather station is located in. The two dash lines denote the 0 ºC and 10 ºC. The weather station is not in the study area but is the closest one with data available. 18

Figure 2.3. Spatial distribution of temperature-defined plant growing season as delineated by LST_{night} in the Panjin Plain derived from MOD11A2 in 2013. (a) The first date with LST_{night}>=0 ºC; (b) the first date with LST_{night}>=10 ºC; (c) the end date with LST_{night}>=0 ºC; (d) the end date with LST_{night}>=10 ºC. 19

Figure 2.4 The seasonal dynamics of NDVI, EVI, and LSWI of major land cover types from MOD09A1 product in 2013 (a) a paddy rice site (41.0437 ºN, 122.2137 ºE), (b) a reed wetland site (41.2127 ºN, 121.7095.ºE), (c) a corn site (41.1159 ºN, 121.6550 ºE), and (d) a forest site (41.5279 ºN, 121.6303 ºE). All sites were selected according to the

field sampling sites and were representatives of major land cover types except forest site was selected based on Google Earth image. 21

Figure 2.5. The seasonal dynamics of NDVI, EVI, and LSWI from both MODIS and Landsat 8 OLI images at a paddy rice site and a reed wetland site, which were also used in Figure 4. MODIS vegetation indices were gap-filled values while Landsat 8 OLI vegetation indices only included good observations used in this study. Black rectangles indicated the flooding periods from Landsat vegetation indices. 23

Figure 2.6. A schematic diagram illustrating the implementation of the algorithm for mapping of paddy rice in the Panjin Plain from multi-temporal Landsat 8 OLI data and MODIS data. 24

Figure 2.7. The 2-D scatter plots of vegetation indices and the difference between two vegetation indices from the Landsat 8 OLI data during the paddy rice flooding period (upper panels)and the tillering period (below panels). The color density represents the number of pixels. (a) Landsat images are false composite displayed with red (SWIR), green (NIR) and blue (red), (b) NDVI versus LSWI-NDVI, (c) EVI versus LSWI-EVI, (d) LSWI versus LSWI-NDVI, and (e) LSWI versus LSWI-EVI. 26

Figure 2.8. The resultant paddy rice map of the Panjin Plain derived from the Landsat 8 OLI data in 2013 at 30-m spatial resolution. Field survey sites were included for reference. 28

Figure 2.9. Paddy rice maps derived from (a) the $Rice_{Landsat}$ and (b) the $Rice_{NLCD}$ at the 1-km spatial resolution (c) the comparison between the $Rice_{Landsat}$ and the $Rice_{NLCD}$. .. 31

Figure 2.10. The quantitative comparison between paddy rice maps derived from the $Rice_{Landsat}$ and the $Rice_{NLCD}$ at (a) county level and (b) pixel level. 32

Figure S2.1 False composite displayed Landsat OLI image in DOY 159 (6/8/2013) with red (SWIR), green (NIR) and blue (red). 38
Figure S2.2 The resultant paddy rice map of the Panjin Plain derived from Landsat OLI data in DOY 159 (the paddy rice flooding period) using ISODATA. 39
Figure S2.3 The resultant paddy rice map of the Panjin Plain derived from Landsat OLI data in DOY 159 (the paddy rice flooding period) using Support Vector Machine (SVM). 41
Figure 3.1. Location of flux tower site and overlapping with MODIS pixels. Location of the flux tower site is marked as red point and labeled. Red rectangle is the boundary of the study field. Green diamonds are boundaries of MODIS pixels. 47
Figure 3.2. Seasonal dynamics of photosynthetically active radiation (PAR), precipitation (Precip), air temperature (Tair), and soil water content (SWC) at 25 cm observed at the flux tower site/nearby Mesonet site. Each data point represents daily average. 49
Figure 3.3. PhenoCam images showing management practices and phenology of grassland. The black rectangle in panel e shows the region of interest (ROI) used to calculated GCC values. 56
Figure 3.4. Management practices, climate events, and plant phenology in the field. The plant phenology was delineated through interpreting individual time series PhenoCam images. 56
Figure 3.5. Daily GCC values from PhenoCam images. 57
Figure 3.6. Landsat images of the study area in different periods. Location of flux tower site and boundaries of MODIS pixels are also shown. 58

Figure 3.7. MODIS vegetation indices (VIs) for the flux tower located pixel (iGOS W) and its neighbor pixel (iGOS WN). 59
Figure 3.8. Differences in Enhanced Vegetation Index (EVI) and Land Surface Water Index (LSWI) at iGOS WN and iGOS W MODIS pixel derived from MODIS and Landsat images. 60
Figure 3.9. Half-hourly binned diurnal courses of net ecosystem CO_2 exchange (NEE) from May to October 2014 at the iGOS W site. Negative values of NEE indicate net carbon uptake and positive values indicate carbon release by the ecosystem. Each data point is a mean value for the specific time step for the entire month and bars represent standard errors of the means. 61
Figure 3.10. Daily sums of gross primary production (GPP), ecosystem respiration (ER), and net ecosystem CO_2 exchange (NEE) from flux tower in the 2014 growing season. 62
Figure 3.11. (a) Relationship between enhanced vegetation index (EVI) and gross primary production (GPP_{EC}). (b) Comparison between gross primary production (GPP) from VPM simulation and EC measurement (GPP_{VPM_W} and GPP_{EC}). 63
Figure 3.12. Differences in gross primary production (GPP) difference of the flux tower located pixel (iGOS W) and its neighbor pixel (iGOS WN). 65
Figure 3.13. Footprint before and after hay baling. (a) Prior to first baling, (b) after first but before second baling, (c) after second baling. The background images are from Landsat which showed conditions prior to baling, after the first baling, and after the second baling. The circular dots are contribution of flux measurements from different

direction and distance. Colors indicate the frequency of contribution of flux measurements. 70

Figure 4.1. Different timescales of drought, highlighting observables of vegetation water stress expressed as remote sensing proxies. Only the primary factors affecting the remotely sensed vegetation indices are listed. 76

Figure 4.2. Location of the Southern Great Plains (SGP) study area and the coverage of the tallgrass prairie (in the inset). MODIS tile boundaries are indicated as dark lines. The base map shows the 30 year (1981-2010) mean annual precipitation over the region. 80

Figure 4.3. A schematic diagraph of the seasonal dynamics of LST, LSWI, and NDVI during drought and non-drought years for a sample data point is located at 36.556481^{o}N, -98.317713^{o}W. The LST-defined growing season is depicted for the duration of nighttime LST > 5 °C. 84

Figure 4.4. Comparison of LSWI-based drought duration with ESI, VegDRI, and USDM in normal, WGSD, and summer drought years. (a) Summer drought duration and WGSD in 2010, (b) Summer ESI in 2010, (c) Summer VegDRI in 2010, (d) USDM 20100831, (e) Summer drought duration and WGSD in 2011, (f) Summer ESI in 2011, (g) Summer VegDRI in 2011, (h) USDM 20110830, (i) Summer drought duration and WGSD in 2012, (j) Summer ESI in 2012, (k) Summer VegDRI in 2012, (l) USDM 20120828. 88

Figure 4.5. LSWI-based summer drought duration vs. 3-month composite ESI (JJA) in 2012. 90

Figure 4.6. LSWI vs. USDM for the last week of August in 2012. The climate division boundaries are indicated by black polygons. Only pixels classified as tallgrass prairie were plotted. The inset in (b) showed the mean LSWI values in each category (D0, D1, D2, D3, and D4). 91

Figure 4.7. Annual summer drought dynamics in three states (KS, OK, and TX) of the SGP for 2000-2013. 92

Figure 4.8. Areal percentage of the total tallgrass prairie area affected by the whole growing season drought (WGSD) in three states (KS, OK, and TX) of the SGP for 2000-2013. 92

Figure 4.9. Summer drought and WGSD patterns in the SGP for 2000-2013. (a) Mean of summer drought duration for 2000-2013, (b) Standard deviation of summer drought duration, (c) Occurrence of WGSD for 2000-2013. The insert panel shows the frequency distribution of values. 93

Figure 4.10. LSWI-based summer drought duration vs. summer precipitation in (a) 2010, (b) 2011, and (c) 2012. Relative frequency in the legend indicates the ratio of pixels with certain summer precipitation to the total pixels. 94

Figure 4.11. Comparison of summer precipitation anomalies and LSWI anomalies in drought years (2006, 2011, and 2012) at 113 Mesonet stations across OK. 94

Figure 4.12. WGSD vs. annual precipitation in 2011. (a) Distribution of WGSD in 2011, (b) Annual precipitation deviation from the mean (annual anomaly in 2011). The inset in (b) shows the frequency distribution of precipitation deviation. 95

Figure 4.13. Relationship between the WGSD affected area and annual precipitation anomaly. 96

Figure 4.14. Relationship between areas affected by drought and hay production in each state. 96
Figure 4.15. Precipitation distribution in early (March) and peak growing season (June-August) according to rainfall events (%) with different rainfall sizes (25 mm rainfall bin size in the graph). 99
Figure S4.1 Data processing workflow for LSWI-based drought assessment algorithm. 103
Figure S4.2 Annual, early spring, and summer precipitation deviation to the mean. .. 104
Figure S4.3 Drought dynamics in the SGP for 2000-2013 mean. 105
Figure S4.4 LSWI and NDVI vs. VegDRI for the last week of August in 2012. 106
Figure S4.5 Distribution of the annual precipitation deviation from the mean in 2011. 106
Figure S4.6 Standard deviation of summer precipitation during 2000-2013. 107
Figure S4.7 NDVI anomaly in early growing season of 2012 (March-May) relative to the baseline of 2000 - 2011. The inset shows the distribution of area percent of NDVI anomalies. 108
Figure 5.1. A list of major factors affecting cattle production systems 111
Figure 5.2. Mean and standard deviation of all cattle and calves for 2000-2015..... 116
Figure 5.3. Anomalies of all cattle and calves in 2010-2012 116
Figure 5.4. Dynamics of cattle production during 2000-2015 117
Figure 5.5. SPI-12 and ESI-3 in 2010, 2011, and 2012 (Showing US with SGP outlined) 119

Figure 5.6. Dynamics of annual precipitation (Precip), maximum temperature (Tmax), and minimum temperature (Tmin) during 2000-2013..... 119

Figure 5.7. Dynamics of hay production and grain prices during 2000-2015..... 120

Figure 5.8. Dynamics of the market during 2000-2015. (a) Beef price and (b) beef consumption 120

Figure 5.9. Results from the Random Forests for KS (a), OK (b), and TX (c). The graphs show the importance of variables calculated by the Random Forests. Figures in left panels and right panels show the importance of variables from different perspectives. Larger values indicate higher importance. The percent of variance explained (R^2) and mean squared error (MSE) were inserted in the corresponding panels. 122

Figure 5.10. Results from the Random Forests using all the state-years data. 123

Abstract

With the increasing population, human needs more food, fresh water, and other ecosystem services, which burdens the agricultural and natural ecosystems. Under the background of climate change, meeting these human needs becomes more challenging because of increasing temperature, climate extremes, etc. and their interaction with human activities. Thus, it is important to understand the impacts of climate change and human activities on ecosystem dynamics. The land-use and land-cover change, one of the most important human activities, greatly affects the function and dynamics of ecosystems. Drought is one of the most costly natural disasters and imposes wide-ranging impacts on the economy, environment, and society. This dissertation aimed to strengthen the usage of remote sensing and eddy covariance techniques in paddy rice mapping, agricultural drought monitoring, land management effects assessment, and evaluating the impacts of drought on cattle production.

Chapter 2 identified the different flooding/transplanting periods of paddy rice and natural wetlands. The natural wetlands foods earlier and have a shorter duration than paddy rice in the Panjin Plain, a temperate region in China. Using this asynchronous flooding stages, this chapter extracted the paddy rice planting area from the rice-wetland coexistent area using MODIS and Landsat 8 imagery. The comparison and validation tests indicated high accuracy of our paddy rice map.

Chapter 3 quantified the agricultural drought of tallgrass prairie in the SGP using a remotely sensed water-related vegetation index derived from MODIS. The results are comparable to other widely used drought products. The spatial pattern of drought duration was highly correlated with the decreasing precipitation gradient from

east to west. LSWI-based drought depictions are sensitive to both precipitation anomalies from the historical mean and abnormal seasonal precipitation distributions. A comparison with other widely used drought products is made.

Chapter 4 examined the impacts of burning, baling, and grazing on canopy and carbon fluxes in a pasture through integrating PhenoCam images, satellite remote sensing, and eddy covariance data. Landsat images were used to assess the baling area and the trajectory of vegetation recovery. MODIS vegetation indices (VIs) were used in the Vegetation Photosynthesis Model (VPM) to estimate gross primary production (GPP_{VPM}) at a MODIS pixel for the flux tower (baled) site. Multiple datasets allowed studying intra-annual variations caused by various management practices. The larger increase of GPP after large rain in baled grassland (photosynthetically more active vegetation) compensated the reduction in GPP caused by baling. This result indicated that the interaction of management practices with climate is important when studying their impacts on GPP.

Chapter 5 evaluated the impacts of drought on cattle production in the SGP during 2000-2015 use meteorological, remote sensing, and statistical data. The results showed that the consecutive years of drought and high temperatures in 2011 and 2012 dramatically decreased the cattle production in OK and TX. The decrease extent in KS was smaller probably because of the greater accessibility to the groundwater resource. 2011 was a whole year drought in the SGP which decreased the hay production and thus cattle production, while 2012 was a summer drought year in the Corn Belt which increased the corn price and thus cattle production. The Random Forest method performed well and shows the potential in predicting the dynamics of cattle production.

Chapter 1: Introduction

1.1 Research background

With the increasing population, human society needs more food and, fresh water, and other ecosystem services, which burdens the agricultural and natural ecosystems (Beddington et al. 2012; FAO 2013; Godfray et al. 2010). The modification of Earth's terrestrial surface by human activities to meet these human needs is known as land-use and land-cover change (LULCC) (Ellis and Pontius 2007). LULCC greatly affects the function and dynamics of ecosystems at both regional and global scale because of increasing extent, intensity, and rate (Foley et al. 2005; Lambin et al. 2001). Under the background of climate change, meeting human needs becomes more challenging because of increasing temperature (IPCC 2013), more frequent climate extremes (Stocker et al. 2013), etc. and their interaction with human activities (Fig. 1.1).

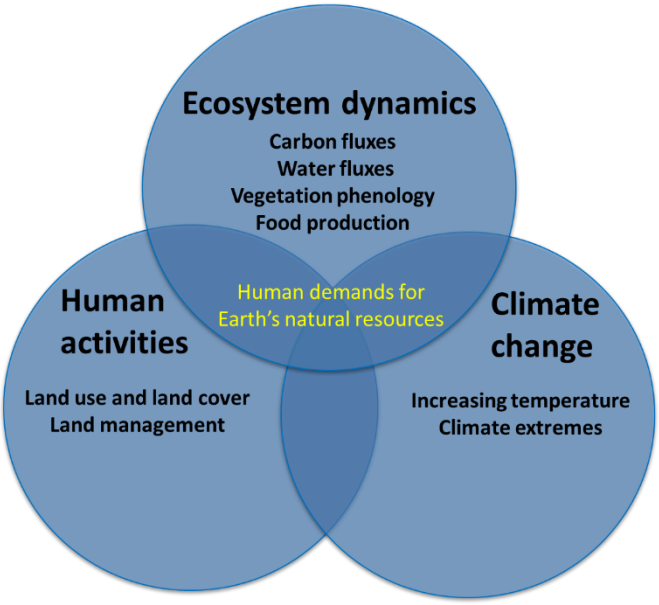


Figure 1.1. The research background of the dissertation.

Cropland ecosystems provide food for humans (FAO 2013). Meanwhile, it also dramatically alters the ecosystem structure and function, and is an important driver of

the ecosystem and environment changes (Ellis and Pontius 2007; Foley et al. 2005). Paddy rice provides the most important staple food for more than half the global population (FAO 2013; Matthews et al. 2001). With the rapid growth in world population, the demand for food (Godfray et al. 2010), especially rice, is increasing, which increases pressure on land, water, and biodiversity. Paddy rice, along with natural wetlands are the largest sources of CH_4 emissions (Stocker et al. 2013; Zhuang et al. 2009). Information on the spatial distribution and temporal dynamics of paddy rice fields is important for the studies of trace gas emissions, management of water resources, and food security (Döll 2002; Xiao et al. 2006; Xiao et al. 2005). An updated and accurate paddy rice map with fine spatial resolution (e.g. 30 m) is vital for policy makers and farmers to understand and balance environmental problems (greenhouse gas emissions and water deficit issues) with rice production.

Since the late 1980s, remote sensing technology has been used for mapping rice areas in addition to paddy rice datasets from agricultural statistics and census approaches (Aselmann and Crutzen 1989; Huke and Huke 1997; Huke 1982; Matthews et al. 1991; Olson 1992). The image-based method (Bachelet 1995; Chen et al. 2011b; Fang 1998; Gilabert and Melia 1990; McCloy et al. 1987; Okamoto and Fukuhara 1996; Rao and Rao 1987; Tennakoon et al. 1992), using visualization and digitalization or pixel clustering, was first utilized to monitor paddy rice fields using optical remote sensing data. However, the image-based method depends highly on the producer's knowledge and the image statistics feature. The pixel-based method, based on pixel statistics and signal detection in each pixel, targets specific feature detection using time

series data. With the increasing temporal and spatial resolutions of satellite data, the use of remote sensing in paddy rice mapping becomes more and more important.

Grassland (both native prairie and planted/introduced pasture) is a major forage source for millions of beef cattle in the Southern Great Plains (SGP: Kansas, Oklahoma, and Texas) of the United States. Grassland is susceptible to frequent drought and under different management practices (Bajgain et al. 2016; Basara et al. 2013; Christian et al. 2015; Gu et al. 2007; Gu et al. 2008; Hoerling et al. 2014; Schubert et al. 2004; Worster 1979). The agricultural drought of 2011 in Texas caused more than $7.62 billion in losses, with about half of the loss attributed to the reduction in livestock production (Fannin 2012). Management practices in the pasture are diverse (e.g., burning, grazing, baling, fertilizing), complex (e.g., a mixture of management practices such as grazing and baling, different duration and timing), and can vary over space and time (Campioli et al. 2015; Wilson et al. 2013).

Satellite remote sensing is providing consistent observations of vegetation dynamics, which can be incorporated into drought monitoring over large areas at high spatial and temporal resolutions (AghaKouchak et al. 2015; Wardlow et al. 2012a). The Land Surface Water Index (LSWI) (Xiao et al. 2004), calculated as a normalized ratio between NIR and shortwave infrared (SWIR) bands, is sensitive to the leaf water content and water stress. Recent studies have shown the ability of LSWI to track drought-impacted vegetation or to monitor drought (Bajgain et al. 2016; Bajgain et al. 2015; Chandrasekar et al. 2010; Wagle et al. 2015; Wagle et al. 2014).

Vegetation indices (VIs) derived from satellite images are also used in production efficiency models to estimate gross and net primary production of vegetation. Meanwhile, eddy covariance (EC) measurements can reflect effects of land use and management on the

exchange of carbon dioxide, water vapor, and energy fluxes. Combining the remote sensing and EC techniques help to detect the impacts of diverse management practices on ecosystem dynamics in grassland.

1.2 Overall research objectives

The goal of this dissertation is to facilitate the usage of remote sensing and eddy covariance technologies in characterizing cropland, agricultural drought and land managements and their impacts on ecosystem dynamics. Specifically, my dissertation focuses on three major topics: (1) mapping paddy rice in the Panjin Plain, China; (2) examining the impacts of diverse management practices on plant phenology and carbon fluxes of a pasture; and (3) mapping agricultural drought in grassland in the U.S. Southern Great Plains (SGP) and assessing its impacts on cattle production.

1.3 Organization of the dissertation

This dissertation consists of one introductory chapter, four main chapters, and one summary chapter. Chapters 2, 3 have been published in three peer-reviewed journals, chapter 4 is under the second review, and chapter 5 is in preparation and will be submitted to one peer-reviewed journal.

Chapter 2 aims to develop a new phenology-based paddy rice mapping algorithm to map paddy rice planting area from the rice-wetland coexistent area. This chapter identifies the different flooding/transplanting periods of paddy rice and natural wetlands. The natural wetlands foods earlier and have a shorter duration than paddy rice in the Panjin Plain, a temperate region in China. Using this asynchronous flooding stages, this chapter extracts the paddy rice planting area from the rice-wetland coexistent area. The accuracy, comparison with other products, and uncertainties are discussed.

Chapter 3 examines the impacts of burning, baling, and grazing on canopy and carbon fluxes in a pasture through integrating PhenoCam images, satellite remote sensing, and eddy covariance data. Landsat images were used to assess the baling area and the trajectory of vegetation recovery. MODIS vegetation indices (VIs) were used in the Vegetation Photosynthesis Model (VPM) to estimate gross primary production (GPP_{VPM}) at a MODIS pixel for the flux tower (baled) site. This chapter points out the necessity of combining different techniques to investigate the responses of pastures to different management practices under different climate regimes at multiple temporal and spatial scales.

Chapter 4 focuses on quantifying agricultural drought in tallgrass region in the SGP using a remotely sensed water-related vegetation index (LSWI). The temporal and spatial pattern of drought is presented the compared with precipitation gradient. A comparison with other widely used drought products is made. The relationship between drought and precipitation at the annual and seasonal level are discussed. This chapter highlights the potential of LSWI in agricultural drought monitoring.

Chapter 5 attempts to use meteorological, remote sensing, and statistical data evaluate the impacts of drought and heatwave on cattle production in the SGP during 2000-2015. The random forest and multivariate linear regression are used to model the impacts of social and ecological factors on cattle production.

1.4 List of Publications from the Dissertation

Chapter 2

Zhou, Y., Xiao, X., Qin, Y.W., Dong, J.W., Zhang, G.L., Kou, W.L., Jin, C, Wang, J., Li, X.P, 2016, Mapping paddy rice planting area in rice-wetland mixed areas through

analysis of Landsat 8 OLI and MODIS images, International Journal of Applied Earth Observation and Geoinformation, 46:1-12.

Chapter 3

Zhou, Y., Xiao, X., Wagle, P., Bajgain, R., Mahan, H., Basara, B.J., Dong, J., Qin, Y., Zhang, G., Luo, Y., Gowda, P.H., Neel, P.S.J., Steiner, L.J, 2017, Examining the short-term impacts of diverse management practices on plant phenology and carbon fluxes of Old World bluestems pasture, Agricultural and Forest Meteorology, 237-238:60-70.

Chapter 4

Zhou, Y., Xiao, X., Zhang, G., Wagle, P., Bajgain, R., Dong, J., Jin, C., Basara, B.J., Anderson, C. M., Hain, R.C., Otkin, A. J., 2016, Quantifying agricultural drought in tallgrass prairie region in the U.S. Southern Great Plains 1 through analysis of a water-related vegetation index from MODIS images, Agricultural and Forest Meteorology (under 2nd review).

Chapter 5

Zhou, Y., Xiao, X., Zhang, Y., Zou, Z., Osei, E., Bajgain, R., Basara, B.J., Steiner, L.J., Consecutive years of agricultural drought drove the large losses of cattle production in the U.S. Southern Great Plains (in preparation)

Chapter 2: Mapping paddy rice planting area in rice-wetland coexistent areas through analysis of Landsat 8 OLI and MODIS images

Abstract

Accurate and up-to-date information on the spatial distribution of paddy rice fields is necessary for the studies of trace gas emissions, water source management, and food security. The phenology-based paddy rice mapping algorithm, which identifies the unique flooding stage of paddy rice, has been widely used. However, identification and mapping of paddy rice in rice-wetland coexistent areas is still a challenging task. In this study, we found that the flooding/transplanting periods of paddy rice and natural wetlands were different. The natural wetlands flood earlier and have a shorter duration than paddy rice in the Panjin Plain, a temperate region in China. We used this asynchronous flooding stage to extract the paddy rice planting area from the rice-wetland coexistent area. MODIS Land Surface Temperature (LST) data was used to derive the temperature-defined plant growing season. Landsat 8 OLI imagery was used to detect the flooding signal and then paddy rice was extracted using the difference in flooding stages between paddy rice and natural wetlands. The resultant paddy rice map was evaluated with in-situ ground-truth data and Google Earth images. The estimated overall accuracy and Kappa coefficient were 95% and 0.90, respectively. The spatial pattern of OLI-derived paddy rice map agrees well with the paddy rice layer from the National Land Cover Dataset from 2010 (NLCD-2010). The differences between $Rice_{Landsat}$ and $Rice_{NLCD}$ are in the range of ±20% for most 1-km grid cell. The results of this study demonstrate the potential of the phenology-based paddy rice mapping

algorithm, via integrating MODIS and Landsat 8 OLI images, to map paddy rice fields in complex landscapes of paddy rice and natural wetland in the temperate region.

2.1 Introduction

Paddy rice provides the most important staple food for more than half the global population (FAO 2013) even though it only accounts for around 11% of the world's cropland area (Matthews et al. 2001). With the rapid growth in world population, the demand for food, especially rice, is increasing, which increases pressure on land, water, and biodiversity (Beddington et al. 2012; Godfray et al. 2010). Paddy rice fields consume a large amount of water (Bouman and Tuong 2001; Döll 2002) and emit methane (CH_4) into the atmosphere, which plays an important role in atmospheric chemistry and climate change (Zhuang et al. 2009). The largest sources of CH_4 emissions are rice paddies (~ 33-40 Tg yr^{-1}) (IPCC 2013) and natural wetlands (~177-284 Tg yr^{-1}) (Stocker et al. 2013). Information on the spatial distribution and temporal dynamics of paddy rice fields is important for the studies of trace gas emissions, management of water resources, and food security (Döll 2002; Xiao et al. 2006; Xiao et al. 2005). An updated and accurate paddy rice map with fine spatial resolution (e.g. 30 m) is vital for policy makers and farmers to understand and balance environmental problems (greenhouse gas emissions and water deficit issues) with rice production.

We developed a phenology-based algorithm to identify paddy rice fields based on the unique phenological feature that rice plants are first grown on flooded soils (Xiao et al. 2002a; Xiao et al. 2006; Xiao et al. 2005; Zhang et al. 2015). At the beginning of the growing season, the land surface is a mixture of plants and water and can be detected as flooding using spectral bands or vegetation indices that are sensitive to both

water thickness (Land Surface Water Index, LSWI) and vegetation canopy (Normalized Difference Vegetation Index, NDVI; Enhanced Vegetation Index, EVI). Those areas where LSWI were greater than NDVI or EVI (LSWI ≥ NDVI or LSWI ≥ EVI) during the growing season were identified as paddy rice fields. This algorithm has been applied to map paddy rice fields in Eastern Jiangsu Province, China using VEGETATION data (Xiao et al. 2002a) and in Southern China, Northeast China, and Southeast Asia using MODIS data (Xiao et al. 2006; Xiao et al. 2005; Zhang et al. 2015).

However, accurate mapping of paddy rice in rice-wetland coexistent areas is still challenging since both paddy rice and natural wetlands have a flooding stage in their growing season, which often leads to misclassification of natural wetlands as paddy rice (Brisco et al. 2012; Gong et al. 2010; Xiao et al. 2005). Previous studies has used the thematic map of wetland to deal with this problem and suggested the need to develop a MODIS- or Landsat-based natural wetland mask (Jin et al. 2015; Zhang et al. 2015). A more detailed analysis of the dynamics of paddy rice and natural wetland might give us more clues to solve this problem. Furthermore, the previous phenology-based algorithm has not been applied in the temperate region using Landsat 8 data that has a finer spatial resolution than MODIS although it has been tested in other paddy rice planting areas in China (Qin et al. 2015; Wang et al. 2015). The objective of this study was to develop and test an improved method to map paddy rice in the rice-wetland coexistent areas, using MODIS and Landsat 8 OLI images. As a case study, we selected the Panjin Plain in Liaoning Province, Northeastern China, as (1) extensive natural wetlands and paddy rice are distributed throughout the area and (2) field survey data, agricultural statistical data, and other fine-resolution cropland data are available for the evaluation of a

Landsat 8 OLI-derived paddy rice map.

Using multi-temporal MODIS and Landsat 8 OLI images in 2013, we examined spectral characteristics of various land cover types and applied a phenology-based algorithm to map seasonally flooded/inundated areas. Then, paddy rice fields were distinguished from natural wetland based on the observation of the different timing in flooding stages. Our algorithm focused on the flooding feature of paddy rice and utilized the asynchrony of the flooding signal in paddy rice and reed wetland. It has the potential be applied to large area using program without substantial human inputs. Other conventional classification methods (e.g. Maximum Likelihood, ISODATA, SVM, etc.) either need the prior knowledge of the land cover samples or post classification interpretation which are time consuming and labor intensive. The algorithm has the potential to generate better paddy rice results than others without considering the asynchrony of the flooding signal in paddy rice and reed wetland. The algorithm developed in this study takes advantage of the high temporal resolution (8-day) of MODIS images at 500 m spatial resolution and the high spatial resolution (30 m) of Landsat 8 OLI images at 16-day temporal resolution and may be applied to other rice-producing areas to generate a paddy rice database at 30 m spatial resolution. Such a data product would be critical for studying estimation of trace gas emissions, water sources management, wild bird migration, and food security.

2.2 Materials and methods

2.2.1 Study area

The Panjin Plain is located in the core area of the Liaohe Delta in Liaoning province, Northeast China (40.623-41.597°N, 121.376-122.813°E). Four counties are

included in the study area: Panshan County, Dawa County, Panjin urban area, and Taian County. The first three counties are part of Panjin City with Panjin urban area as the business and administration center and it has a smaller area than the other two. Two main streams of the Liaohe River, one of the largest rivers in Northeastern China, run through the area (Figure 2.1a).

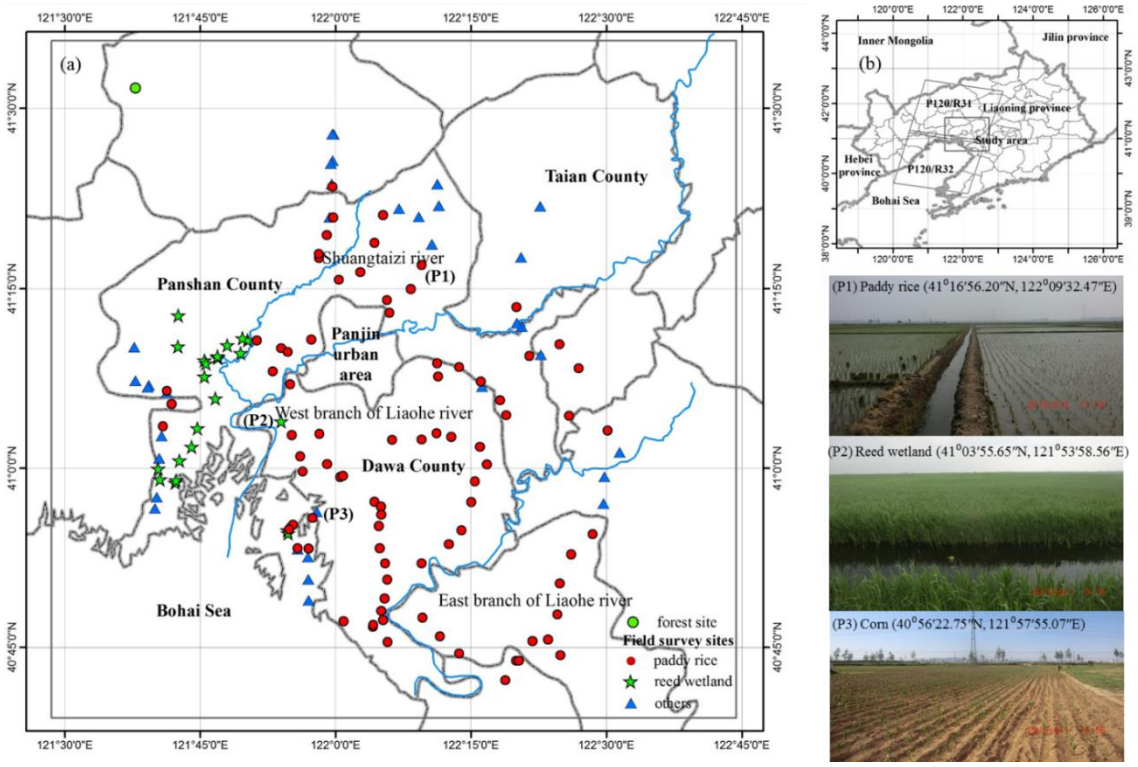


Figure 2.1. (a) Location of the field survey sites in the Panjin Plain, Liaoning Province, China. The total number of sites for paddy rice, reed wetland, and others (corn, soybean, water body etc.) were 86, 21, and 34. (b) Landsat tiles (path/row) for the study area and its location in Liaoning province. (P1), (P2), and (P3) are the photos that show the paddy rice, reed wetland and corn fields.

The Panjin Plain belongs to the temperate zone and has a monsoon climate (Xu et al. 2009). Annual mean temperature is ~10.6 ºC. Annual precipitation is 444 mm, and most of the precipitation occurs between May and September. Forest and natural wetland are the major natural vegetation types. Paddy rice is the most important cropland in this area. Paddy rice, corn, and soybean accounted for 84%, 12%, and 4% of

the total crop area in Panjin City in 2012, respectively (Bureau 2014; Liaoning Statistical Bureau 2013).

2.2.2 Data

2.2.2.1 Landsat 8 (OLI) data and processing

Landsat 8 provides a good source for paddy rice mapping with new features that build upon its predecessors. It gets rid of the gaps problems in Landsat 7 ETM+ and has the same spatial resolution (30 m) which makes it possible to generate finer resolution paddy rice map than MODIS (Salmon et al. 2015; Zhang et al. 2015). The additional quality assessment band includes information on cloud and cirrus; ETM+ and its predecessors do not have such quality information for each pixel which might bring error in previous studies (Beddington et al. 2012; Liu et al. 2005).

Table 2.1. Landsat 8 images used in this study. Two tiles (Path120/Row31 and Path120/Row32) are combined to cover the study area. The cloud cover information of each image is given by the metadata.

DOY	Date	Cloud cover (P120/R31)	Cloud cover (P120/R32)
2013111	4/21/2013	2.86%	17.06%
2013127	5/7/2013	Only thermal bands	Only thermal bands
2013143	5/23/2013	0.14%	4.19%
2013159	6/8/2013	0.24%	22.18%
2013175	6/24/2013	75.77%	89.56%
2013191	7/10/2013	No image available	No image available
2013207	7/26/2013	3.44%	2.68%
2013223	8/11/2013	65.18%	22.06%
2013239	8/27/2013	91.32%	58.90%
2013255	9/12/2013	3.00%	23.16%
2013271	9/28/2013	48.17%	30.25%
2013287	10/14/2013	No image available	No image available
2013303	10/30/2013	1.00%	0.98%
2013319	11/15/2013	0.89%	1.36%
2013335	12/1/2013	5.59%	4.72%
2013351	12/17/2013	45.93%	47.69%

We downloaded Landsat 8 data products from April to December 2013 in the Panjin Plain from the USGS EarthExplorer (http://earthexplorer.usgs.gov/). Two tiles are needed to cover the study area (Figure 2.1b). A total of 26 images were used for this study (Table 2.1).

Each Landsat 8 OLI image was atmospherically corrected to generate surface reflectance, using the Fast Line-of-Sight Atmospheric Analysis of Spectral Hypercubes (FLASSH) (Adler-Golden et al. 1999; Matthew et al. 2000), a matured and easy to use atmospheric correction method imbedded in popular remote sensing software (e.g. ENVI). The OLI data product includes a 16-bit quality assessment (QA) file in GeoTIFF format, which contains information on clouds and cirrus. We used the Landsat-LDOPE Toolbelt to extract cloud and cirrus covered pixels from the QA file. The medium (34%-66%) confidence level was used for both cloud and cirrus information detection in the QA file. Other criteria were further applied to detect cloud: when a pixel has a blue band reflectance value ≥ 0.2 and a positive LSWI value, it was masked as a cloudy pixel. In order to exclude the effect of cloud and cirrus, we combined these three criteria to generate a cloud mask for each image; all cloud pixels were excluded from further analysis (Xiao et al. 2006).

For each image, we calculated NDVI, EVI, and LSWI using surface reflectance from blue (ρ_{blue}), red (ρ_{red}), NIR (ρ_{nir}), and SWIR (ρ_{swir} , 1.63-1.65 μm) bands:

$$NDVI = \frac{\rho_{\text{nir}} - \rho_{red}}{\rho_{\text{nir}} + \rho_{red}} \quad (1)$$

$$EVI = G \times \frac{\rho_{\text{nir}} - \rho_{red}}{\rho_{\text{nir}} + C_1 \times \rho_{red} - C_2 \times \rho_{blue} + L} \quad (2)$$

$$LSWI = \frac{\rho_{\text{nir}} - \rho_{swir}}{\rho_{\text{nir}} + \rho_{swir}} \quad (3)$$

NDVI is related to changes of leaf area index and the amount of green biomass within the canopy (Xiao et al. 2002b), but it has some limitations including saturation under dense canopy and vulnerability to atmospheric conditions and visible soil background (Huete et al. 2002). EVI uses the blue band in combination with the red band to reduce atmospheric contamination and also has a soil background adjustment factor L. The coefficients C1, C2, and L are 6.0, 7.5, and 1.0, respectively, and G is a gain factor set to 2.5 (Huete et al. 2002). LSWI is sensitive to equivalent water thickness (Xiao et al. 2002a).

2.2.2.2 MODIS data and processing

MODIS Land Surface Temperature (LST) products provide the estimation for daytime and nighttime land surface temperature at 1-km spatial resolution (Wan et al. 2002). The 8-day LST products (MOD11A2) were used to investigate temperature dynamics at the regional level.

MODIS land surface reflectance data (MOD09A1) was used to investigate the dynamics of different land cover types. NDVI, EVI, and LSWI were calculated using the same equations mentioned in the above section. Normalized Difference Snow Index (NDSI) was also calculated from the MOD09A1 data using green and SWIR bands, which is used in snow/ice identification latter (Hall et al. 2002) to minimize the potential impact of those observations with snow/ice cover in the spring and winter.

$$NDSI = \frac{\rho_{green} - \rho_{swir}}{\rho_{green} + \rho_{swir}} \quad (4)$$

2.2.2.3 Crop calendar

Paddy rice seeds are sown in a small, richly nourished seed bed in mid-April, and it takes about one month for the seeds to grow up and be ready to be transplanted into flooded fields. Flooding is an important feature of paddy rice that differentiates it from other plants, including soybean, corn, and deciduous forest (Table 2.2). Usually, farmers irrigate the paddy rice fields at the end of April and then transplant rice plants in late May. In June and July, the rice seedlings grow quickly and cover the whole area of the field. The rice plant is mature by the end of September and harvested in October.

Table 2.2. Phenology stages of major plants in the Panjin Plain, Liaoning Province, China. The phenology data of paddy rice, soybean, and corn were provided by China Meteorological Data Sharing Service System (http://cdc.cma.gov.cn/home.do). The phenology stages of reed wetland and deciduous forest were extracted from (Li et al. 2006) and (Yu and Zhuang 2006), respectively.

Month	April			May			June			July			August			September			October		
Ten-day	E	M	L	E	M	L	E	M	L	E	M	L	E	M	L	E	M	L	E	M	L
Paddy rice		1	2			3	4	5				6	7			8		9	10		
Soybean				1	2	3		4			5	6						7			
Corn				1	2	3	4			5		6		7				8			
Reed wetland			1		2											3				4	
Deciduous			1		2					3								4			

Paddy rice: 1-Sowing, 2-Seeding/Flooding, 3-Transplanting/Flooding, 4-Reviving, 5-Tillering, 6-Booting, 7-Heading, 8-Milky maturity, 9-Mature, 10-harvesting**;**

Soybean: 1-Sowing, 2-Seeding, 3-The third true leaf, 4- Branches forming, 5-Flowering, 6-Pod setting 7-Mature;

Corn: 1-Sowing, 2-Seeding, 3-Three leaves, 4-Seven leaves, 5-Stem elongation, 6-Heading, 7-Milk maturity, 8-Mature;

Reed wetland: 1-Germinating, 2-Leafing, 3-Flowering, 4-Fade;

Deciduous Forest: 1-Sprouting, 2-Leafing, 3-Growing, 4-Defoliating.

Plants in natural (reed) wetland begin to germinate in late April or early May when temperatures rise up to 0 ºC. When reed wetland is in the leafing stage with a closed canopy in middle or late May, paddy rice fields are still in the flooding stage. The asynchrony of the paddy rice's and reed wetland' growing season phases makes it possible to distinguish them using multi-temporal satellite images.

2.2.2.4 Field survey data

We carried out a field survey in the study area during the period of May 31st to June 3rd, 2013, when most paddy rice fields were in the flooding/transplanting phase and reed wetland had a closed canopy. The sampling distance between two different sites was 3-5 km. The width and length of the field sites were larger than 100 m and of the same land cover type. The land cover types at the sites were classified as one of three: paddy rice, reed wetland or others. We considered corn, soybean, water body, or built-up to be "others" without listing all the specific land cover types because they were minor land cover types and also out of the major scope of this study. For the paddy rice sites, we went into the paddy rice field at least 60 m away from the border in each direction and took the geo-referenced photo. For the reed wetland sites, we stood on the road running through the large reed wetland area, instead of going into the center of the reed wetland by boat, limited by time and human resources. The total numbers of sites for paddy rice, reed wetland and other land cover types were 86, 21, and 34, respectively (Figure 2.1a). All field survey sites were used in the validation process.

2.2.2.5 Other land cover datasets for inter-comparison

The National Land Cover Dataset from 2010 (NLCD-2010) at a 1:100,000 scale

was generated by the Chinese Academy of Sciences through visual interpretation and digitalization of Landsat images (Liu et al. 2014; Zhang et al. 2014b). Its classification scheme has six classes and 25 subclasses of land use types and includes paddy rice as one of the subclasses in the dataset. The human-computer interactive interpretation method was used to interpret the Landsat TM/ETM+ images and HJ-1 satellite images and generate vector patches of different land cover types (1:100,000 scale). Extensive field survey data were used to evaluate the accuracy of the NLCD-2010 dataset. The resultant NLCD were aggregated and rasterized to have a spatial resolution of 1-km with cell values assigned as the percentage of different land use and land cover types. In this study, the 1-km resolution paddy rice thematic map of the NLCD-2010 dataset was used for comparison with the Landsat 8 OLI-derived paddy rice map.

The Liaoning Statistical Yearbook from 2014 is a yearly summary public government report. The data is reported by the lower district level (city) to the provincial office. It contains the economic, societal, and environmental conditions of the year before the publication of the statistical yearbook (e.g. Liaoning Statistical Yearbook from 2013 reflects the conditions of 2012). Considering the uncertainty of the statistical data, the comparison between the Landsat 8 OLI-derived paddy rice map and statistical data is coarse.

2.2.3 Temperature-defined plant growing season

In the Panjin Plain, the daily minimum air temperature rises above 0 ºC in April (Figure 2.2). It remains above 10 ºC from the end of April to September. The daily minimum temperature drops below 0 ºC at the end of October or the beginning of November. The temperature-defined plant growing season (0 ºC threshold) runs from April to October based on the weather station data. The LST_{night} data from MODIS corresponds well with the daily minimum air temperature for the same pixel where the weather station located.

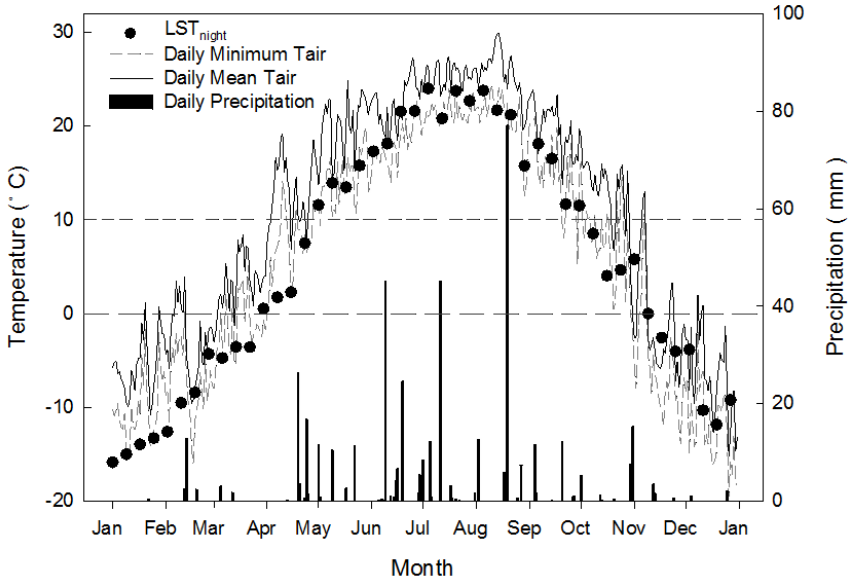


Figure 2.2. Daily mean and minimum temperature, precipitation and night time land surface temperature (LST_{night}) in the Panjin Plain. Temperature and precipitation data is from the weather station located at Jin Zhou City (41.08 ºN, 121.07 ºE) and collect collected from China Meteorological Data Sharing Service System (http://www.escience.gov.cn/metdata/page/index.html). LST_{night} data is from MOD11A2 product for the pixel where the weather station is located in. The two dash lines denote the 0 ºC and 10 ºC. The weather station is not in the study area but is the closest one with data available.

LST_{night} from MODIS rises above 0 ºC usually around April 15 (Figure 2.3a) in the Panjin Plain. Then, natural plants such as reeds and trees begin to grow. The regional LST_{night} map shows that the temperature rises up to 10 ºC around May 9 (Figure 2.3b), and paddy rice fields are in the flooding stage. LST_{night} remains above 10

ºC from early May to early September (Figure 2.3d) and drops to less than 10 ºC at the beginning of September when paddy rice is mature and reeds enter the senescence phase. Paddy rice is harvested in October before the daily minimum temperature approaches 0 ºC (Figure 2.3c). The growing stages recorded by crop calendar (Table 2.2) matched well with the temperature-defined plant growing season from both local climate data and the LST_{night} data.

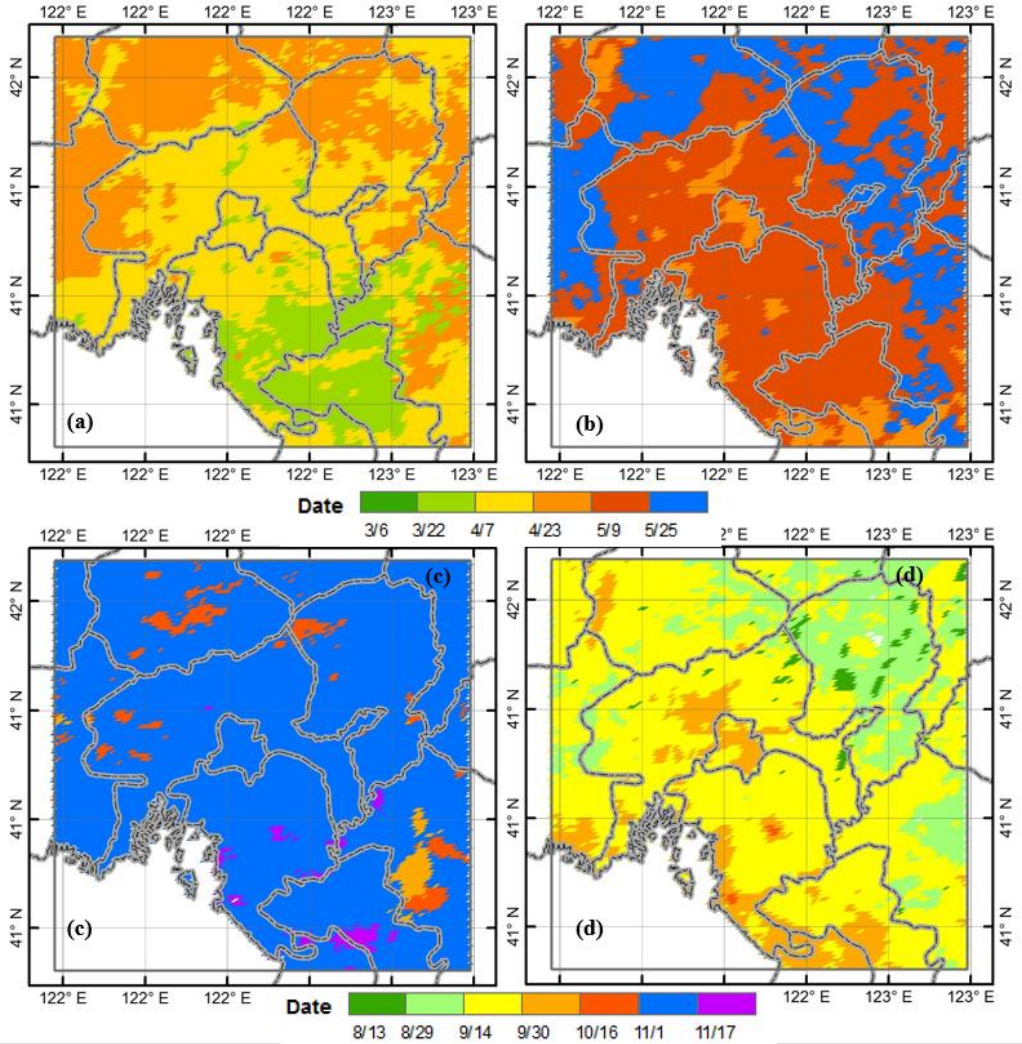


Figure 2.3. Spatial distribution of temperature-defined plant growing season as delineated by LST_{night} in the Panjin Plain derived from MOD11A2 in 2013. (a) The first date with LST_{night}>=0 ºC; (b) the first date with LST_{night}>=10 ºC; (c) the end date with LST_{night}>=0 ºC; (d) the end date with LST_{night}>=10 ºC.

2.2.4 Phenology-based algorithm to identify paddy rice

2.2.4.1 Seasonal dynamics of vegetation indices of major land cover types from MODIS

Figure 2.4 shows the seasonal dynamic of NDVI, EVI, and LSWI from MOD09A1 data for four typical land cover sites: paddy rice, reed wetland, corn, and forest. Vegetation indices of natural vegetation (Figure 2.4b and Figure 2.4d) increase quickly from early May. NDVI is > 0.30 and EVI is > 0.20 in reed wetland (Figure 2.4b) in late May, indicating green-up of plants. At the same time NDVI and EVI in paddy rice (Figure 2.4a) are less than 0.3 and 0.2 respectively, which suggests that transplanting has not yet started or has finished but the canopy is still open. NDVI and EVI in crops (Figure 2.4a and Figure 2.4c) increase quickly starting in late June. The LSWI values are always lower than NDVI and EVI from April to October in corn and forest while LSWI values are greater than NDVI or EVI in May and/or June in paddy rice and reed wetland, and this signal (LSWI $\geq$ NDVI or LSWI $\geq$ EVI) occurs in several continuous 8-day periods.

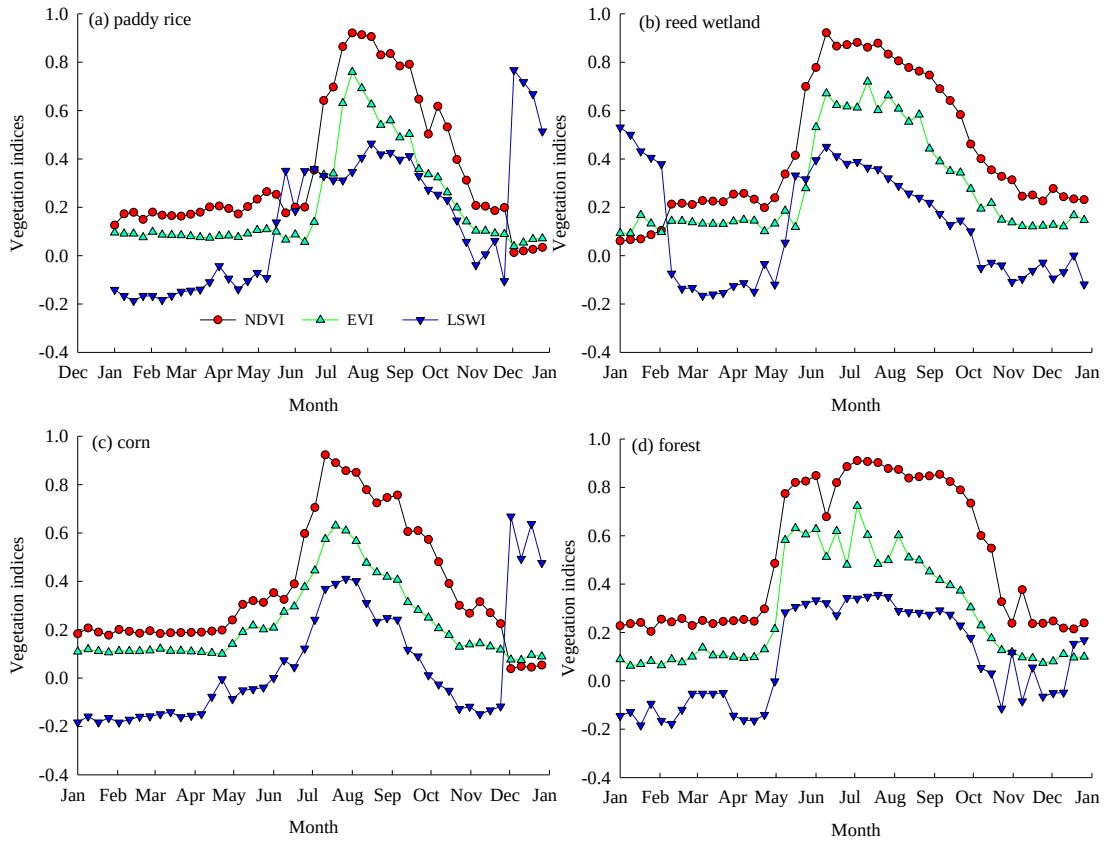


Figure 2.4 The seasonal dynamics of NDVI, EVI, and LSWI of major land cover types from MOD09A1 product in 2013 (a) a paddy rice site (41.0437 ºN, 122.2137 ºE), (b) a reed wetland site (41.2127 ºN, 121.7095.ºE), (c) a corn site (41.1159 ºN, 121.6550 ºE), and (d) a forest site (41.5279 ºN, 121.6303 ºE). All sites were selected according to the field sampling sites and were representatives of major land cover types except forest site was selected based on Google Earth image.

2.2.4.2 Identification of flooding/inundation signal

For the major land cover types in the study area, only paddy rice and weeds present flooding/inundation events. Some previous works suggest that LSWI $\geqslant$ NDVI or LSWI $\geqslant$ EVI coincide with flooding events (Xiao et al. 2002a; Xiao et al. 2006; Xiao et al. 2005).This phenomena is also present in Figure 2.4 (a) and (b). Those pixels identified as flooded during the whole year may be pure water or mixtures of water and plants where water information is dominant in the pixel. The seasonally flooded pixels identified in some periods of the year include seasonal water bodies, reed wetland, and

paddy rice. Seasonal water bodies form during the flood season when precipitation provides a water source. This feature helps us to detect seasonal water bodies via identifying flooded pixels during plant canopies' closed period, when reed wetland and paddy rice are not flooded. After excluding permanent and seasonal water bodies from the flooding/inundated pixels, the remaining pixels are reed wetland and paddy rice.

2.2.4.3 The asynchronous flooding/inundation stages of paddy rice and reed wetland from MODIS and Landsat 8 OLI

The flooding signal of paddy rice can be detected in DOY 143 (5/23/2013) and DOY 159 (6/8/2013), but reed wetland was only flooded in DOY 143 (Figure 2.5). The asynchronous flooding/inundation stages of paddy rice and reed wetland can be detected from both MODIS and Landsat 8 OLI data and is consistent in the points used for validation. Reed wetland is a form of natural vegetation and grows when the temperature is suitable. According to the LST_{night} data in the Panjin Plain, the temperature-defined growing season begins around April 15 (DOY 105). In DOY 159, the reed wetland canopy is closed while the paddy rice canopy is still open with a mixture of rice plants and water because the temperature-defined plant growing season for reed wetland starts about one month before paddy rice. We assumed those pixels flooded in DOY 143 but not flooded in DOY 159 were reed wetlands since the flooding signal of reed wetland lasts to the end of May and disappears before the beginning of June. Flooding pixels in DOY 159 were identified as paddy rice fields (Figure 2.5).

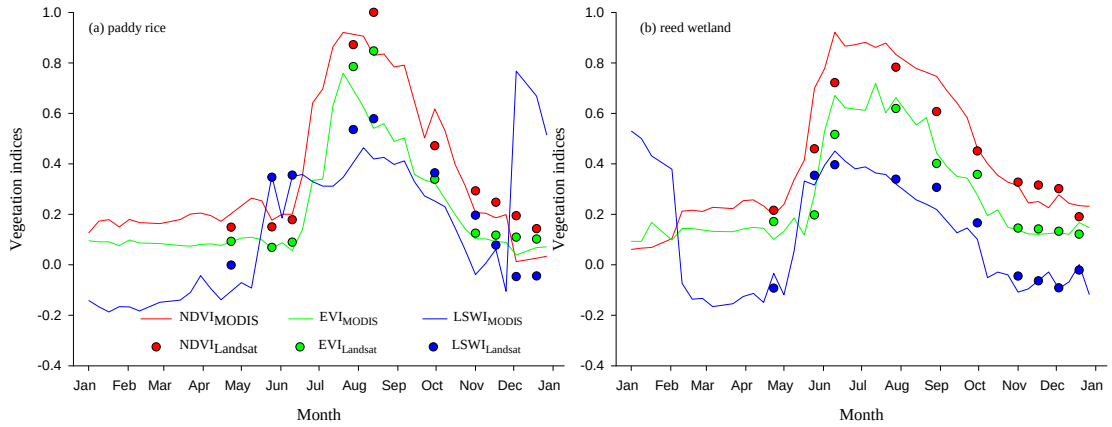


Figure 2.5. The seasonal dynamics of NDVI, EVI, and LSWI from both MODIS and Landsat 8 OLI images at a paddy rice site and a reed wetland site, which were also used in Figure 4. MODIS vegetation indices were gap-filled values while Landsat 8 OLI vegetation indices only included good observations used in this study. Black rectangles indicated the flooding periods from Landsat vegetation indices.

2.2.4.4 Implementation of phenology-based paddy rice mapping algorithm

To implement the Landsat 8 OLI paddy rice detection algorithm at the image level, we developed a procedure (Figure 2.6) by generating various masks for cloud (using the QA file, reflectance in the blue band, and LSWI as mentioned before (Section 2.2.2.1)), snow/ice cover, built-up and barren soil, evergreen vegetation, and permanent water bodies (Qin et al. 2015) in an effort to minimize their potential impacts.

Cloud, snow/ice, built-up and barren soil, evergreen vegetation, and permanent water bodies were excluded from identification of the flooding period. Permanent water bodies were identified based on the frequency of flooding. We assumed a pixel to be permanent water body if it was identified as water with a frequency ≥ 0.80. After applying these masks, the remainder were seasonally flooded pixels that included reed wetland and paddy rice. Paddy rice and reed wetland were then mapped according to their asynchronous flooding/inundation stages.

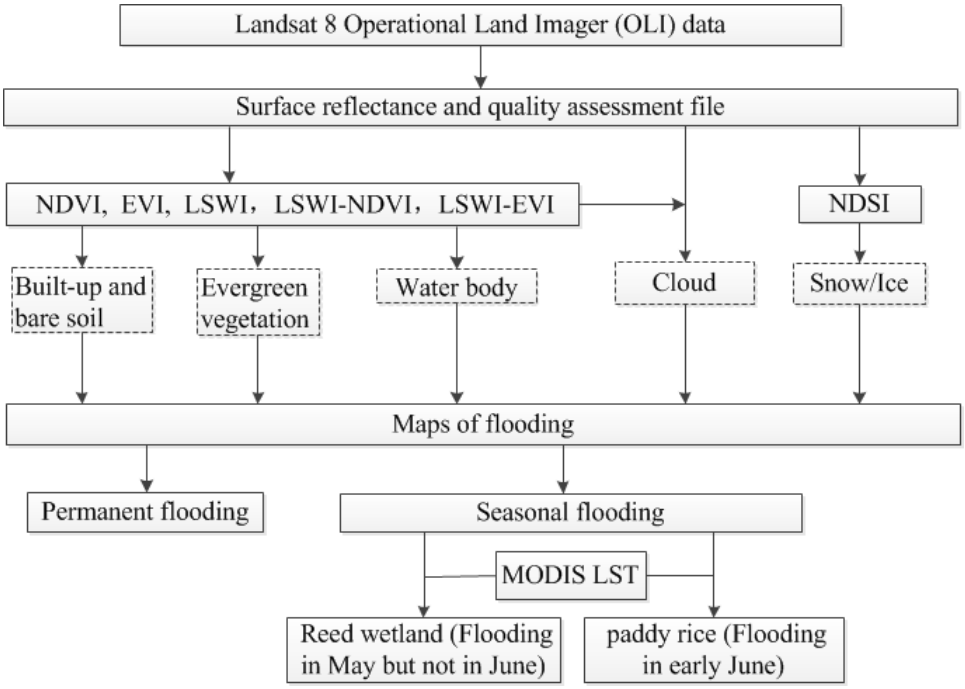


Figure 2.6. A schematic diagram illustrating the implementation of the algorithm for mapping of paddy rice in the Panjin Plain from multi-temporal Landsat 8 OLI data and MODIS data.

2.2.5 Accuracy assessment

Our previous study has shown that integrating the field photo library and Google Earth is reliable for generating Regions of Interest (ROIs) for land cover classification (Dong et al. 2012a; Dong et al. 2012b). We combined the geo-referenced field photos collected in the field survey and high-resolution images from Google Earth to generate ROIs, following the procedure reported in a previous study (Dong et al. 2014). The image provider in the study area is Digital Globe. The images we used are mostly from April to July 2013. If there is no high resolution images during this period, we went back or forth for one year. Since our goal is to map paddy rice and the small number of other land cover type sites, we divided all the filed survey sites into two categories: paddy rice and others (including reed wetland, corn, soybean, water body etc.) to

generate ROIs. A total of 141 ROIs (11, 044 pixels) were generated for product validation. Using the Landsat 8 OLI-derived paddy rice map and ROI data, we calculated the confusion matrices for paddy rice and other land cover types in an effort to obtain ROI-based validation.

2.2.6 Comparison with other paddy rice datasets

The paddy rice area was summarized by county (city) from the Landsat 8 OLI-derived paddy rice map and NLCD-2010 dataset (hereafter referred to as $Rice_{Landsat}$ and $Rice_{NLCD}$). The comparison between $Rice_{Landsat}$ and $Rice_{NLCD}$ was conducted at the county level. The comparison between $Rice_{Landsat}$ and the statistical data was conducted for Panjin City as city is the smallest unit of the statistical data.

The $Rice_{Landsat}$ map is a binary (0 or 1) map with a spatial resolution of 30 m×30 m and an area of 900 m^2 for each pixel. We counted the number of pixels with the value of 1 (indicating the existence of paddy rice) in the $Rice_{Landsat}$ map and then calculated the total area of rice by multiplying the total number of rice pixels with the area of a Landsat image pixel (900 m^2) within the area of a 1-km grid cell. Note that the grid cell in the $Rice_{NLCD}$ product has a spatial resolution of 1km ×1km and an area of 1 km^2, so the paddy rice area of an individual grid cell was calculated using the equation: percentage fraction×0.01 km^2. The sum of paddy rice area in each 1-km grid cell is the total area of paddy rice in the $Rice_{NLCD}$ product.

2.3 Results

2.3.1 Spectral signature of major land cover types during and after paddy rice flooding stage

Figure 2.7 b1 shows the distribution of NDVI and the difference between LSWI

and NDVI (LSWI-NDVI) from Landsat 8 OLI data in DOY 159, when paddy rice was still in its flooding stage but reed wetland was in its leaf stage. The LSWI-NDVI values for paddy rice and water are larger than 0, which means they are flooded. Other land cover types including reed wetland, forest, and shrub, don't show this flooding feature. The distribution of EVI and LSWI-EVI (Figure 2.7 c1) shows a similar pattern with NDVI and LSWI-NDVI (Figure 2.7 b1). The distribution of LSWI and LSWI-NDVI or LSWI-EVI have similar patterns with a clear flooding signal for paddy rice (Figure 2.7 d1, e1). However, the distribution of vegetation indices (NDVI, EVI, and LSWI) and the difference in vegetation indices (LSWI-NDVI, LSWI-EVI) in an image within the tillering stage (closed canopy) (DOY 207, 7/26/2013) don't have a similar pattern to DOY 159; paddy rice, reed wetland are mixed together (Figure 2.7 below panels). It is

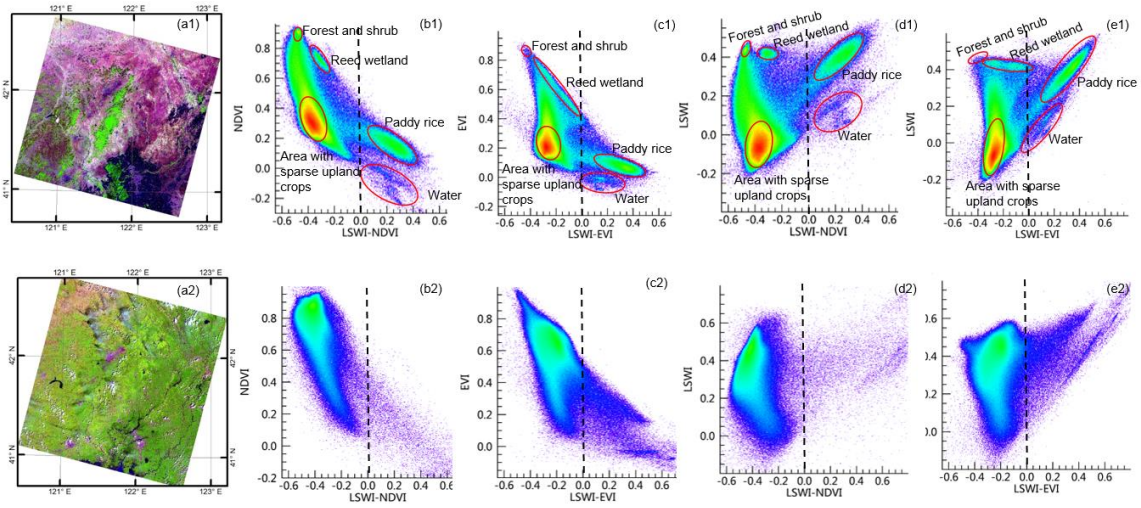


Figure 2.7. The 2-D scatter plots of vegetation indices and the difference between two vegetation indices from the Landsat 8 OLI data during the paddy rice flooding period (upper panels)and the tillering period (below panels). The color density represents the number of pixels. (a) Landsat images are false composite displayed with red (SWIR), green (NIR) and blue (red), (b) NDVI versus LSWI-NDVI, (c) EVI versus LSWI-EVI, (d) LSWI versus LSWI-NDVI, and (e) LSWI versus LSWI-EVI.

difficult to use images in DOY 207 to distinguish paddy rice and reed wetland since

both of them have high NDVI and EVI values and are without flooding signals on that date.

2.3.2 Paddy rice map of the Panjin Plain from Landsat 8 OLI data

Figure 2.8 shows the spatial distribution of paddy rice in the Panjin Plain from Landsat 8 OLI data. Paddy rice fields are mainly distributed in the three counties of Panjin City. No large paddy rice field appears outside of the four counties included in the study area except a relatively large one to the east of Dawa County. Paddy rice areas are mostly located along the two main streams of the Liaohe River. Some paddy rice fields are located around the Shuangtaizi River, which also runs through large reed wetland areas.

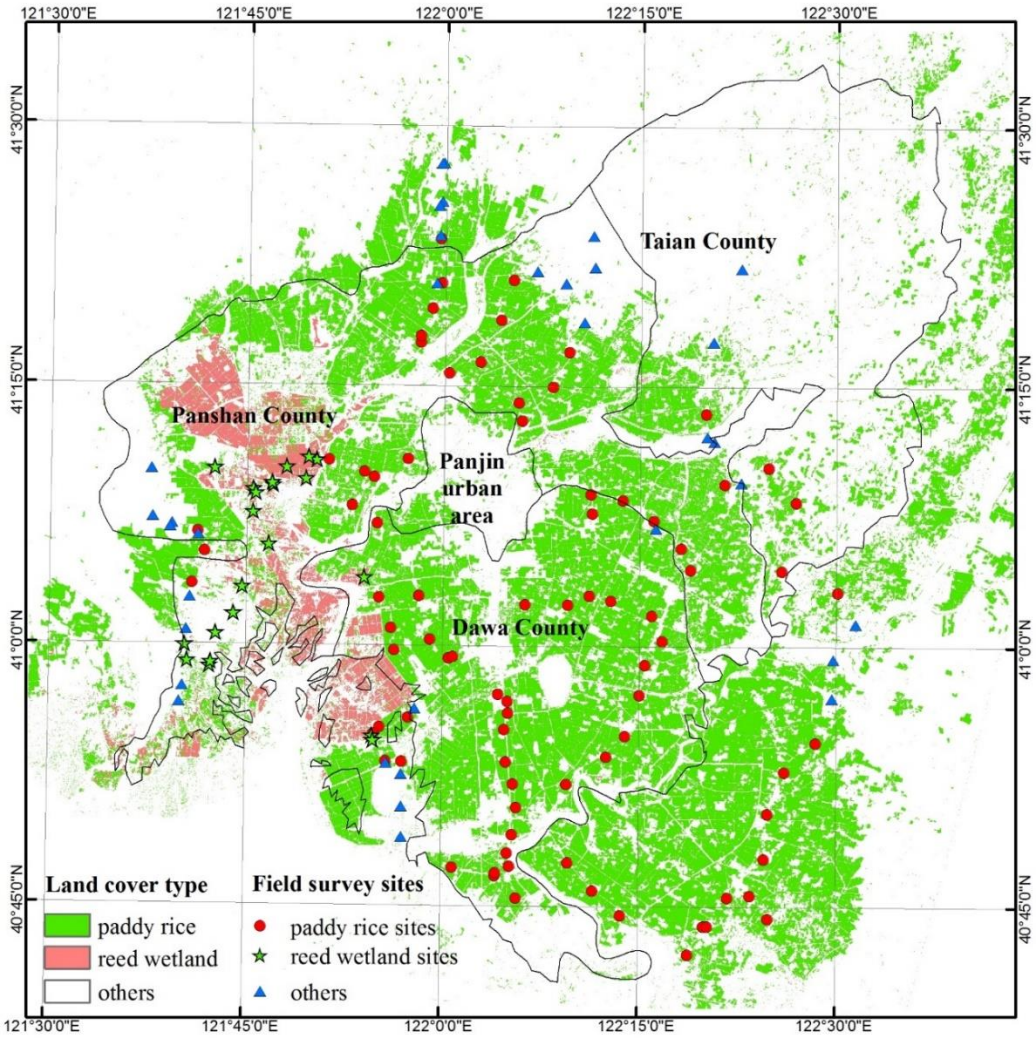


Figure 2.8. The resultant paddy rice map of the Panjin Plain derived from the Landsat 8 OLI data in 2013 at 30-m spatial resolution. Field survey sites were included for reference.

2.3.3 Validation of the paddy rice map derived from Landsat 8 OLI data

The classification map of paddy rice was compared with the ROIs generated based on the ground-truth data and high resolution images in Google Earth. The results indicate a very high agreement between the classification map and ground-based data for paddy rice. The overall accuracy and Kappa coefficient are, respectively, 95% and 0.90 for the ROIs based validation (Table 2.3). The producer's and user's accuracy for

paddy rice are 93% and 91%, respectively. 91 reed wetland pixels and 221 others pixels were classified as paddy rice. Although the map of reed wetland is not good according to the field survey data, it is not mixed with paddy rice (Figure 2.8). The low accuracy of the reed wetland is because some reed wetlands were never flooded during the whole year or the flooding signal was not captured by the Landsat images due to the 16-day revisit period and cloud and cloud shadow effect. The commission error might be because the irrigation or the flooding event in other land cover types during the paddy rice flooding/transplanting period. The omission error might be because the bad observation affected by clouds and cloud shadows and the mixed pixels of rice paddy fields and non-rice paddy fields (roads, irrigation channels, etc.)

Table 2.3. The confusion matrix between the $Rice_{Landsat}$ in the Panjin Plain and ROIs derived from geo-reference field photos in the field survey and high resolution images in Google Earth.

	Class	Ground truth (GT) samples (pixels)		Total classified pixels	User Acc. (%)	Commission errors (%)
		Paddy rice	Others			
Classification	Paddy rice	3322	312	3634	91	9
	Others	263	7147	7410	96	4
	Total GT pixels	3585	7459	11044		
	Pro.Acc. (%)	93	96			
	Omission errors (%)	7	5			

2.4 Discussion

2.4.1 Advantages of the pixel- and phenology-based algorithm

The pixel-and phenology-based algorithm focuses on the specific phenological features of paddy rice and reed wetland in individual pixels and therefore is not dependent on other pixels' spectral features within the same image. The spectral

signature of images after the flooding stage of paddy rice shows no big difference between different land cover types (Figure 2.7 below panels). This indicates that the image-based clustering method might have some bias if images from canopy closed periods are used. The pixel-and phenology-based algorithm works well using MODIS data (Xiao et al. 2006; Xiao et al. 2005; Zhang et al. 2015; Zhang et al. 2009). The extended algorithm for Landsat 8 OLI used in this study, through analyzing the different timing of flooding stages of paddy rice and wetland works well for mapping paddy rice in rice-wetland coexistent areas in the Panjin Plain China and probably in the same latitude with similar climate. The high producer's and user's accuracy indicate the high accuracy of the Landsat 8 OLI-derived paddy rice map at 30 m resolution. However, the phenology of paddy rice and wetland should be studied to identify the difference of flooding stages before utilizing this algorithm in other locations with different climate system.

2.4.2 Comparison of Landsat 8 OLI-derived rice map with other products

The spatial pattern of paddy rice from $Rice_{Landsat}$ (Figure 2.9a) is very similar to that of the NLCD-2010 reference dataset (Figure 2.9b), though the former shows more heterogeneity. There are some notable differences between the $Rice_{Landat}$ and $Rice_{NLCD}$ map. First, in the western part of the study area, $Rice_{Landsat}$ identifies some scattered paddy rice fields while the $Rice_{NLCD}$ product reports almost no rice fields in this region. Farmers converted reed wetlands into the paddy rice files seen in the western part of the $Rice_{Landsat}$ map to increase their income according to the observation of our field survey. Second, paddy rice fields in the Panjin urban area are smaller in the $Rice_{Landsat}$ map than in the $Rice_{NLCD}$ product. The reason is the rapid urbanization of the city area. We can

see that the size of Panjin urban area in the $Rice_{Landsat}$ map was larger than in the $Rice_{NLCD}$ map. According to the statistical yearbook in Liaoning province from 2010 to 2013, the built-up area in Panjin City increased from 58.9 km^2 to 69.6 km^2. The spatial pattern of the differences between Landsat 8 $Rice_{Landsat}$ and $Rice_{NLCD}$ also shows that the paddy rice area in these two products is consistent with each other (Figure 2.9c).

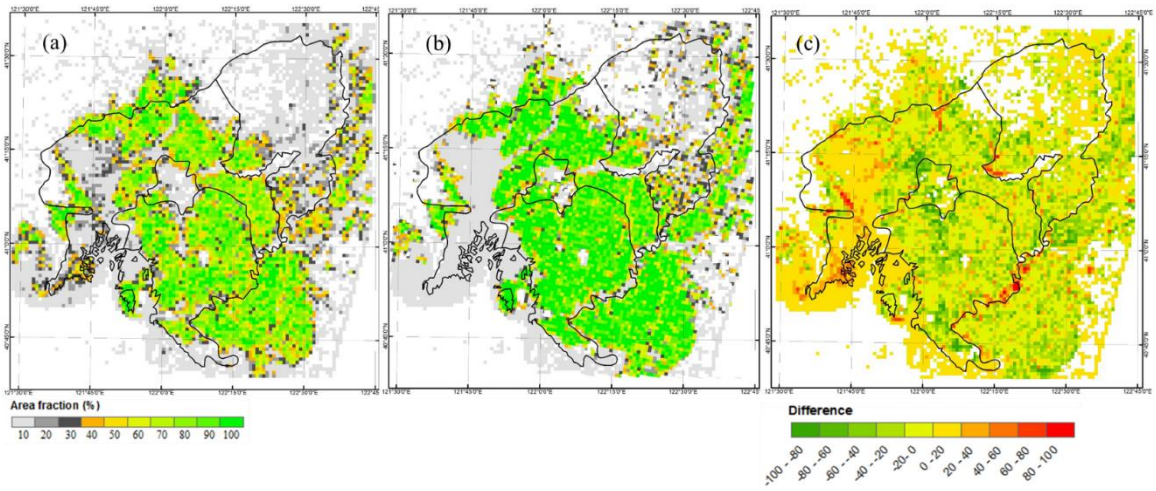


Figure 2.9. Paddy rice maps derived from (a) the $Rice_{Landsat}$ and (b) the $Rice_{NLCD}$ at the 1-km spatial resolution (c) the comparison between the $Rice_{Landsat}$ and the $Rice_{NLCD}$.

The total area of paddy rice fields in the $Rice_{Landsat}$ map and $Rice_{NLCD}$ product is 2,517 km^2 and 3,309 km^2, respectively. We calculated the paddy rice area in the four counties of the study area from the $Rice_{Landsat}$ map and $Rice_{NLCD}$ product (Figure 2.10a). $Rice_{NLCD}$ has more paddy rice area than $Rice_{Landsat}$ in all counties with the largest difference in Dawa County. The frequency distribution of the differences between $Rice_{Landsat}$ and $Rice_{NLCD}$ shows that more than 50% of pixels have the same percentage fraction of paddy rice area in the 1 km × 1 km pixel (Figure 2.10b). 80% of pixels are located in the range of ±20%, which means the percentage fraction of paddy rice in most pixels from $Rice_{Landsat}$ and $Rice_{NLCD}$ agreed with each other. More negative than

positive difference percentage values also indicates that the estimated paddy rice area in $Rice_{NLCD}$ is greater than that of $Rice_{Landsat}$. The visualization and digitalization process may introduce some error since producers might have different criteria.

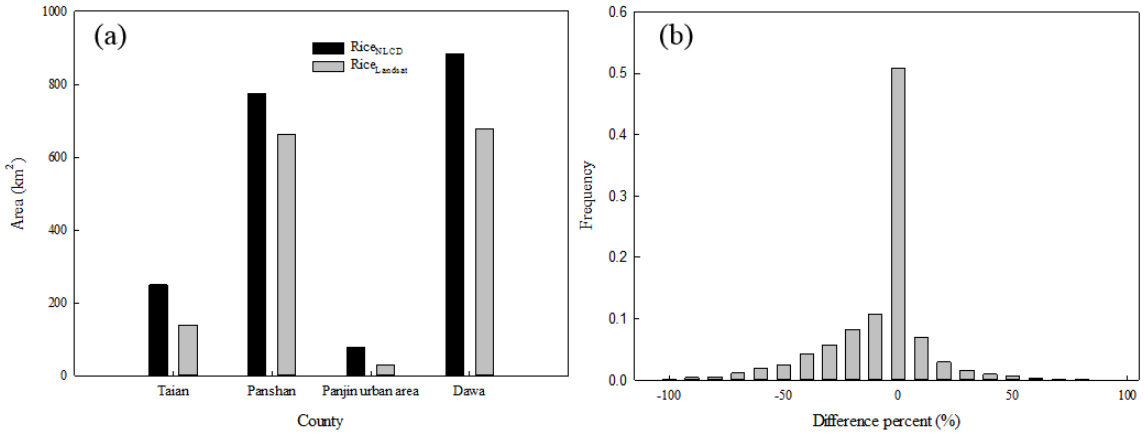


Figure 2.10. The quantitative comparison between paddy rice maps derived from the $Rice_{Landsat}$ and the $Rice_{NLCD}$ at (a) county level and (b) pixel level.

The paddy rice area in Panjin City in the $Rice_{Landsat}$ map was higher than the statistical data (1,373 km^2 versus 1,076 km^2). The uncertainty of statistical data (artificial error or omission) between the $Rice_{Landsat}$ map and the statistical data might contribute to the difference. Since the statistical yearbook in Liaoning province in 2014 was the from the sample survey, it might not be able to represent the whole area condition.

Another study showed that paddy rice area in Panjin City is 1,832 km^2 in 2010 using MODIS data (Zhang et al. 2015). It is higher than both the statistical data and our results. However, the different observation time might explain the difference. Another possible reason might be the natural wetlands used in this study was not very accurate and some of the natural wetlands were misclassified as paddy rice.

We also compared the paddy rice map derived from the pixel- and phenology-

based algorithm with paddy rice maps derived from other two conventional classification methods (the image-based clustering methods), ISODATA and Support Vector Machine (SVM), using the image in DOY 159 (paddy rice flooding period, Figure S2.1). The paddy rice map from the ISODATA showed more fragmented paddy rice area (Figure S2.2) than our results. The overall accuracy and Kappa coefficient are 84%, and 0.64, respectively. Both the producer's and user's accuracy are 76% (Table S2.1). The overall accuracy and Kappa coefficient for SVM method are 94% and 0.87, very close to our results. However, a big area of water body in the northern part is misclassified as paddy rice (Figure S2.3). The producer's accuracy is even higher than ours (96% vs. 93%) (Table S2.2). That's because no sample sites were located in the misclassified area. The pixel- and phenology-based paddy rice map showed higher accuracy than the ISODATA method and doesn't need the training samples, yet the SVM needs extensive field samples to build the prior-knowledge.

2.4.3 Sources of uncertainty and limitation

Malfunctions of the satellite and operation of sensors may reduce the availability of data. In this study, we missed three images for the study area not scanned by the Landsat 8 OLI sensor. The data quality is also constrained by cloud and cloud shadow. If there is no available image during the flooding period of paddy rice because of the acquisition schedule or cloud, it is hard to map paddy rice using any algorithm based on optical remote sensing. The irrigation or flooding event in other land cover types during the paddy rice flooding/transplanting period might affect the classification results. The mixed pixels of rice paddy fields and non-rice paddy fields (roads, irrigation channel, etc.) might be missed if the flooding signal is not captured. The combination of the

Landsat 7 (ETM+) and Landsat 8 (OLI) imagery could potentially provide data at eight-day intervals which may increase the data availability for phenology-based paddy rice mapping (Qin et al. 2015). However, the stripe present in Landsat 7 images could spoil the results even part of it is correctable. MODIS LST products were used to choose the images during the flooding period for identifying paddy rice areas. However, there is no LST product from the Landsat series. The temperature-defined plant growing season depicted well the growing stages of paddy rice in temperate zones. However, the relationship between LST dynamics and the paddy rice growing season at the pixel level might be different at the regional level.

2.4.4 Future work and challenges

MODIS data (MOD09A1) have the advantage of higher temporal resolution (8 days) than Landsat 8 (16 days), which increases its ability to capture the flooding period. However, the lower spatial resolution of MODIS data (500 m versus Landsat 8's 30 m) presents the problem of mixed pixels in fragmented areas where paddy rice plots are smaller than 500 m. Combining of MODIS data and Landsat 8 data is a potential solution to improve the accuracy and spatial resolution of paddy rice mapping (Wang et al. 2015). The phenology-based paddy rice mapping algorithm, developed in the temperate region with complex landscapes of paddy rice and natural wetland, has the potential to be applied in areas with similar climate system and ecosystems, which can provide more accurate paddy rice map for food production, water resource management, and methane emission estimation. There is still a need to develop a more accurate Landsat and/or MODIS based natural wetland mask in the future to further improve the accuracy of the paddy rice mapping.

Cloud and cloud shadow with the flooding feature of a high water-related index (LSWI) are identified as flooding pixels and may affect paddy rice mapping. Improved cloud and cloud shadow algorithms can be used to reduce their residual contamination. The combination of optical and radar sensors is a way to take advantage of both optical and radar remote sensing in order to map paddy rice (Yang et al. 2008; Zhang et al. 2009).

The selection of images in the flooding period was based on the crop calendar, local weather data, and LST data from MODIS. Local crop calendar and weather data are difficult to collect and might not be enough to reflect the regional conditions. LST data from satellites can be used to support image selection in large area paddy rice mapping. The relationship between LST dynamics and the paddy rice growing season needs to be investigated in different climate zones. Extreme weather events, including delays of temperature in spring and flooding events during the paddy rice flooding/transplanting period, raise several more challenges to paddy rice mapping.

2.5 Conclusion

This study aimed to use MODIS and Landsat 8 imagery to map paddy rice in the Panjin Plain, Northeastern China, which represents our continual efforts to provide more accurate and updated paddy rice maps by studying unique spectral features of the rice crop system. We generated the paddy rice map of the Panjin Plain at a 30 m spatial resolution based on the pixel- and phenology-based algorithm in a region with a coexistent paddy rice and wetland landscape. The validation tests indicated the high accuracy of our paddy rice map. Comparison of this map with other paddy rice products yielded high levels of consistency and revealed that this map provided more detailed

information about the distribution of paddy rice areas because of its higher spatial resolution. The resultant paddy rice map might be affected by the data availability and quality (cloud and cloud shadow) during the critical plant growing stage (flooding/inundation). With the improvement of cloud and cloud shadow detection and LST retrieval from Landsat 8, it has great potential to provide reliable, sustainable data for paddy rice mapping in the future. The combination of Landsat 7, 8, and MODIS imagery can open up many more possibilities for the mapping of paddy rice in complex landscapes.

Supplementary materials

1. The paddy rice mapping using ISODATA and Support Vector Machine (SVM)

To compare our paddy rice map with the results from the conventional unsupervised and supervised classification methods, we included ISODATA (an unsupervised classification) and SVM (a supervised classification) to map paddy rice in the Panjin Plain (Chang and Lin 2001; Tou and Gonzalez 1974). ISODATA relies on the spectral signature of images and doesn't need the prior-knowledge (Xie et al. 2008). The post-classification processes (e.g combine classes) are usually needed for producing reasonable results. SVM is derived from statistical learning theory and applied through machine learning (Burges 1998; Mountrakis et al. 2011). The training samples are needed to support the SVM classification.

The Landsat OLI image in DOY 159 (6/8/2013) was used for ISODATA and SVM classification when paddy rice was still in flooding period and reed wetland was not. The image is clear with little could cover (Fig. S2.1). We set the number of classes as 15 for the ISODATA and then combined different classes into paddy rice, reed

wetland, and others in the pose-classification process (Fig. S2.2) based on the high-resolution images from Google Earth and field photos. For the SVM classifier, we used the same ROIs generated in the accuracy assessment (section 2.2.5) to support the classification (Fig. S2.3). In order to validate the results and give quantitative comparison of the different classification methods, we computed the confusion matrix for the resultant paddy rice maps from ISODATA (Table S2.1) and SVM classification (Table S2.2) using the same ROIs data as in the validation of the pixel- and phenology based paddy rice map.

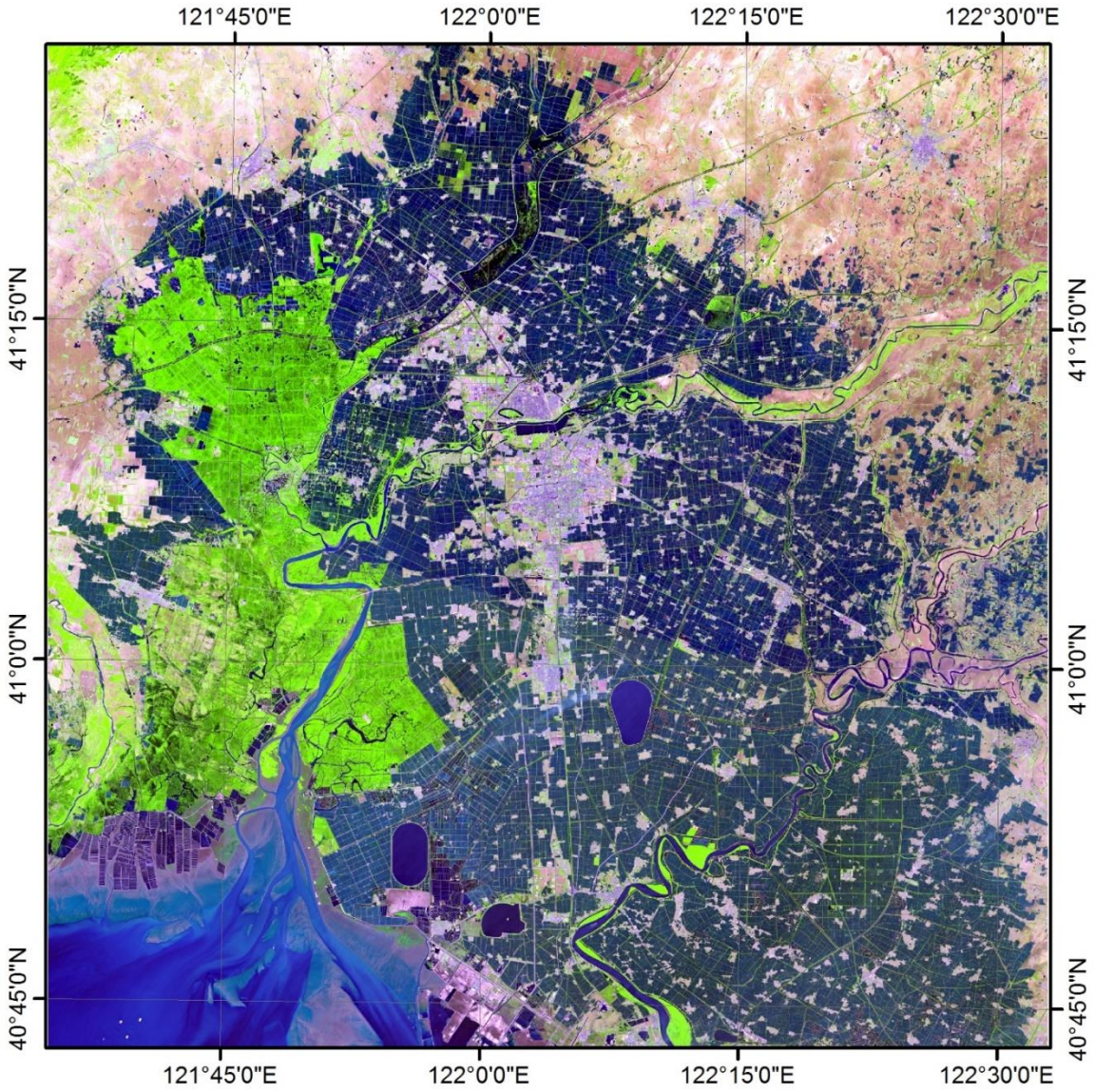


Figure S2.1 False composite displayed Landsat OLI image in DOY 159 (6/8/2013) with red (SWIR), green (NIR) and blue (red).

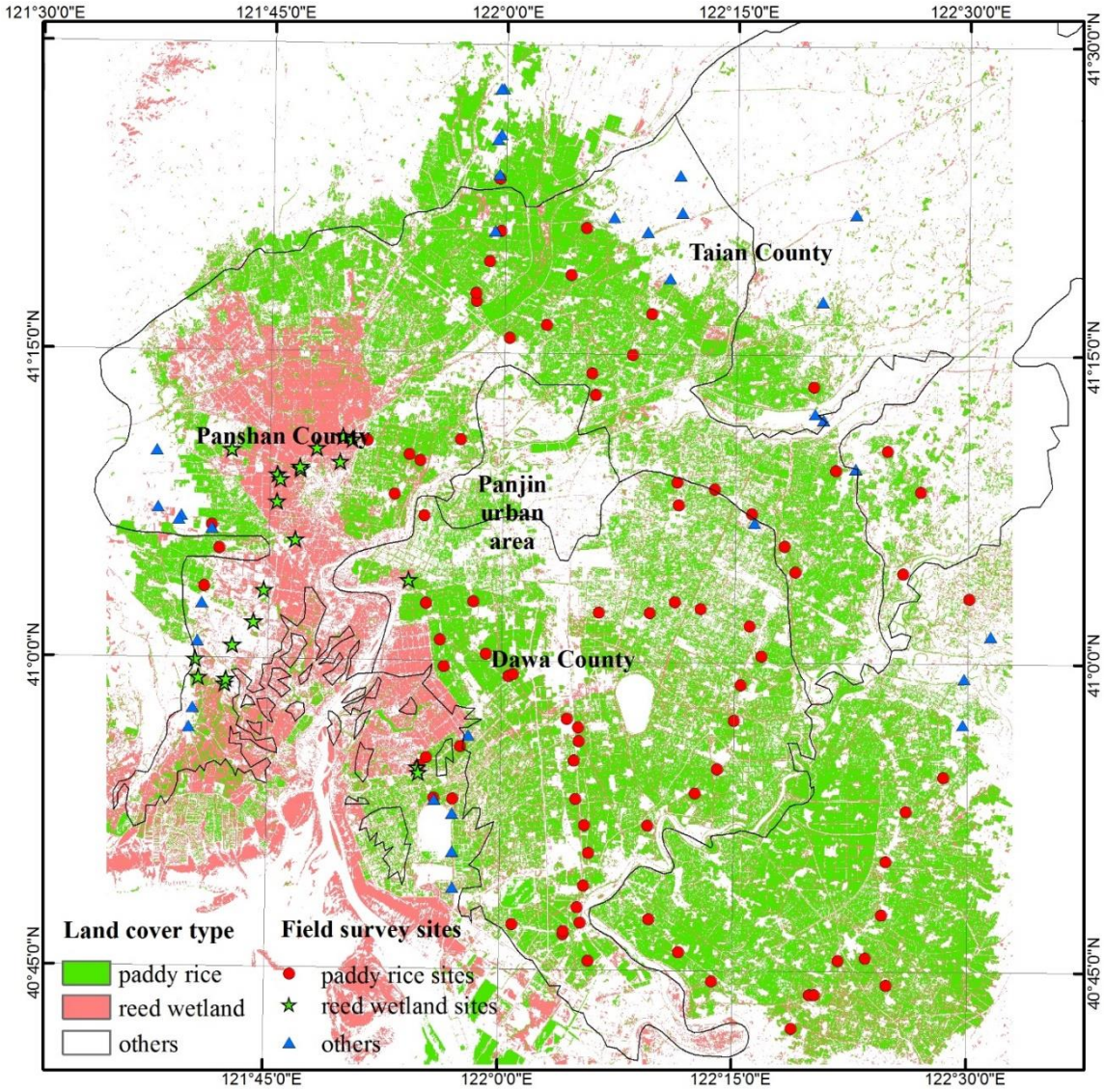


Figure S2.2 The resultant paddy rice map of the Panjin Plain derived from Landsat OLI data in DOY 159 (the paddy rice flooding period) using ISODATA.

Table S2.1. The confusion matrix between the paddy rice map derived using ISODATA classification and ROSs from geo-reference field photos in the field survey and high resolution images in Google Earth.

	Class	Ground truth (GT) samples (pixels)				
		Paddy rice	Others	Total classified pixels	User Acc. (%)	Commission errors (%)
Classification	Paddy rice	2727	866	3593	76	24
	Others	858	6593	7451	88	12
	Total GT pixels	3585	7459	11044		
	Pro.Acc. (%)	76	88			
	Omission errors (%)	24	12			

Overall accuracy 84%

Kappa coefficient 0.64

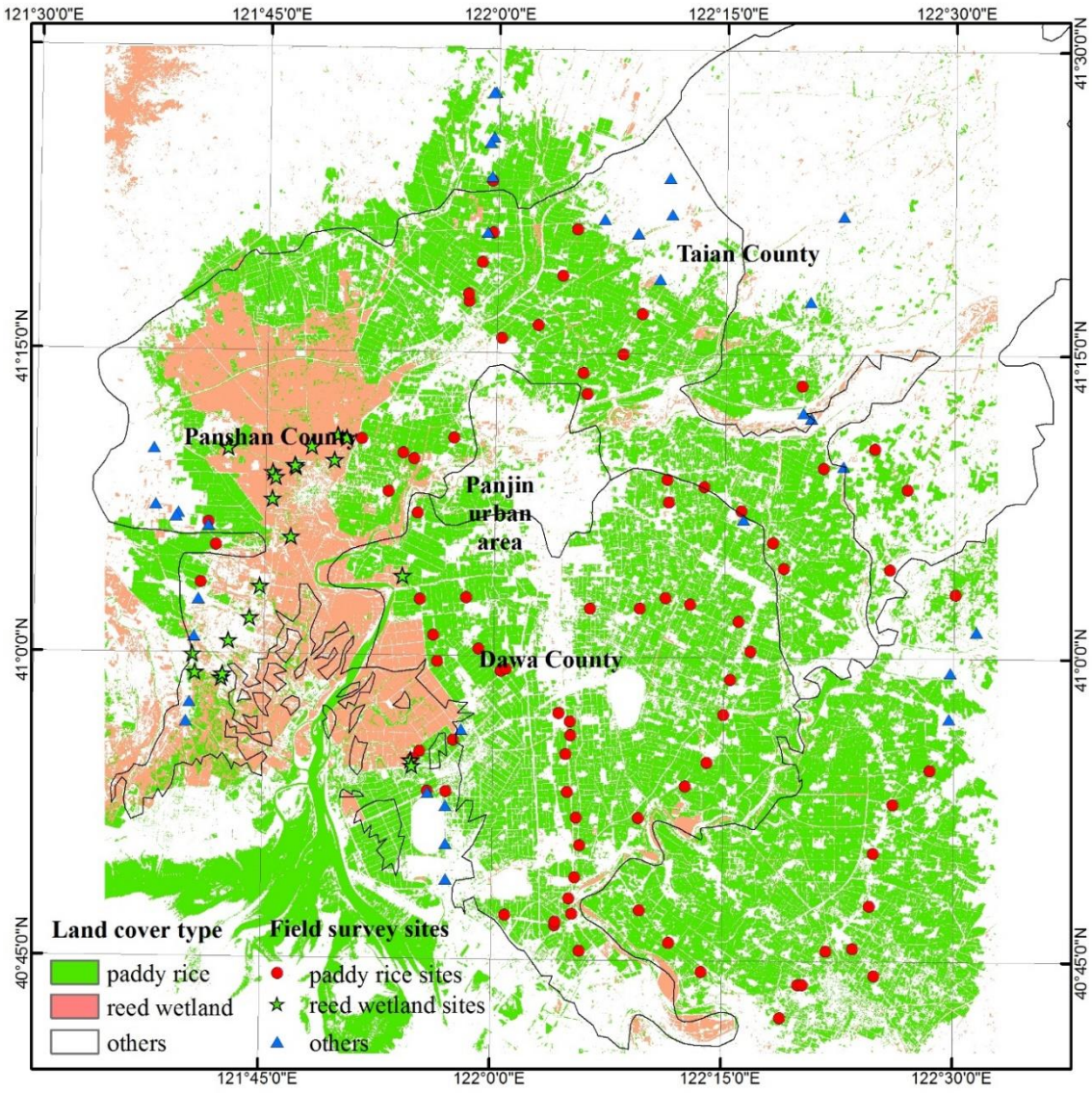


Figure S2.3 The resultant paddy rice map of the Panjin Plain derived from Landsat OLI data in DOY 159 (the paddy rice flooding period) using Support Vector Machine (SVM).

Table S2.2. The confusion matrix between the paddy rice map derived using ISODATA classification and ROSs from geo-reference field photos in the field survey and high resolution images in Google Earth.

	Class	Ground truth (GT) samples (pixels)				
		Paddy rice	Others	Total classified pixels	User Acc. (%)	Commission errors (%)
Classification	Paddy rice	3430	491	3921	87	13
	Others	155	6968	7123	98	2
	Total GT pixels	3585	7459	11044		
	Pro.Acc. (%)	96	93			
	Omission errors (%)	4	7			

Overall accuracy 94%

Kappa coefficient 0.87

Chapter 3: Examining the short-term impacts of diverse management practices on plant phenology and carbon fluxes of Old World bluestems pasture

Abstract

Burning, grazing, and baling (hay harvesting) are common management practices in grassland. To develop and adopt sustainable management practices, it is essential to better understand and quantify the impacts of management practices on plant phenology and carbon fluxes. In this study, we combined multiple data sources, including *in-situ* PhenoCam digital images, eddy covariance data, and satellite data (Landsat and Moderate Resolution Imaging Spectroradiometer (MODIS)) to examine the impacts of burning, baling, and grazing on canopy dynamics, plant phenology, and carbon fluxes in a pasture in El Reno, Oklahoma in 2014. Landsat images were used to assess the baling area and the trajectory of vegetation recovery. MODIS vegetation indices (VIs) were used in the Vegetation Photosynthesis Model (VPM) to estimate gross primary production (GPP_{VPM}) at a MODIS pixel for the flux tower (baled) site. For comparison between baled and unbaled conditions, we used MODIS VIs for a neighbor MODIS pixel (unbaled) and ran VPM. Daily PhenoCam images and green chromatic coordinate (GCC) tracked canopy dynamics and plant phenology well. The grassland greened up immediately after burning in April. GCC values showed two peaks with the similar magnitude because of quick recovery of grassland after baling. Satellite-derived VIs and GPP_{VPM} showed that the pasture recovered in one month after baling. The GPP_{VPM} matched well (R^2 = 0.89) with the eddy covariance-derived GPP (GPP_{EC}). Grazing in the late growing season did not influence plant phenology (VIs and

GCC) and carbon uptake (GPP) as plants were in the late growing stage. Neither did it affect GPP differently in those two conditions because of even grazing intensity. The reduction in GPP after baling was compensated by higher GPP after large rain events in late July and early September, causing little seasonal differences in GPP (-0.002 g C m^{-2} day^{-1}) between the baled and unbaled conditions. Interactions of different management practices with climate make it complicated to understand the impacts of different management practices on carbon dynamics and plant phenology. Thus, it is necessary to further investigate the responses of pastures to different management practices under different climate regimes at multiple temporal and spatial scales.

3.1 Introduction

Grassland (both native prairie and planted/introduced pasture) is a major forage feed for millions of beef cattle in the Great Plains of the United States. Management practices in pasture are diverse (e.g., burning, grazing, baling, fertilizing), complex (e.g., mixture of management practices such as grazing and baling, different duration and timing), and can vary over space and time. Prescribed burning is a recommended management practice to recycle plant nutrients, remove senesced vegetation, and to control weeds and inhibit woody species encroachment (Brockway et al. 2002; Reinhart et al. 2016; Twidwell et al. 2013; Valkó et al. 2014). Grazing and baling remove aboveground biomass and reduce canopy coverage and vegetation photosynthesis. The effects of grazing on carbon fluxes (e.g., gross primary production, GPP) vary under different ecological conditions and grazing intensity (Rogiers et al. 2005). Field experiments that mechanically clip vegetation to mimic hay or biofuel feedstock harvest, showed that grassland ecosystems may not be a sink of carbon depending on

the amount of biomass removal (Luo et al. 2009; Niu et al. 2013; Wagle and Kakani 2014). These management practices can have multiple impacts on vegetation canopy, phenology, and carbon dynamics (Campioli et al. 2015; Wilson et al. 2013). Thus, it is a challenging task to track those management practices and assess their impacts on pasture as well as beef cattle production.

A number of tools are available to study the impacts of management practices on vegetation phenology and carbon fluxes of grasslands, including *in-situ* digital cameras (PhenoCam), eddy covariance (EC) measurements, and satellite remote sensing. PhenoCam takes multiple digital photography in a day and provides "near surface" observations of plant phenology with high temporal resolution (Migliavacca et al. 2011; Richardson et al. 2009). Satellite remote sensing acquires consistent and periodic observations of the land surface to track vegetation phenology (Zhang et al., 2003). Vegetation indices (VIs) derived from satellite images are also used in production efficiency models to estimate gross and net primary production of vegetation (Potter et al. 1993; Running et al. 2004; Sims et al. 2008; Wu et al. 2010; Xiao et al. 2004b; Xiao et al. 2004c; Yuan et al. 2007). Because of the higher temporal resolution (8-day), the Moderate Resolution Imaging Spectroradiometer (MODIS) is used more often in GPP modeling than Landsat which has a higher spatial resolution (30 m) but lower temporal resolution (16-day). EC observations reflect effects of land use and management on the exchange of carbon dioxide, water vapor, and energy fluxes (Chi et al. 2016; Fischer et al. 2012; Owensby et al. 2006; Suyker et al. 2003). As the footprint of eddy flux tower is often comparable with the spatial resolution of the MODIS surface reflectance products, EC-derived GPP (GPP_{EC}) are widely used to evaluate modeled

GPP using MODIS data (Dong et al. 2015; Jin et al. 2013a; Sims et al. 2008; Wagle et al. 2014; Wu et al. 2010; Yuan et al. 2007).

Although field experiments help to examine the effects of management practices on carbon dynamics (Luo et al. 2009; Niu et al. 2013; Wagle and Kakani 2014), the influence of management practices on canopy scale carbon dynamics is not well understood, necessitating the integration of EC and remote sensing observations to study the effects of grazing, baling, or other management practices on canopy and carbon dynamics. Ideally, paired towers are needed in both the control and manipulated (e.g., unbaled and baled) area for the comparison. However, the high construction cost and logistical requirements of EC systems prohibit the utilization of paired towers in most cases (Chi et al. 2016; Fischer et al. 2012). Alternatively, modeling approaches can be used. Remote sensing-based production efficiency models estimate GPP as the product of the absorbed photosynthetically active radiation (APAR) and light use efficiency (LUE, Ɛg) (Potter et al. 1993; Running et al. 2004; Xiao et al. 2004a; Xiao et al. 2004b; Yuan et al. 2007). Most of these models use VIs and meteorological parameters as inputs. In the case of a single eddy flux tower site with disturbances or management practices, VIs of the nearby undisturbed area of similar vegetation cover, can be combined with the meteorological parameters of the flux tower site to simulate GPP for the undisturbed condition. By comparing the two scenarios (e.g., baled and unbaled), we can show the effects of management practices or disturbances on GPP.

The objective of this study is to examine the impacts of burning, baling, and grazing on canopy and carbon fluxes in a pasture through integrating PhenoCam images, satellite remote sensing, and eddy covariance data. In addition, the impacts of

management practices (e.g., baling and grazing) on GPP were investigated using the satellite-based vegetation photosynthesis model (VPM) for disturbed and undisturbed conditions. This case study, using multiple observation techniques to detect the impacts of diverse management practices, can serve as an example of utilizing different data sources to better understand the impacts of management practices on vegetation phenology and carbon fluxes.

3.2 Materials and methods

3.2.1. Study site description

The study site (Fig. 3.1) is located at the United States Department of Agriculture—Agricultural Research Service (USDA-ARS) Grazinglands Research Laboratory (GRL) in El Reno, Oklahoma (35.54679ºN, 98.04529ºW, 435 m above sea level). The field (red rectangle in Fig. 3.1) is an introduced warm-season, pasture which

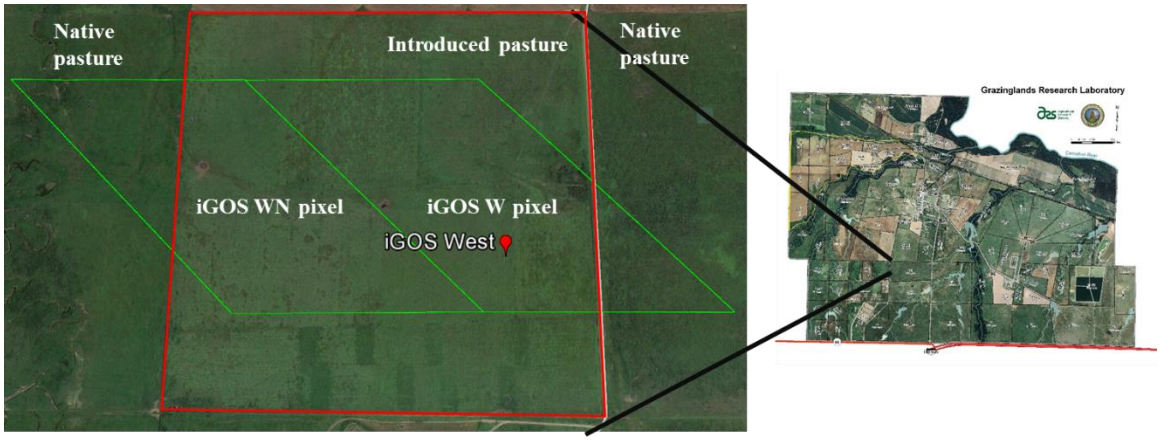


Figure 3.1. Location of flux tower site and overlapping with MODIS pixels. Location of the flux tower site is marked as red point and labeled. Red rectangle is the boundary of the study field. Green diamonds are boundaries of MODIS pixels.

was planted with old world bluestem (*Bothriochloa caucasica* C. E. Hubb.) (Samuel and Forbes 1998). The pasture's soil is classified as Norge silt loam (Fine-silty, mixed,

active, thermic Udic Paleustolls) (Staff 1999) with a depth greater than 1 m and high water holding capacity (Fischer et al. 2012).

Several management activities (e.g., burning, fertilizer and herbicide applications, baling for hay, and cattle grazing) were implemented at the site in the same year (2014). The field was burned on April 9th (DOY 99) and sprayed on May 1st with herbicide (2.35 l/ha of GRAZON) and followed immediately by fertilizer (44.8 kg N/ha 46-0-0) application. In late July, part of the eastern half of the field close to eddy flux tower was cut for hay and baled on July 23rd (DOY 204, the first baling). The remaining part of the eastern half was cut for hay in early August and baled on August 15th (DOY 227, the second baling). Twenty five cows with an average weight of 520 kg continuously grazed the entire field from September 25th (DOY 268) until end of the calendar year.

3.2.2. Eddy flux tower site and EC data processing

The EC system was deployed at the beginning of May 2014 to measure fluxes of CO_2 and H_2O using a LI-7500 A (LI-COR Biosciences Inc., NE, USA) and CSAT3 sonic anemometer (Campbell Scientific Inc., UT, USA). PhenoCam (StarDot Technologies, CA, USA) images, and other meteorological variables such as surface energy balance components, air temperature, relative humidity, soil temperature, soil water content at 25 cm (SWC), and solar radiation were also included as part of an integrated Grassland Observation System in the west of GRL (iGOS W). The Oklahoma Mesonet El Reno site is 800 m to the east of iGOS W which provides quality-controlled measurements of meteorological and land-surface variables such as precipitation, temperature, and soil moisture at intervals spanning 5-30 minutes depending on the

variables (McPherson et al. 2007) (http://www.Mesonet.org/). Precipitation, photosynthetically active radiation (PAR), air temperature, and SWC at 25 cm are presented in Fig. 3.2.

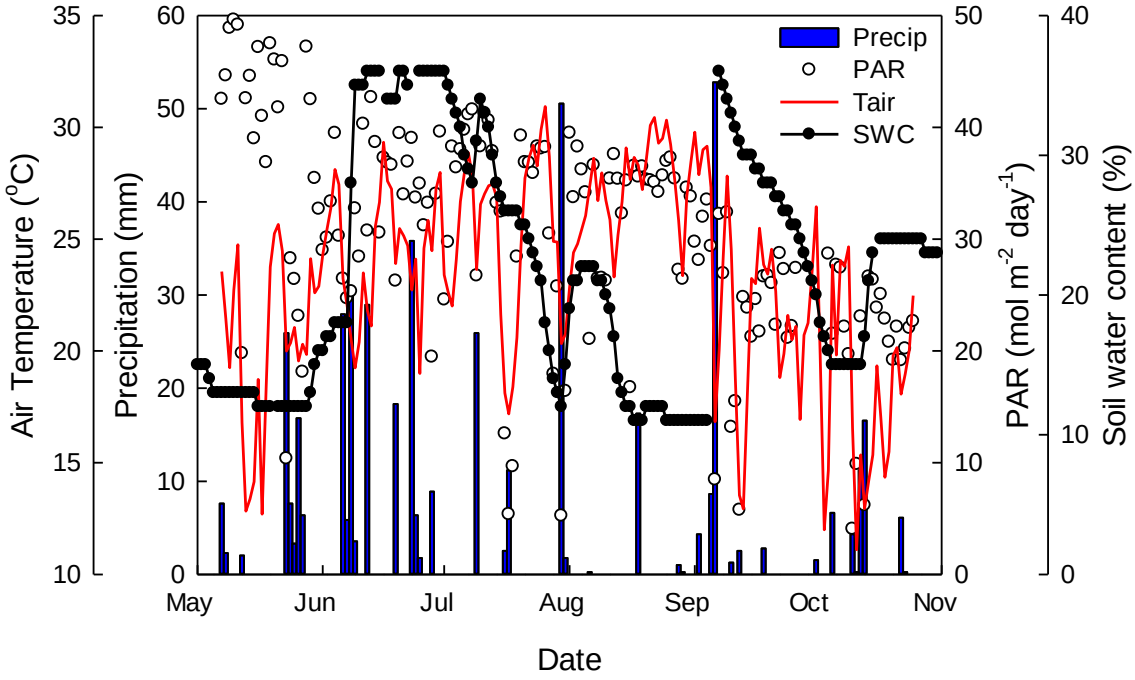


Figure 3.2. Seasonal dynamics of photosynthetically active radiation (PAR), precipitation (Precip), air temperature (Tair), and soil water content (SWC) at 25 cm observed at the flux tower site/nearby Mesonet site. Each data point represents daily average.

The raw 10 Hz EC data were processed using EddyPro software version 5.1.1 (LI-COR Biosciences Inc., NE, USA) to produce 30-min fluxes of CO_2, H_2O, and energy. The EddyPro output results were further screened based on quality assurance/quality control (QA/QC) flags [i.e., fluxes with quality flags of '2 (bad quality)' were rejected]. In addition, fluxes beyond the reliable range of fluxes [i.e., net ecosystem CO_2 exchange, NEE: beyond ±50 μmol m^{-2} s^{-1} (Zeeman et al. 2010)] were also excluded. The EddyPro also provides flux footprint estimations which can show

the contribution of flux measurements from different directions and distances for different periods (before and after baling).

Gaps in the flux data were filled using a moving lookup table approach which considers both the covariance of fluxes with meteorological variables and temporal auto-correlation of fluxes (Reichstein et al. 2005). The NEE was partitioned into GPP and ecosystem respiration (ER) based on the temperature sensitivity of ER (Lloyd and Taylor 1994). Both gap filling and partitioning were conducted using the online R package "REddyProc" (https://www.bgc-jena.mpg.de/bgi/index.php/Services/REddyProcWebRPackage), developed at the Max Planck Institute for Biogeochemistry, Jena, Germany (Moffat et al. 2007; Reichstein et al. 2005). Daily sums of NEE, ER, and GPP were presented to show the carbon dynamics for the growing season in 2014 (May-October).

3.2.3. PhenoCam images and greenness index

Canopy images were collected with a StarDot NetCam SC camera installed in a weatherproof enclosure at a height of 3.0 m above the ground. The camera was pointed south and set at an angle of about 20^{o} below horizontal. The camera provides regular RGB images for the same scene as the camera position was fixed. Various greenness indices can be derived from the PhenoCam images to detect the plant phenology (Richardson et al. 2007). For this study, the green chromatic coordinate (GCC) value was used to indicate the vegetation status for one specific "Region of Interest" (ROI) located in the baling affected area (black rectangle showed in Fig. 3.3e) using the following equation (Eq. 1):

$$GCC = \frac{G_{DN}}{R_{DN}+G_{DN}+B_{DN}} \quad (1)$$

where R_{DN}, G_{DN}, B_{DN} are RGB digital numbers (DN). The time series of GCC values were calculated using the PhenoCam toolkit from PhenoCam network (https://phenocam.sr.unh.edu/webcam/tools/).

3.2.4. MODIS images and VIs

The 8-day composite MODIS surface reflectance product (MOD09A1) (Vermote and Vermeulen 1999) was used to investigate the seasonal dynamics of the VIs for the flux tower located pixel (iGOS W) and for its neighbor pixel (iGOS WN) (Fig. 3.1). The majority of both iGOS W and iGOS WN MODIS pixels are old world bluestem pasture. Both pixels were burned and received applications of fertilizer and herbicide. The first baling only affected iGOS W and the second baling did not affect both pixels which was to the south of the iGOS W pixel. MOD09A1 has reflectance values of the seven spectral bands: blue (459-479 nm), green (545-565 nm), red (620-670 nm), two near infrared (NIR_1: 841-876 nm; NIR_2: 1230-1250 nm), and two shortwave infrared ($SWIR_1$: 1628-1652 nm, $SWIR_2$: 2105-2155 nm) at a 500-m spatial resolution. It also includes quality control flags for consideration of various image artifacts (e.g., clouds and cloud shadow). All data that did not pass the quality control were excluded in further analysis based on the following criteria: cloud state flag indicates cloudy or mixed, or cloud shadow existence, or aerosol quantity flag shows high, or cirrus detected flag is average or high.

Normalized Difference Vegetation Index (NDVI), Enhanced Vegetation Index (EVI), and Land Surface Water Index (LSWI) were calculated from MOD09A1 using surface reflectance (ρ) from blue (ρ_{blue}), red (ρ_{red}), NIR_1 (ρ_{nir}, 841-876 nm), and $SWIR_1$ (ρ_{swir}, 1628-1652 nm) bands (Eq. 2-4). The coefficients C1, C2, and L are 6.0,

7.5, and 1.0, respectively, and G is a gain factor set to 2.5 in EVI calculation (Huete 2002). EVI and LSWI were also used in VPM to simulate GPP. Bad observations of EVI and LSWI values were linearly interpolated using good, nearby observations.

$$NDVI = \frac{\rho_{nir} - \rho_{red}}{\rho_{nir} + \rho_{red}} \quad (2)$$

$$EVI = G \times \frac{\rho_{nir} - \rho_{red}}{\rho_{nir} + C1 \times \rho_{red} - C2 \times \rho_{blue} + L} \quad (3)$$

$$LSWI = \frac{\rho_{nir} - \rho_{swir}}{\rho_{nir} + \rho_{swir}} \quad (4)$$

3.2.5. Landsat images and VIs

Landsat has higher spatial resolution than MODIS (30 m vs. ~500 m). The baled area was smaller than one MODIS pixel which could introduce error if the baling areas are not examined using higher spatial resolution images. Landsat surface reflectance product (Landsat 7 ETM+ and Landsat 8) covering the study area were downloaded from the USGS EarthExplorer (http://earthexplorer.usgs.gov/) and the images for the study area were extracted. Landsat 8 does not have the same data gap problem as Landsat 7 ETM+ and keeps the same spatial resolution (30 m) (Roy et al. 2014). Fortunately, our study area is located in the center of the image tiles and was not affected by the gaps in Landsat 7 data. Thus, both Landsat 7 ETM+ and Landsat 8 images were included in the analysis. The data quality control approach is similar to use of Landsat imagery in a previous study to exclude the effect of clouds and cirrus observations (Zhou et al. 2016). Shortwave infrared (SWIR-2), near infrared (NIR), and red bands were used to construct false color composite images for use in reducing atmospheric effects and highlight vegetation. EVI and LSWI values for iGOS W and

iGOS WN were calculated using Landsat pixels in the corresponding MODIS pixels. The EVI and LSWI differences between iGOS W and iGOS WN derived from MODIS and Landsat for the same period were used to investigate the comparability of these two satellite observations.

3.2.6. Vegetation Photosynthesis Model

The Vegetation Photosynthesis Model (VPM) (Xiao et al. 2004b; Xiao et al. 2004c) estimates GPP as the product of light use efficiency (ε_g) and absorbed photosynthetically active radiation (APAR) by chlorophyll,

$$GPP_{VPM} = \varepsilon_g \times APAR_{chl} \quad (5)$$

$$APAR_{chl} = fPAR_{chl} \times PAR \quad (6)$$

where $fPAR_{chl}$ is the fraction of PAR absorbed by chlorophyll which is estimated as a linear function of EVI where the coefficient a is set to be 1.0 (Xiao et al. 2004b).

$$fPAR_{chl} = a \times EVI \quad (7)$$

The ε_g is derived by down-regulating the theoretical maximum light use efficiency (ε_0) with scalars of temperature (T_{scalar}) and water (W_{scalar}) stresses.

$$\varepsilon_g = \varepsilon_0 \times T_{scalar} \times W_{scalar} \quad (8)$$

More information about the T_{scalar} and W_{scalar} can be found in previous studies (Wagle et al. 2014; Xiao et al. 2004b; Xiao et al. 2004c).

The site-specific ε_0 is usually determined using a rectangular hyperbola light-response function (NEE-PAR relationship) at 30-minute intervals during peak growing season (Falge et al. 2001). For this study the ε_0 is set to be 0.062 mol CO_2 mol^{-1} PPFD (PPFD represents photosynthetic photon flux density) which was used for nearby tallgrass prairie sites in a previous study (Wagle et al. 2014).

We first ran VPM for flux tower located MODIS pixel to determine GPP for iGOS W (GPP_{VPM_W}). Then we used the same PAR, air temperature and VIs of the nearby MODIS pixel to simulate GPP for iGOS WN (GPP_{VPM_WN}). This substitution should introduce minimal error as PAR and air temperature do not vary significantly at the scale of one MODIS pixel (~500 m) in flat terrain. GPP_{VPM_W} was compared with the EC derived GPP (GPP_{EC}) to evaluate the performance of VPM. The dynamics of GPP_{VPM_W} and GPP_{VPM_WN} were plotted to visually examine the course of grassland recovery after disturbance due to different management practices (e.g., baling). The differences in GPP sums between the two MODIS pixels indicate the cumulative impacts of disturbances/management practices.

3.2.7. Statistical analysis

A simple linear regression model was used to investigate the relationship between GPP_{EC} and EVI (one of the major inputs in VPM). GPP_{EC} and GPP_{VPM_W} values were compared to assess the validity of the model. The coefficient of determination (r^2) was used to evaluate the model agreement in both statistical analyses. To show the impacts of different management practices, we tabulated GPP for iGOS W and iGOS WN for different periods.

3.3 Results

3.3.1. Canopy dynamics and plant phenology in response to management practices as observed by PhenoCam, Landsat, and MODIS images

3.3.1.1 Canopy dynamics and GCC values in response to management practices as observed by PhenoCam images

The real-time images from PhenoCam showed different management practices (burning, baling, and grazing) and phenology of the grassland (Fig. 3.3) occurred within its field of view. The quick recovery of grasses after baling was also observed in the time-series of PhenoCam images (Fig. 3.3d and f). The chronology of management practices (the time and period), climate events (rain), and plant phenology is shown in Fig. 3.4. The GCC values derived from PhenoCam images showed the daily growth dynamics of the vegetation (Fig. 3.5). The green-up, peak growing season, and senescence stages were clearly reflected by GCC values. While the range of GCC values was small (0.32-0.38), the GCC values showed two peaks at early May and mid-August with the magnitude of 0.37-0.38, whereas GCC values during senescence were around 0.34. As expected, the GCC values decreased after baling. However, grazing in the late growing season (September 25th - end of the year) did not affect GCC values.

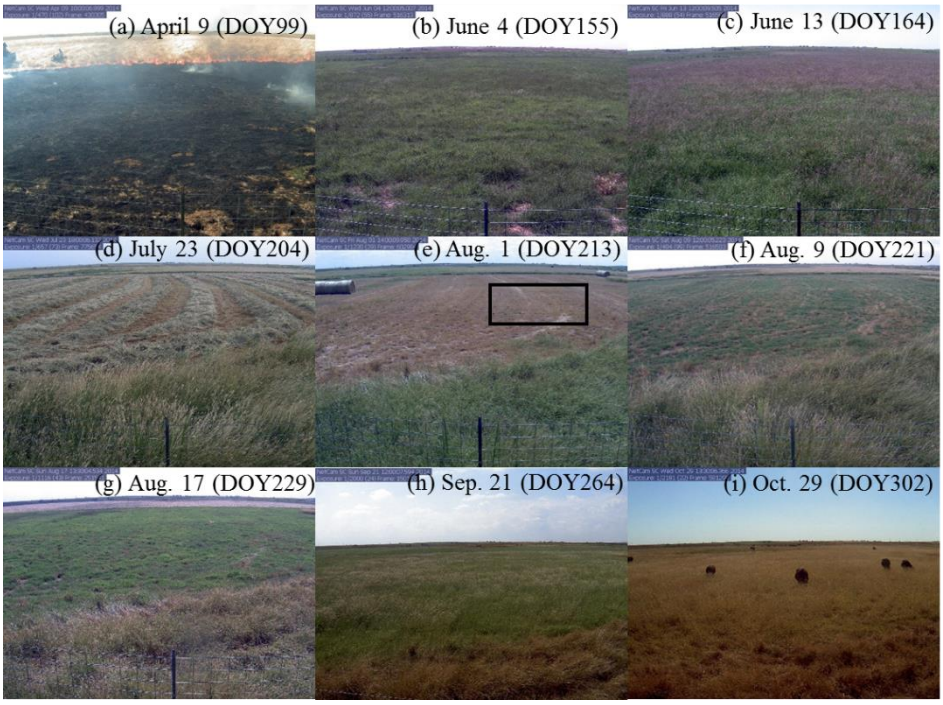


Figure 3.3. PhenoCam images showing management practices and phenology of grassland. The black rectangle in panel e shows the region of interest (ROI) used to calculated GCC values.

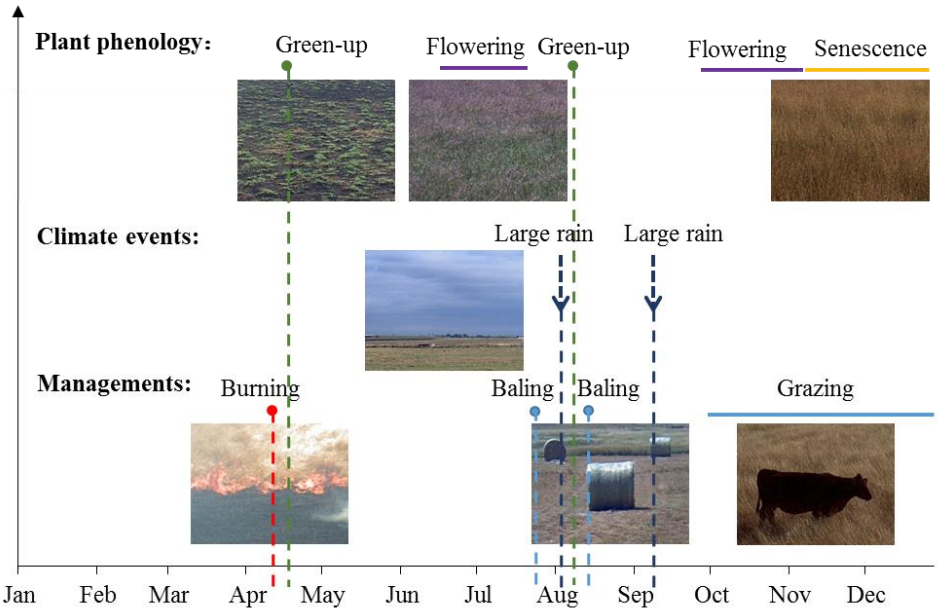


Figure 3.4. Management practices, climate events, and plant phenology in the field. The plant phenology was delineated through interpreting individual time series PhenoCam images.

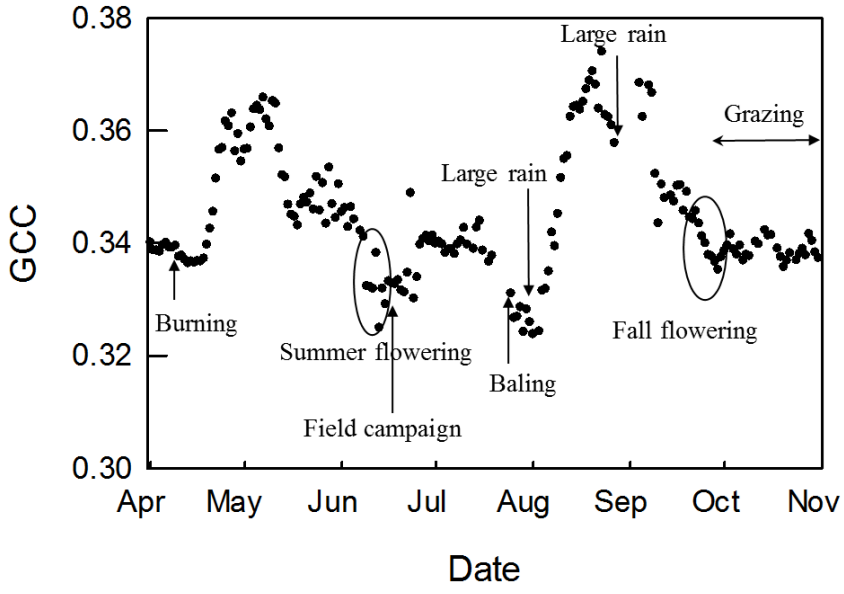


Figure 3.5. Daily GCC values from PhenoCam images.

3.3.1.2. Canopy dynamics and plant phenology in response to management practices as observed by Landsat images

The time-series images from Landsat 8 and Landsat 7 ETM+ clearly showed the areas affected by burning and the two baling events (Fig. 3.6b, d, and f). The Landsat images showed some heterogeneity within the corresponding MODIS pixels. For example, the first baling mostly affected the center of the MODIS pixel for iGOS W (around 67% of the pixel affected) (Fig. 3.6d). The second baling affected only the area to the south of the MODIS pixel for iGOS W (Fig. 3.6f). From these images, we can see that the vegetation phenology of the field was quite different than areas outside since the study site is covered by introduced pasture with better vegetation growth than the native pasture. The introduced pasture was much greener than the native pasture in July (Fig. 3.6c and d) before baling. The area affected by the first baling recovered quickly

after one month after cutting (Fig. 3.6d and f), which was also reflected by high GCC values in mid-August (Fig. 3.5). The second baling affected area also recovered after about one month (Fig. 3.6f and i). The introduced pasture (inside field) entered senescence stage much later than the native grassland (outside field) (Fig. 3.6h and i).

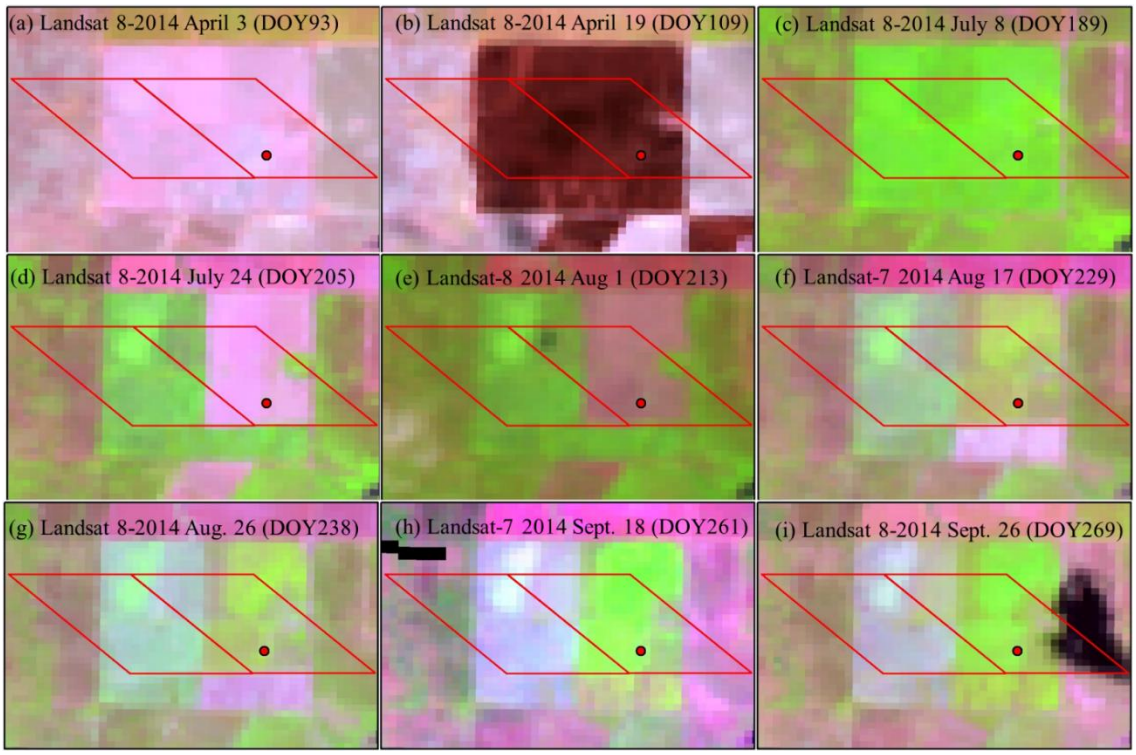


Figure 3.6. Landsat images of the study area in different periods. Location of flux tower site and boundaries of MODIS pixels are also shown.

3.3.1.3. Plant phenology in response to management practices at iGOS W and iGOS WN as observed by MODIS images

Dynamics of NDVI, EVI, and LSWI derived from MODIS images for iGOS W and iGOS WN were synchronous from January to early June and from early October to December (Fig. 3.7). The grassland greened up immediately after burning in April and entered senescence stage at the end of October. LSWI had the most significant drop

among three VIs after burning because of SWIR band embedded (Eq. 4). The lower VIs in mid-June in iGOS WN occurred because of disturbance associated with more frequent sample collection during an intensive field research campaign (Steiner 2014) that was more focused in the western part of the field, where most of MODIS pixel for iGOS WN was located (Fig. 3.1). The intensive field research campaign investigated multiple aspects of the soil (soil water content and soil greenhouse gas emission) and plant systems (canopy reflectance, leaf area index, canopy height, and aboveground biomass) through sampling soil and plants. VIs values at both MODIS pixels became very similar again at around mid-July. VIs diverged after the first baling in iGOS W on July 23rd. After two big large rain events, VIs of both pixels increased, but VIs at iGOS W increased more. Grazing in the late growing season did not cause differences in VIs between iGOS W and iGOS WN, most likely due to the similar grazing intensity.

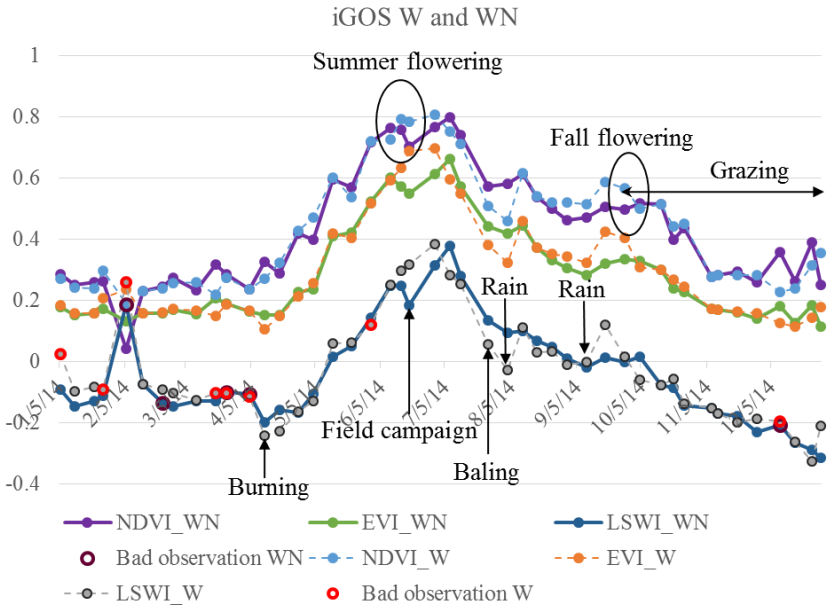


Figure 3.7. MODIS vegetation indices (VIs) for the flux tower located pixel (iGOS W) and its neighbor pixel (iGOS WN).

3.3.1.4. Differences in VIs between iGOS WN and iGOS W derived from MODIS and Landsat images

The EVI and LSWI differences between iGOS WN and iGOS W derived from MODIS images varied between -0.1 to 0.1 throughout the growing season (Fig. 3.8). The relatively larger differences in EVI and LSWI between two pixels derived from Landsat images were observed after the first baling (0.3) and during senescence (-0.1). The EVI differences derived from both MODIS and Landsat images showed that EVI in iGOS W was higher (by around 0.1) than iGOS WN at the beginning of October, which indicates re-growth of more photosynthetically active vegetation after baling.

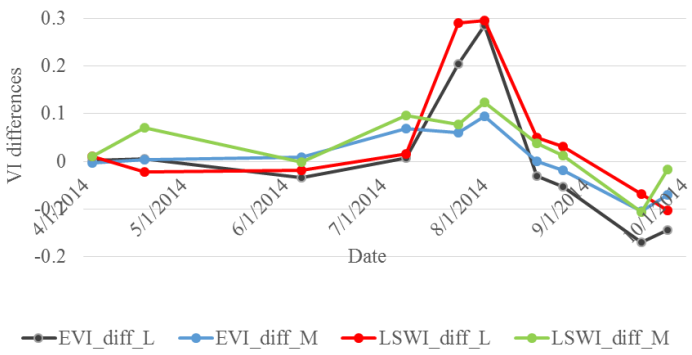


Figure 3.8. Differences in Enhanced Vegetation Index (EVI) and Land Surface Water Index (LSWI) at iGOS WN and iGOS W MODIS pixel derived from MODIS and Landsat images.

3.3.2. Carbon fluxes in response to management practices as observed by eddy flux tower

Diurnal patterns of NEE in the pasture across the growing season in 2014 are presented in Fig. 3.9. As expected, NEE increased with the increasing photosynthetic capacity and NEE rates decreased during the late growing season because of senescence of plants. The magnitude of daily NEE reached up to -11.51 g C m^{-2} day^{-1}. The iGOS W

was a carbon sink (i.e., negative NEE values) for most of the growing season until late October when it turned to carbon neutral. Baling changed NEE values from negative to positive (from carbon sink to carbon source). The magnitudes of diurnal peak NEE (monthly average) reached up to -37.33 ± 1.46 µ mol m^{-2} s^{-1} in June (leaf area index: 5.95 and aboveground biomass: 563.44 g/m^2) and declined quickly in July (-22.02 ± 2.68 µ mol m^{-2} s^{-1}). The diurnal patterns of NEE in May and July were similar. It is noteworthy to mention that NEE in September was higher than in August, which showing that the pasture was a stronger carbon sink in September than in August.

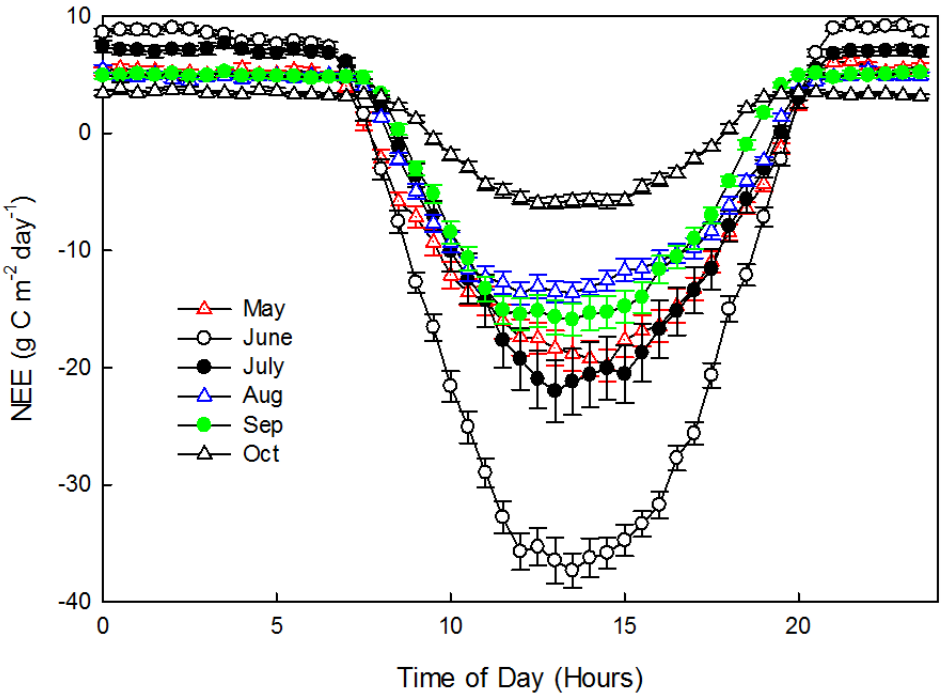


Figure 3.9. Half-hourly binned diurnal courses of net ecosystem CO_2 exchange (NEE) from May to October 2014 at the iGOS W site. Negative values of NEE indicate net carbon uptake and positive values indicate carbon release by the ecosystem. Each data point is a mean value for the specific time step for the entire month and bars represent standard errors of the means.

The seasonal pattern of GPP was similar to NEE but with the opposite sign (Fig. 3.10). The magnitude of daily GPP reached up to 21.47 g C m^{-2} day^{-1}. ER had small

variation during the growing season (approximately 5 g C m^{-2} day^{-1}) except for June and early July when it reached about 12 g C m^{-2} day^{-1}. A decreasing trend of GPP was observed after early June and dropped abruptly in mid-July because of cloudy (also indicated by very low PAR in Fig. 3.2) and windy weather (identified from PhenoCam images during this period). As expected, GPP decreased more than ER after baling, turning the grassland into a net carbon source for approximately 10 days. After that period, both GPP and NEE increased rapidly again which might have been triggered by re-growth of vegetation and two large rain events (~50 mm/day) at the end of July and early September (Fig. 3.2). These two peaks for GPP after baling had similar magnitudes (~10 g C m^{-2} day^{-1}). Grazing in the late growing season did not affect carbon dynamics substantially.

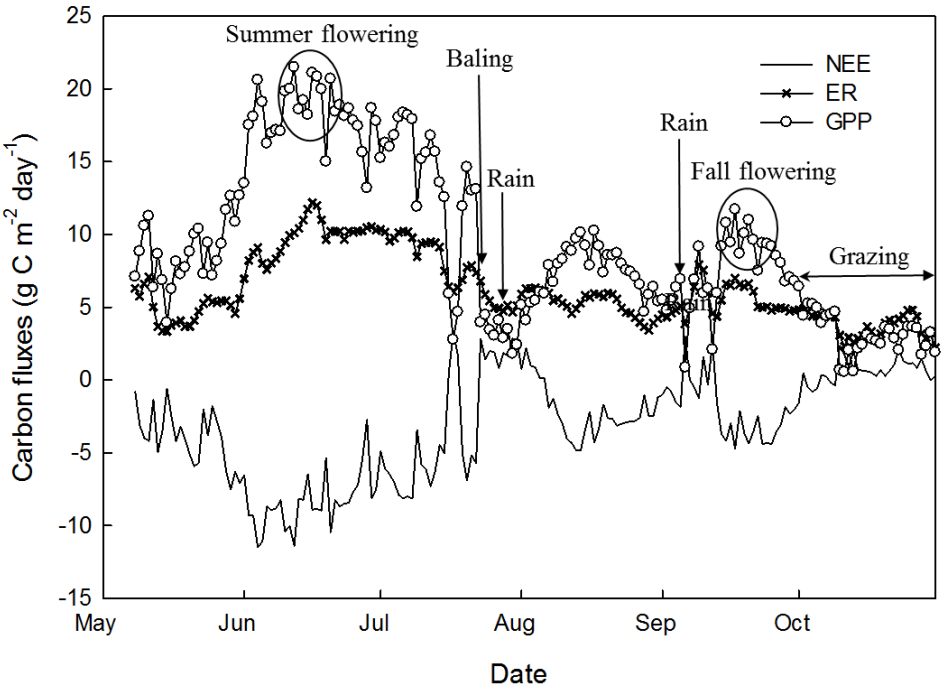


Figure 3.10. Daily sums of gross primary production (GPP), ecosystem respiration (ER), and net ecosystem CO_2 exchange (NEE) from flux tower in the 2014 growing season.

3.3.3. GPP in response to management practices and disturbance as estimated by VPM

3.3.3.1. GPP simulation from VPM

GPP_{EC} was highly correlated with EVI (Fig. 3.11a), showing the capability of EVI to track GPP. GPP_{VPM_W} captured the trends of GPP_{EC} very well (r^2 = 0.89) throughout the growing season (Fig. 3.11b). Three peaks of GPP_{EC} were also tracked by GPP_{VPM_W}. GPP_{EC} decreased sharply immediately after baling and it began to increase again with increasing greenness in the baled area, which as well captured by GPP_{VPM}. This result strengthens the comparison of GPP_{VPM} for baled and unbaled conditions. The VPM tended to underestimate GPP in the early stages of flowering (head emergence) which was detected from PhenoCam images (Fig. 3.3c and h). For example, GPP_{VPM} were smaller than GPP_{EC} values for mid-June and mid-September.

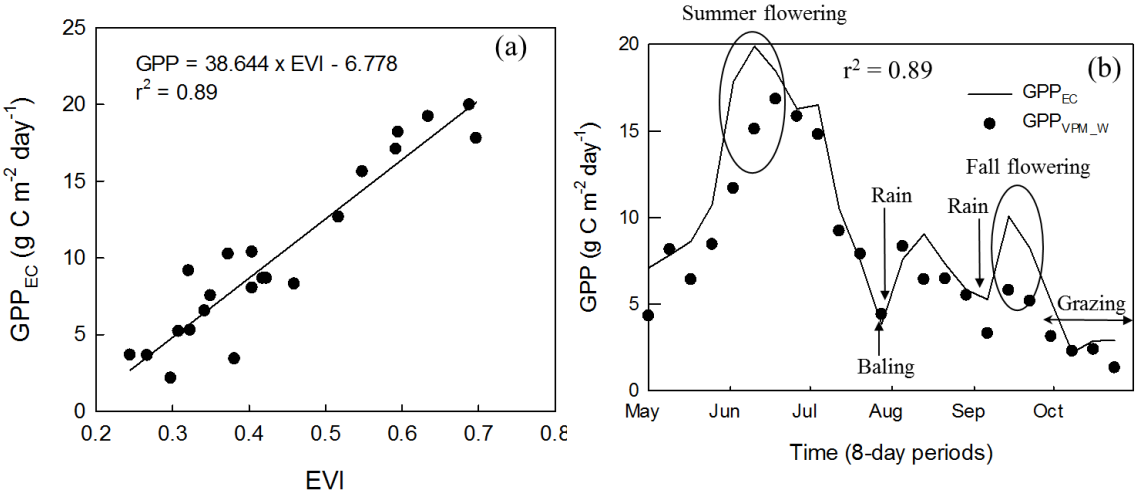


Figure 3.11. (a) Relationship between enhanced vegetation index (EVI) and gross primary production (GPP_{EC}). (b) Comparison between gross primary production (GPP) from VPM simulation and EC measurement (GPP_{VPM_W} and GPP_{EC}).

3.3.3.2 GPP in response to intensive field campaign, baling, and grazing as estimated by VPM

GPP_{VPM_W} and GPP_{VPM_WN} were very similar in May, August, and October (Fig. 3.12) because of little differences in VIs and the identical meteorological data input into the VPM. Event-based GPP statistics are presented in Table 3.1 to reflect impacts of intensive field research campaign, baling, and grazing. Before the intensive field research campaign in mid-June, GPP_{VPM_W} and GPP_{VPM_WN} were almost identical. The intensive field research campaign in iGOS WN caused the lower GPP values than in iGOS W (12.633 g C m^{-2} day^{-1} vs. 15.962g C m^{-2} day^{-1}). The GPP difference caused by the intensive field research campaign disappeared around mid-July as GPP_{VPM_W} and GPP_{VPM_WN} became similar (Fig. 3.12). Baling (July 23rd) decreased GPP_{VPM_W} by around 2 g C m^{-2} day^{-1} for the following two 8-day periods. GPP_{VPM_W} and GPP_{VPM_WN} converged again in early August and remained similar for the rest of the month. Following the large rain events in late July and early September (Fig. 3.2) both GPP_{VPM_W} and GPP_{VPM_WN} increased, with GPP_{VPM_W} having a higher magnitude because of more photosynthetically active vegetation in iGOS W after baling. This compensated for the decreased GPP due to baling and resulted in negligible difference between GPP_{VPM_W} and GPP_{VPM_WN} (-0.002 g C m^{-2} day^{-1}) for the period after baling to before grazing (July 20th - September 22th). The late growing-season grazing in the whole field did not exert different impacts at iGOS W and iGOS WN. With different management practices, the growing season average GPP was similar (7.528 g C m^{-2} day^{-1} in iGOS W and 7.286 g C m^{-2} day^{-1} in iGOS WN).

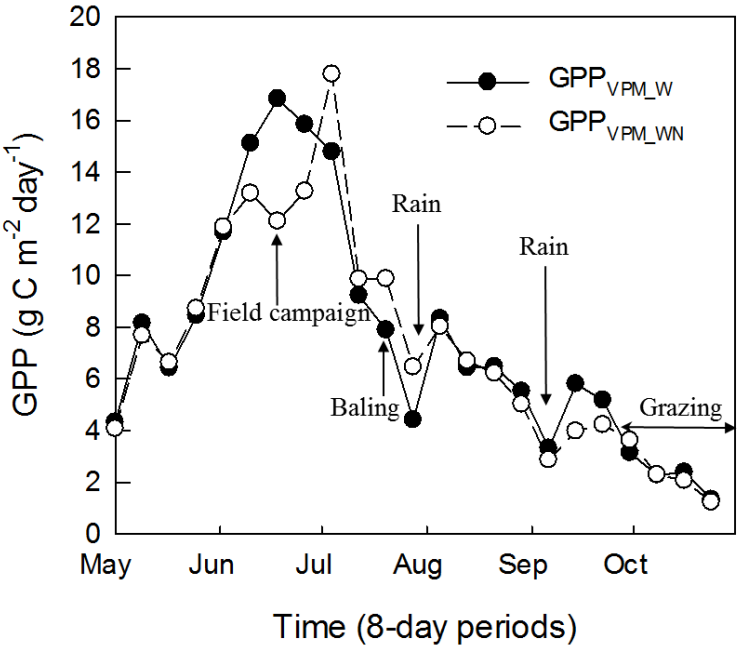


Figure 3.12. Differences in gross primary production (GPP) difference of the flux tower located pixel (iGOS W) and its neighbor pixel (iGOS WN).

Table 3.1. Event based GPP statistics for iGOS W and iGOS WN

Event	Time point or period in 8-days	GPP_{VPM_W} (g C m^{-2} day^{-1})	GPP_{VPM_WN} (g C m^{-2} day^{-1})
1. Before field campaign	May 1st - June 2nd	7.799	7.790
2. Field campaign	Mid-June		
a. 2 weeks after field campaign	June 10th - July 18th	15.962	12.633
b. 3-5 weeks after field campaign	June 26th - July 12nd	13.278	13.629
Average	June 10th - July 12nd	14.352	13.230
3. The first baling	July 23rd		
a. 2 weeks after baling	July 20th - July 28th	6.143	8.157
b. 3-7 weeks after baling	Aug. 5th - Sept. 6th	6.004	5.758
c. 8-9 weeks after baling	Sept. 14th - Sept. 22nd	5.484	4.098
Average	July 20th - Sept. 22nd	5.920	5.922
4. Grazing	Sept. 30th – Oct. 24th	2.277	2.294
Whole growing season	May 1st – Oct. 24th	7.528	7.286

3.4 Discussion

3.4.1. Necessity of utilizing multiple observations to study the impacts of management practices on plant phenology and carbon fluxes

This study incorporated PhenoCam images, satellite remote sensing products, and eddy covariance data to investigate the impacts of burning, baling, and grazing on vegetation phenology and GPP of an Old World bluestems pasture. Because of different spatial and temporal resolutions of data sources, their applications on detecting the impacts of management practices are different. Since PhenoCam provide high temporal frequency *in situ* images, it is suitable for detecting plant phenology. Satellite remote sensing has larger spatial coverage than PhenoCam which makes it suitable for investigating larger scale events (e.g. characterizing the baling affected area). The EC data quantifies the impacts of management practices on carbon fluxes and provides data to evaluate GPP models. Combination of remote sensing and EC data in VPM for disturbed and undisturbed scenarios allowed assessment of the impacts of intensive field research campaign and baling on GPP. Multiple datasets allowed an investigation of intra-annual variations caused by different management practices.

PhenoCam has been a popular tool to study plant phenology (Migliavacca et al. 2011; Richardson et al. 2007; Richardson et al. 2013). PhenoCam images vividly showed the management practices (burning, baling, and grazing) and the quick recovery of grassland after baling (Fig. 3.3). The underestimation of GPP from VPM (Fig. 3.11b) was attributed to the underestimation of VIs for the early stages of flowering (seed heads tend to have lower VIs values than leaves because of lower chlorophyll content.), which was identified from PhenoCam images (Fig. 3.3c and h and Fig. 3.5). The *in situ*

observation from PhenoCam indicated its potential applications in ecosystem management studies as an aided tool.

Satellite remote sensing provides observations at larger spatial scale than does PhenoCam but at lower temporal resolution. Free satellite remote sensing data, namely MODIS and Landsat, are suitable for different purposes depending on the temporal and spatial scales and objectives of the study. The 8-day temporal resolution of MODIS makes it well suited to quantify GPP dynamics, while the higher spatial resolution of Landsat (30 m) allows quantification of areas affected by various small-scale management practices (Fig. 3.6). Although the higher spatial resolution of Landsat image provides more detail at the land surface, the lower temporal resolution (16-day) limits its application in remote sensing based GPP models. Sixteen days between observations are long periods of time for characterizing vegetation, especially grasslands and crops. In addition, some observations are affected by cloud covers. Thus, Landsat may not be suitable to track the recovery trajectory of vegetation. For example, Landsat images were not available during the intensive field research campaign, while MODIS images captured this event well (Fig. 3.7). Thus, combining observations from Landsat and other high spatial resolution sensors (e.g., SPOT HRB/HRVIS and Sentinel-2A/B) can help to alleviate this issue.

With a single flux tower site, we simulated GPP using VPM for both disturbed and undisturbed scenarios. This approach of combining remote sensing and EC data to study the impacts of management practices on GPP helps to extend the use of EC data collected within flux networks (e.g., AmeriFlux and FLUXNET) to study the impacts of

management practices (Campioli et al. 2015) in cases where paired-tower data are not available.

3.4.2. Complexity of assessing the impacts of management practices

There are a multitude of management practices that can occur in different durations and intensities. Most pastures in the Great Plains are used to support livestock grazing. The management practices evaluated in this study (burning, baling, and grazing) are quite common in the tallgrass pasture region (Fischer et al. 2012; Luo et al. 2009; Owensby et al. 2006; Suyker et al. 2003). The grassland greened up immediately after burning in April. Our results showed quick recovery (about one month) of grassland after baling. The pasture was a stronger carbon sink in September than in August mostly because of more precipitation in September. The net overall effect of baling on GPP was negligible because of the fact that baling enhanced the production in the post-baling period and resulted in higher GPP than the unbaled condition. The effect of baling may have been confounded by climatic conditions as well. For example, large rain events in late July and early September increased GPP, possibly offsetting the reduction in GPP caused by baling. Because of the large variability in climate from year to year, this may not be the case for baling in other years or locations. Beside climatic conditions, timing and intensity (e.g., stubble height) of baling could also play important roles in determining the response/recovery of ecosystem from the disturbances. To better understand the impacts of baling and other management activities, multiple years of data and consideration of interaction between management practices and climatic conditions (Fischer et al. 2012; Luo et al. 2012; Wagle et al. 2015) are needed. Grazing in the late growing season had similar impacts on VIs and

GPP in both iGOS W and iGOS WN, indicating similar grazing intensity over the entire field. To investigate the impacts of grazing, comparison between grazed and un-grazed fields is needed.

3.4.3. Importance of the examination of EC footprint

As GPP_{EC} was used to evaluate the performance of VPM, we assume that the EC system and MODIS observed the same area. To test this assumption, we overlapped the EC footprint with the affected area characterized by Landsat images during different periods (Fig. 3.13). Contribution of flux measurements outside the iGOS W MODIS pixel boundaries can be detected by flux tower, while it cannot be detected using VIs derived from MODIS. The peak contribution of flux measurement from the upwind distance increased from 50-60 m before the first baling (Fig. 3.13a) to 80-90 m after the first baling (Fig. 3.13b and c). This discrepancy may be a function of decreased roughness due to reduced canopy height after baling (Chen et al. 2011a; Chen et al. 2012; Schmid 1994). Since the flux tower is 100 m away from the southern boundary of the iGOS W pixel, the second baling in the southeastern part of the field had little effect on the flux measurement (Fig. 3.13c). This observation suggests that we need to bring the EC footprint dynamics (size, shape, and direction) into consideration because the affected areas in second baling might be in the fetch area and observed by the flux tower, while the iGOS W pixel cannot reflect this effect. If this scenario is the case then the pixel-to-pixel comparison in GPP model evaluation using EC measurements might be biased. Thus, investigating the dynamics of the footprint and its relative location to managed area is important to reflect the true impacts of management practices.

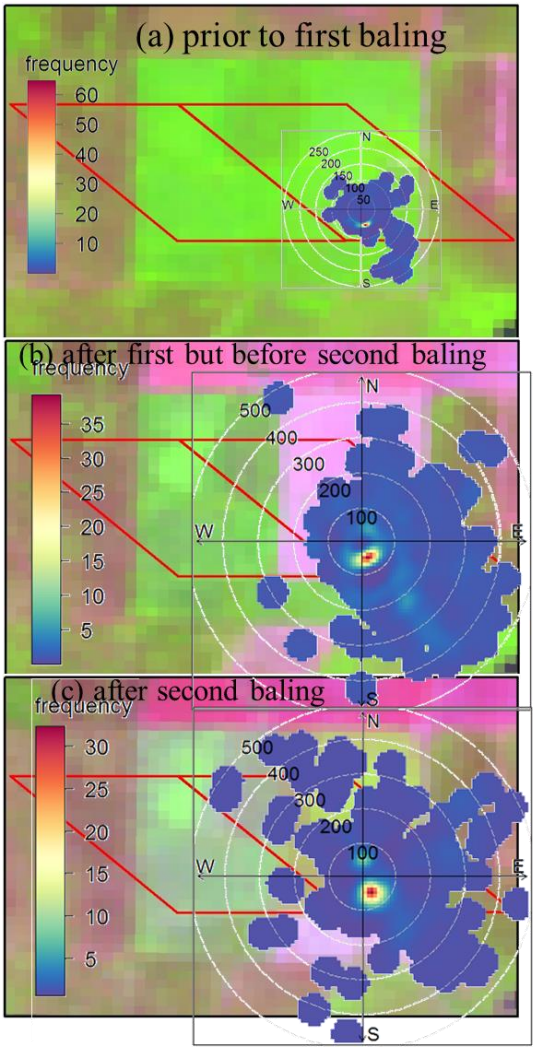


Figure 3.13. Footprint before and after hay baling. (a) Prior to first baling, (b) after first but before second baling, (c) after second baling. The background images are from Landsat which showed conditions prior to baling, after the first baling, and after the second baling. The circular dots are contribution of flux measurements from different direction and distance. Colors indicate the frequency of contribution of flux measurements.

3.4.4. Implication and future steps

This comprehensive case study used different data sources to investigate the impacts of different management practices on grassland phenology and carbon dynamics. We quantified the impacts of disturbance from an intensive field research campaign and baling on GPP using a single flux tower data, satellite remote sensing

data, and modeling. This approach could be used in other similar conditions for better utilization of carbon fluxes data to quantify the impacts of management practices. The study only includes one year of data. Thus, to better understand the interactive effects of management practices and climatic conditions, additional study years and sites are needed. There is a potential to use data from different networks (e.g., EC data from FLUXNET and PhenoCam images from PhenoCam Network) (Baldocchi et al. 2001; Richardson et al. 2009) to better understand impacts of various land management practices on plant phenology and carbon fluxes in different years.

The difference between GPP_{VPM_W} and GPP_{VPM_WN} was highly dependent on the differences in VIs for the two neighbor MODIS pixels. However, MODIS obscured this difference because of its spatial resolution. We showed large differences in the VIs derived from MODIS and Landsat images (Fig. 3.8), which needs further research. The low temporal resolution of Landsat also limited the ability to detect GPP dynamics over short periods of time.

Although we proposed a way to simulate the impacts of management practices and disturbances on GPP in a complex agricultural production field, additional research is needed to better estimate the individual and confounding effects of different management practices. Ensuring the fetch area of the flux tower can reduce the effects of changed footprint on GPP model and management evaluation (Chen et al. 2011a; Chen et al. 2012). Locating the flux tower in the center of the MODIS pixel can facilitate the linkage between EC and satellite observations (Zhang et al. 2014a). Each management regime needs better understanding before we blend different management practices. The compounding effects of interactive management practices need further

examination with multiyear data. For example, burning in the early growing season might increase nutrient availability and affect the response of the field to baling.

3.5 Conclusion

This case study used digital repeat photography (PhenoCam), satellite remote sensing, and the eddy covariance technique to investigate the impacts of burning, baling, and grazing on plant phenology and carbon fluxes in an Old World bluestems pasture. Multiple datasets allowed studying intra-annual variations caused by various management practices. PhenoCam images provided valuable information for both management practices and plant phenology. MODIS and Landsat images reflected different aspects of management practices. Higher temporal resolution of MODIS helped in understanding the GPP dynamics, whereas Landsat detected the burning and baling affected area because of its higher spatial resolution. VIs from MODIS showed impacts of burning and baling on plant phenology. Responses of GPP in baled and unbaled grasslands to large rain events were different because of different stages of vegetation. The larger increase of GPP after large rain in baled grassland (photosynthetically more active vegetation) compensated the reduction in GPP caused by baling. This result indicated that the interaction of management practices with climate is important when studying their impacts on GPP. Since management practices are often complex (e.g, grazing and baling in pasture), we need multiyear data from different sources for better understanding of individual and confounding impacts of those management practices. Investigation of the dynamics of EC footprint and its relative geolocation to affected area is important when evaluating the impacts of management practices. The approach of integrating EC data with remote sensing to

study the impacts of management practices on plant phenology and carbon fluxes can be helpful to extend the usage of EC data collected within the flux networks (e.g., AmeriFlux and FLUXNET) to study the impacts of different management practices.

Chapter 4: Quantifying agricultural drought in tallgrass prairie region in the U.S. Southern Great Plains through analysis of a water-related vegetation index from MODIS images

Abstract

Severe droughts in the Southern Great Plains (SGP: Kansas, Oklahoma, and Texas) in recent years have reduced the productivity of tallgrass prairie and resulted in substantial economic losses to the beef cattle industry in this region. Understanding spatial and temporal patterns of agricultural drought in the SGP can help ranchers to develop and implement drought mitigation strategies. In this study, the Land Surface Water Index (LSWI), calculated from the Moderate Resolution Imaging Spectroradiometer (MODIS) near infrared and shortwave infrared bands, was used to assess agricultural drought in the tallgrass prairie region of the SGP during 2000-2013. The number of consecutive days with LSWI < 0 (DNLSWI) during the growing season was defined as the drought duration, which, was then used to identify and analyze frequency of summer drought and whole growing season drought (WGSD). The spatial pattern of DNLSWI was consistent with the east-to-west decreasing precipitation gradient across the SGP region. Summer drought duration as depicted by the DNLSWI in the western portion of the study area was around one and a half month. The occurrence of WGSD increased from one year in the east to up to six years in the west, demonstrating the susceptibility of the tallgrass prairie region to drought. In addition to the total amount of precipitation, its intra-annual distribution also played an important role in drought development. A comparison with other widely used national drought products, namely the Evaporative Stress Index (ESI), the Vegetation Drought Response

Index (VegDRI), and the United States Drought Monitor (USDM), shows that LSWI-based drought has good agreement with ESI and USDM. Quantitative analyses indicate that LSWI-based drought agreed better with ESI in severe drought conditions than in moderate or pre-drought conditions. Severe drought periods characterized by the USDM also had low LSWI values. The areas affected by drought derived from the LSWI-based drought index were significantly correlated with hay production. As an indicator of vegetation water stress at moderate spatial resolution (~500 m), the LSWI has the potential to show drought conditions for an individual ranch and offer guidance for drought mitigation activities and livestock production.

4.1 Introduction

Drought is a complex natural hazard caused by a deficit in precipitation over different time periods (McKee et al. 1993). It is one of the most costly natural disasters and imposes wide-ranging impacts on the economy, environment, and society (Hayes et al. 2012; Mishra and Singh 2010). Tallgrass prairie, an important native grassland type in the Southern Great Plains (SGP: Kansas, Oklahoma, and Texas) of the United States (U.S.), is susceptible to frequent droughts (Basara et al. 2013; Christian et al. 2015; Gu et al. 2007; Gu et al. 2008; Hoerling et al. 2014; Schubert et al. 2004). Poor vegetation growth during agricultural drought reduces crop and forage production which, in turn, threatens the survival of animals and the viability of the livestock business in the SGP (Garbrecht 2015). The agricultural drought of 2011 in Texas caused more than $7.62 billion in losses, with about half of the loss attributed to reduction in livestock production (AgriLifeToday 2011; Fannin 2012; Ziolkowska 2016). Thus, it is crucial to provide information about drought characteristics (e.g., spatial distribution of different

drought durations in each year) and regional drought assessment (e.g., drought severity and regional susceptibility to drought) for agricultural end users and policy-makers in the SGP to facilitate drought mitigation and adaptation decisions (Otkin et al. 2015).

Drought can be characterized from different perspectives reflecting the reduction of precipitation and/or its impacts on other factors, including runoff, streamflow, soil moisture, evapotranspiration (ET), and vegetation water stress (Fig. 4.1). Meteorological drought mainly focuses on deficits in precipitation. Hydrological drought depicts inadequate streamflow and/or surface and ground water levels. Agricultural drought occurs when vegetation experiences stress due to inadequate soil moisture availability, reflecting a more ecosystem point of view on the impacts of drought. As agricultural drought develops, the plant canopy experiences a loss of vegetation water content and pigments such as chlorophyll, and eventually a loss of green leaves.

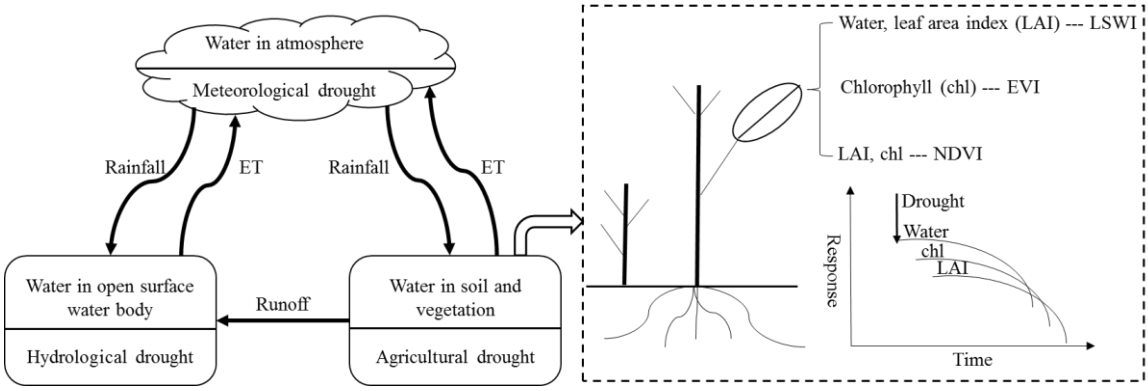


Figure 4.1. Different timescales of drought, highlighting observables of vegetation water stress expressed as remote sensing proxies. Only the primary factors affecting the remotely sensed vegetation indices are listed.

Many drought indices, based on anomalies or percentiles in relevant hydrologic variables (e.g., precipitation, soil moisture or ET), have been developed to monitor

various classes of drought (Hayes 2006; Zargar et al. 2011). Among these, two meteorological drought indices, namely the Palmer Drought Severity Index (PDSI) (Palmer 1965) and the Standardized Precipitation Index (SPI) (McKee et al. 1993, 1995), are currently most widely used. These early standard meteorological drought indices (e.g., PDSI and SPI) tend to focus on precipitation deficiencies at coarse spatial resolution (i.e., the climate division level). They provide valuable information for policy makers to implement drought mitigation actions; however, these indices are usually based on sparsely located long-term meteorological stations. Hydrological drought indices often use basin-specific parameter values, making it difficult to compare among basins (Dai 2011; Mu et al. 2013). Agricultural drought indices have been developed to monitor soil water deficits and the subsequent crop failure in the drought. The Crop Moisture Index (CMI), which is related to PDSI, is able to track the agricultural drought by considering soil moisture deficit in the top 1.5 meters of soil column (Palmer 1968). The role of vegetation was not reflected in the early stages of the development of agriculture drought indices because of the complexity of different plant physiological processes and lack of data (Palmer 1965). Most agricultural drought indices use soil moisture to indicate drought and do not explicitly consider vegetation water stress (Narasimhan and Srinivasan 2005; Palmer 1965, 1968).

Satellite remote sensing is providing consistent observations of vegetation dynamics, which can be incorporated into drought monitoring over large areas at high spatial and temporal resolutions (AghaKouchak et al. 2015; Wardlow et al. 2012a). Remote sensing products such as vegetation greenness indices, vegetation water indices, and land surface temperature have been widely used to monitor and assess drought

conditions since the 1980s (Gao 1996; Hayes et al. 2012; Peters et al. 2002; Rouse Jr et al. 1974; Wan et al. 2004). At the late stage of a severe drought, plant leaves often wither and abscise, resulting in a change in leaf area index (LAI) that can be tracked by the Normalized Difference Vegetation Index (NDVI) (Fig. 4. 1) (Cheng et al. 2006). NDVI, calculated as a normalized ratio between red and near-infrared (NIR) bands (Tucker 1979), has been incorporated into different drought products such as the Vegetation Condition Index (VCI) (Kogan 1995), Vegetation Drought Response Index (VegDRI) (Brown et al. 2008), and Vegetation Temperature Condition Index (VTCI) (Wan et al. 2004). The Enhanced Vegetation Index (EVI) is another vegetation greenness index with improved sensitivity to soil background and atmospheric condition (Huete et al. 2002). At the middle stage of agricultural drought, plant photosynthetic capacity is harmed by reduction of leaf chlorophyll content, which can be approximated by EVI as a proxy (Lawlor 2002; Medrano et al. 2002). At the early stage of agriculture drought, vegetation water stress is often characterized by the decrease of leaf water content. Water-related vegetation indices such as the Normalized Difference Water Index (NDWI) (Gao 1996) and the Land Surface Water Index (LSWI) (Xiao et al. 2004a), calculated as a normalized ratio between NIR and shortwave infrared (SWIR) bands, are more sensitive to the leaf water content and water stress than are vegetation greenness indices such as NDVI and EVI (Gu et al. 2007; Gu et al. 2008; Jackson et al. 2004; Maki et al. 2004; Wagle et al. 2014). Consequently, recent studies have shown the ability of LSWI to track drought-impacted vegetation or to monitor drought (Bajgain et al. 2016; Bajgain et al. 2015; Chandrasekar et al. 2010; Wagle et al. 2015; Wagle et al. 2014).

Wagle et al. (2014) examined the seasonal dynamics of LSWI derived from the Moderate Resolution Imaging Spectroradiometer (MODIS) and the CO_2 flux data at two tallgrass prairie eddy flux tower sites during 2005-2006 in Oklahoma, and reported that LSWI < 0 during the growing season indicates drought-impacted vegetation. Another study (Bajgain et al. 2015) used LSWI to assess and track drought conditions at two tallgrass prairie sites in Oklahoma during 2000-2013 and showed that LSWI < 0 was corresponded well with moderate or severe drought categories indicated by the United States Drought Monitor (USDM) (Svoboda et al. 2002). Another follow up paper validated the LSWI-based drought algorithm for 113 Mesonet stations across Oklahoma and showed that LSWI is sensitive to rainfall variations and can be used as an indicator of drought occurrence (Bajgain et al. 2016). Based on these previous site-level findings (Bajgain et al. 2016; Bajgain et al. 2015; Wagle et al. 2014), we hypothesize that the LSWI-based drought algorithm can be applied to assess the drought dynamics of tallgrass prairie at the regional scale such as in the SGP.

The specific objectives of this study are (1) to apply the LSWI-based drought algorithm in the tallgrass prairie of the SGP during 2000-2013; (2) to analyze the impacts of precipitation distribution on different drought patterns; and (3) to compare the LSWI-based drought map with other U.S. national drought products such as the Evaporative Stress Index (ESI) (Anderson et al. 2011; Anderson et al. 2007; Otkin et al. 2013), VegDRI (Brown et al. 2008), and USDM (Svoboda et al. 2002), during normal, summer drought, and growing season drought years.

4.2 Materials and methods

4.2.1 Study area

This study focuses on the SGP region in the U.S., specifically including Kansas (KS), Oklahoma (OK), and Texas (TX) (Fig. 4.2). These three states are known for extensive ranching and farming. The mean annual precipitation (MAP) shows a decreasing gradient from east (1400 mm) to west (200-400 mm) across the region (http://www.prism.oregonstate.edu/normals/). Precipitation is highly variable both inter- and intra-annually (Christian et al. 2015; Flanagan et al. 2017; Weaver et al. 2016). Maximum temperatures in summer are usually associated with low atmospheric humidity and strong winds, which in turn produce high rates of soil moisture depletion

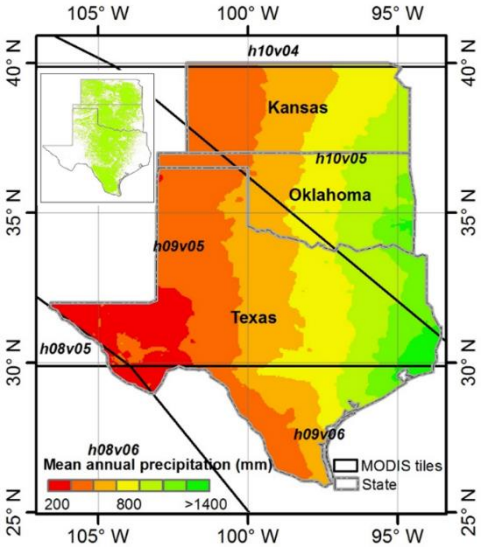


Figure 4.2. Location of the Southern Great Plains (SGP) study area and the coverage of the tallgrass prairie (in the inset). MODIS tile boundaries are indicated as dark lines. The base map shows the 30 year (1981-2010) mean annual precipitation over the region.

through ET, the main reason for summer drought (Dong et al. 2011). Soil types are mainly sandy and clay with small surface slopes (Carter 1994). Shortgrass prairies are

distributed in the arid and semiarid western part of the SGP, while tallgrasses prairies are primarily located in the sub-humid eastern part of the region (Carter 1994).

4.2.2 Data

4.2.2.1 MODIS-based LSWI and NDVI

The SGP is covered by six MODIS tiles (Fig. 4.2). The 8-day composite MODIS Surface Reflectance product at a 500-m spatial resolution (MOD09A1) (Vermote and Vermeulen 1999) was used to calculate LSWI and NDVI at 500 m. MOD09A1 includes seven-bands: blue (459-479 nm), green (545-565 nm), red (620-670 nm), two near infrared (NIR_1: 841-876 nm; NIR_2: 1230-1250 nm), and two shortwave infrared ($SWIR_1$: 1628-1652 nm, $SWIR_2$: 2105-2155 nm) bands at a 500-m spatial resolution. MOD09A1 also includes quality control flags for consideration of various image artifacts (e.g., clouds and cloud shadow). For each 8-day composite image, LSWI (Xiao et al. 2002b, c) and NDVI (Tucker 1979) were calculated using surface reflectance (ρ) from MODIS red, near infrared (NIR_1) and shortwave infrared bands ($SWIR_1$) as:

$$LSWI = \frac{\rho_{nir} - \rho_{swir}}{\rho_{nir} + \rho_{swir}} \quad (1)$$

$$NDVI = \frac{\rho_{nir} - \rho_{red}}{\rho_{nir} + \rho_{red}} \quad (2)$$

4.2.2.2 MODIS Land Surface Temperature (LST) data

The MODIS 8-day Land Surface Temperature (LST) product (MOD11A2) at a 1-km spatial resolution from 2000 to 2013 was used to depict the nighttime LST (LST_{night}) (Wan and Dozier 1996) and define the thermal growing season. Detailed

descriptions of MOD11A2 can be found at https://lpdaac.usgs.gov/dataset_discovery/modis/modis_products_table/mod11a2. The LST data were resampled from 1-km to 500-m spatial resolution using nearest neighbor interpolation.

4.2.2.3 MODIS Land Cover Type data

The MODIS Land Cover Type product (MCD12Q1) was used to generate the grassland mask (Friedl et al. 2002) and then to define the tallgrass prairie layer. The IGBP (International Geosphere-Biosphere Program) classification scheme was used, which includes a grassland class (https://lpdaac.usgs.gov/dataset_discovery/modis/modis_products_table/mcd12q1).

4.2.2.4 Precipitation data

Precipitation data were downloaded from PRISM Climate Group, Oregon State University (http://prism.oregonstate.edu). The time series of precipitation datasets are modeled using climatologically-aided interpolation, which uses the long-term average pattern (i.e., the 30-year normals) as first-guess of the spatial pattern of climatic conditions for a given month or day. Monthly precipitation data for 2000-2013 were used to generate summer precipitation (June-August, JJA) and annual precipitation.

Precipitation data measured by automated weather stations covering Oklahoma were also included to evaluate the LSWI-based drought at site level. The dataset was acquired from a previous LSWI-based drought related study in Oklahoma (Bajgain et al. 2016). The precipitation anomalies were compared against LSWI anomalies at 113 Mesonet stations across Oklahoma for the drought years.

4.2.2.5 Forage production data

Forage production, especially for hay, is affected by drought as most of the hay producing fields rely on rainfall. Hay production data from the United States Department of Agriculture - National Agricultural Statistics Service (https://www.nass.usda.gov/Quick_Stats/) were used to evaluate the LSWI-based drought depictions in each state included in the study. A simple linear regression model was used to examine the relationships between drought affected area and hay production for each state.

4.2.3 Algorithms for mapping agricultural drought

Based on findings from our previous studies (Bajgain et al. 2016; Bajgain et al. 2015; Wagle et al. 2014) that the LSWI can assess the impact of drought on tallgrass prairie vegetation at individual sites, this study aims to expand its use to identify both summer drought and whole growing season drought (WGSD) conditions at the regional scale (SGP). Fig. 4.3 illustrates the steps in the drought identification algorithm as applied to MODIS time series data for a given year. Nighttime LST data from the entire year were first used to determine the temperature-defined growing season, which is the time between the start and end dates for consecutive three 8-day periods with nighttime LST > 5^{o}C (Morison and Morecroft 2008; Zhang et al. 2015; Zhou et al. 2016). Second, the drop of LSWI below zero during summer (JJA) was used to indicate severe agricultural drought in summer (Bajgain et al. 2015). Third, the summer drought duration maps were generated by counting the number of days with LSWI < 0 (these days do not need to be consecutive) in JJA (DNLSWI). Years with all LSWI values less

than zero during the LST-defined plant growing season were defined as WGSD years (Fig. 4.3).

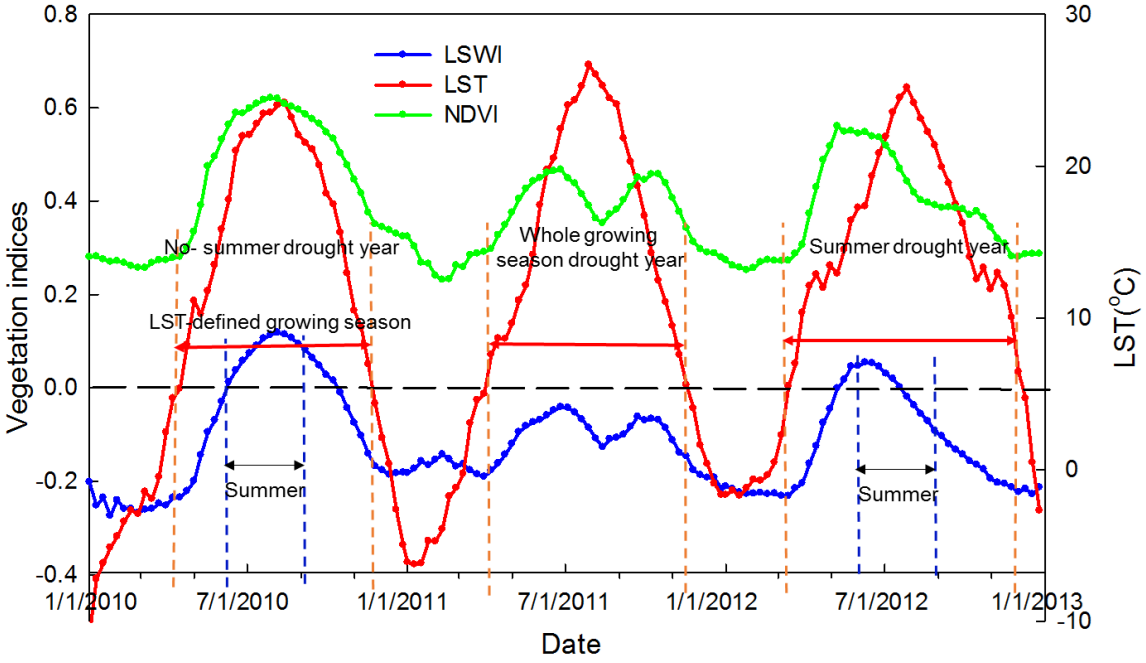


Figure 4.3. A schematic diagraph of the seasonal dynamics of LST, LSWI, and NDVI during drought and non-drought years for a sample data point is located at 36.556481ºN, -98.317713ºW. The LST-defined growing season is depicted for the duration of nighttime LST > 5 °C.

As the LSWI-based drought algorithm was originally developed for the tallgrass prairie, we focused on tallgrass prairie area in this study. The tallgrass prairie map was generated as the study area mask based on the MODIS land cover maps (MCD12Q1) for 2001-2013 and LSWI data. The grassland layer from MCD12Q1 for 2001 was used as a close approximation of 2000 since the MCD12Q1 dataset starts from 2001. Using these time series, the number of years that each pixel classified as grassland was computed, as well as the annual maximum value of LSWI ($LSWI_{max}$) during the LST-based growing season. To exclude sparse vegetation areas, the tallgrass mask was generated by selecting those pixels that meet two criteria over 14 years: (1) the number

of years as grassland is 7 or more (50% or higher) and (2) the number of years with $LSWI_{max} > 0$ is 7 or more (50% or higher) (Fig. 4.2 inset). This tallgrass prairie mask was then used to conduct the analyses of drought duration described later in the manuscript (Fig. S4.1).

Fig. S4.1. Data processing workflow for LSWI-based drought assessment algorithm.

4.2.4 Agricultural drought dynamics and comparison with other drought products

Annual agricultural drought maps were created to show the evolution of agricultural drought over the study period. Each drought map includes both summer and WGSD conditions. The drought maps for three consecutive years (2010, 2011, and 2012) were selected to represent three different drought conditions (normal, WGSD, and summer drought). WGSD and summer drought years were identified from annual and summer precipitation anomalies (Fig. S4.2), respectively, based on the fourteen-year mean (2000-2013). A mean summer drought duration map was generated showing the average drought duration for 2000-2013. The occurrence of WGSD map shows the frequency of WGSD during the study area from 2000 to 2013. These two summary maps indicate the spatial pattern of agricultural drought in the tallgrass region in the SGP.

Fig. S4.2. Annual, early spring, and summer precipitation deviation from the mean.

Three U.S. national drought products, namely ESI, VegDRI, and USDM, were also compared with the LSWI-based drought product to characterize different drought conditions. The ESI (Anderson et al. 2013; Anderson et al. 2011; Anderson et al. 2007) quantifies temporal anomalies in the ratio of actual to potential ET using thermal infrared remote sensing observations and the Atmosphere-Land Exchange Inverse

(ALEXI) surface energy balance model. It has been used to estimate the moisture stress of plants, as well as associated yield impacts (Anderson et al. 2016a; Anderson et al. 2015; Anderson et al. 2016b). VegDRI is a new 'hybrid' index that integrates satellite-based observations of vegetation conditions, climate-based drought index data, and biophysical characteristics of the environment, including PDSI, SPI, and NDVI, to depict drought-related vegetation stress (Brown et al. 2008; Tadesse et al. 2015; Wardlow et al. 2012b). The USDM is a composite drought index which incorporates climatic, hydrologic, and soil data along with professional inputs in order to provide weekly maps of drought conditions (Svoboda et al. 2002).

A direct comparison between the LSWI-based drought with ESI, VegDRI, and USDM is difficult due to their differences in temporal scales and spatial resolutions. ESI data are provided at weekly time steps composited over a period of 1-3 months. The VegDRI and USDM are also created weekly. In this study, we used 3-month ESI composites ending on the last week of August to compare with LSWI-based drought duration. The VegDRI and USDM for the last week of August were used in the comparison. The comparison was done for the period 2010-2012, which represent three different drought conditions (normal, WGSD, and summer drought).

4.2.5 The relationship between precipitation and LSWI-based drought duration

Because agricultural drought is triggered in part by a precipitation deficit, it is worthwhile to investigate the relationship between precipitation and LSWI-based drought duration. Summer drought duration from LSWI-based drought maps and cumulative summer rainfall (JJA) from PRISM data for 2010-2012 were extracted and analyzed. The relationships between summer drought duration and summer rainfall

were analyzed and the pattern of cumulative summer rainfall in different drought condition years are also presented. The site-level precipitation data from the Oklahoma Mesonet were also used to evaluate the LSWI-based drought. The spatial patterns of WGSD and annual precipitation deviation from the mean in 2011 (WGSD year) demonstrate the effects of annual precipitation on the WGSD. The relationship between WGSD affected area and the annual precipitation anomaly was also investigated.

4.3. Results

4.3.1 LSWI-based drought maps and comparison with ESI, VegDRI, and USDM

The tallgrass prairie in the SGP was affected by frequent droughts during the study period (Fig. S4.3) and the drought duration was consistent with the decreasing precipitation gradient from east to west in most years (Fig. 4.2). Some areas experienced a short duration of summer drought even in a normal rainfall year (e.g., 2010, Fig. 4.4a). Central SGP experienced a long period of summer drought in 2012 (indicated by dark red color) (Fig. 4.4i). 2011 was the most severe WGSD year in OK and TX (indicated by black color), with more than half of the tallgrass prairie areas affected (Fig. 4.4e). For KS, 2002 was the most severe WGSD year (Fig. S4.3c).

Fig. S4.3. Drought dynamics in the SGP for 2000-2013.

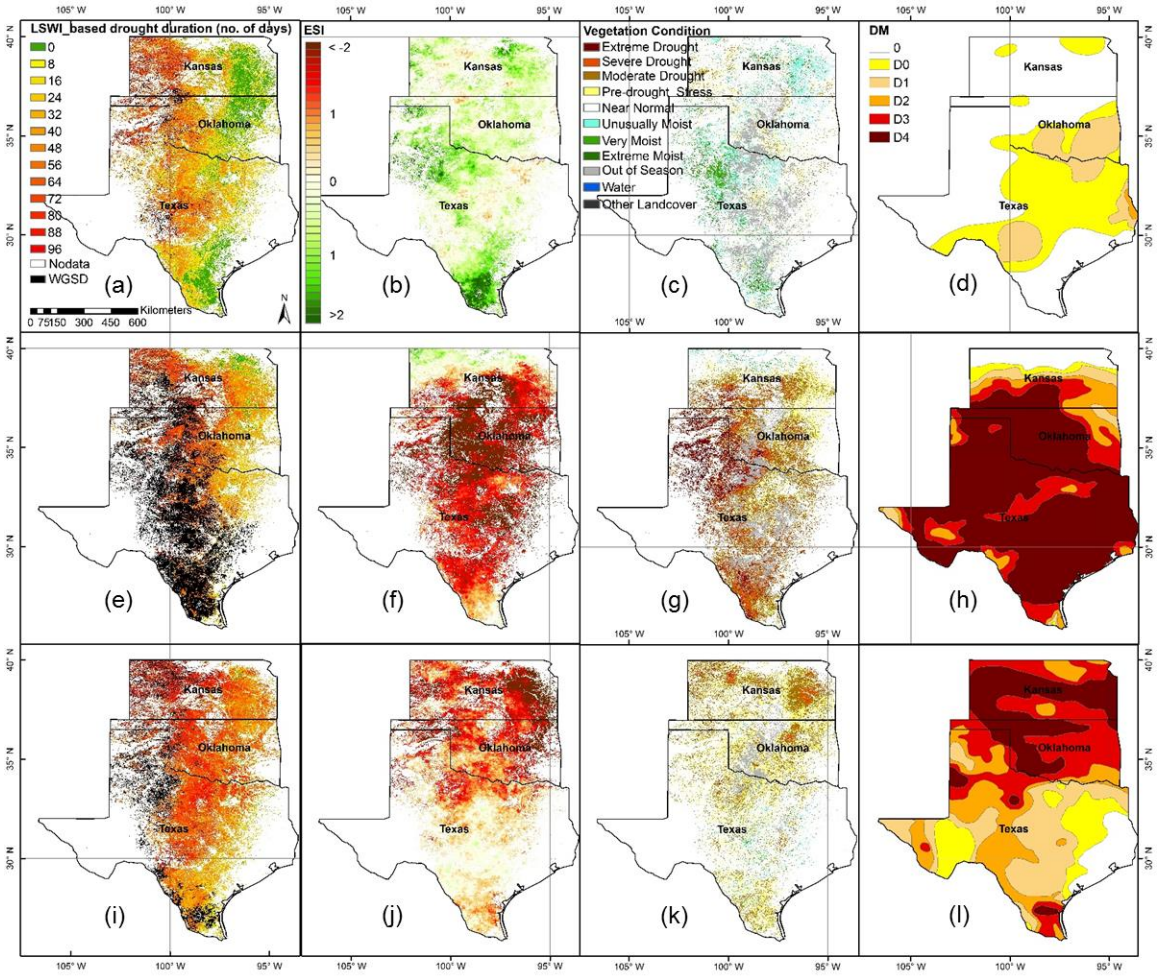


Figure 4.4. Comparison of LSWI-based drought duration with ESI, VegDRI, and USDM in normal, WGSD, and summer drought years. (a) Summer drought duration and WGSD in 2010, (b) Summer ESI in 2010, (c) Summer VegDRI in 2010, (d) USDM 20100831, (e) Summer drought duration and WGSD in 2011, (f) Summer ESI in 2011, (g) Summer VegDRI in 2011, (h) USDM 20110830, (i) Summer drought duration and WGSD in 2012, (j) Summer ESI in 2012, (k) Summer VegDRI in 2012, (l) USDM 20120828.

Fig. 4.4 shows ESI, VegDRI, and USDM summer drought depictions for 2010-2012, and compares with spatial patterns in the LSWI-based drought duration. The LSWI-based drought map, ESI, and VegDRI provided more detailed drought information than did USDM because of their higher spatial resolution and number of drought categories. The LSWI-based drought map showed a short period of drought

occurrence in the western SGP even in a normal year (2010) (Fig. 4.4a), while summer ESI indicated wet or near normal conditions for most of the areas (Fig. 4.4b) and VegDRI showed scattered pre-drought and unusually moist with big non-photosynthetically-active vegetation area (out of season category in the figure) (Fig. 4.4c). In 2011, all drought products identified extended/severe drought conditions in the central SGP (Fig. 4.4e-h). The four indices were different in their depictions of the 2012 drought conditions (Fig. 4.4i-l), with LSWI-based drought, ESI, and USDM showing extensive and severe drought for KS and OK, while VegDRI mostly indicating pre-drought to moderate drought. The increasing drought gradient from east to west in the LSWI-based drought map was not apparent in other drought indices except for VegDRI in 2011 (Fig. 4.4g).

In general, the patterns of LSWI-based summer drought maps are similar with those in the ESI and USDM for most of the areas (Fig. 4.4). However, the VegDRI tends to show less intense drought conditions than other drought products for the same year. One possible reason is that VegDRI uses long-term climate variables such as 36-week SPI which responds more slowly than LSWI and ESI. Similar findings were identified in a study by Otkin et al (Otkin et al. 2016).

LSWI, ESI, and VegDRI over the SGP tallgrass prairie regions were also compared quantitatively. Fig. 4.5 compares ESI values from the 3-month composite ending at the last week of August with LSWI-based drought duration for 2012, which is the period with severe summer drought. A clear trend of increasing ESI stress severity is identified with increasing length of drought conditions as identified by the LSWI. The dynamic range of ESI decreased along with the increasing summer drought duration

(Fig. 4.5), indicating that LSWI-based drought and ESI agree better for severe drought than moderate or pre-drought conditions. The relationship between LSWI and VegDRI showed a stronger trend than did the relationship between NDVI and VegDRI (Fig. S4.4).

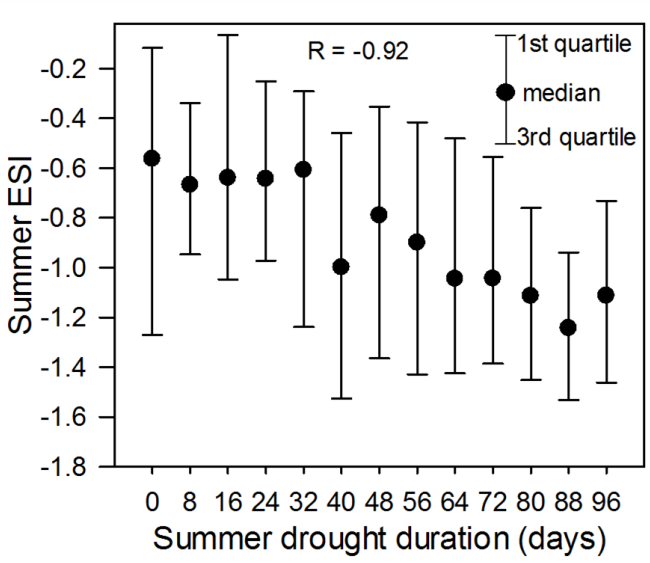


Figure 4.5. LSWI-based summer drought duration vs. 3-month composite ESI (JJA) in 2012.

Fig. S4.4. LSWI and NDVI vs. VegDRI for the last week of August in 2012. Only pixels classified as tallgrass prairie were plotted.

LSWI values are compared to the USDM drought severity classifications from the last week of August in 2012 in Fig. 4.6. Most areas depicted as experiencing severe drought according to the USDM (D3 and D4) also have very low LSWI values (Fig. 4.6b inset) such as western KS and southern TX (Fig. 4.6a). As two key indicators in the USDM are usually available only at the climate division scale, the USDM does not show much variability in drought severity within a climate division. In contrast, LSWI

shows large heterogeneity at the sub-climate division scale due to the relative high spatial resolution of the remotely sensed inputs.

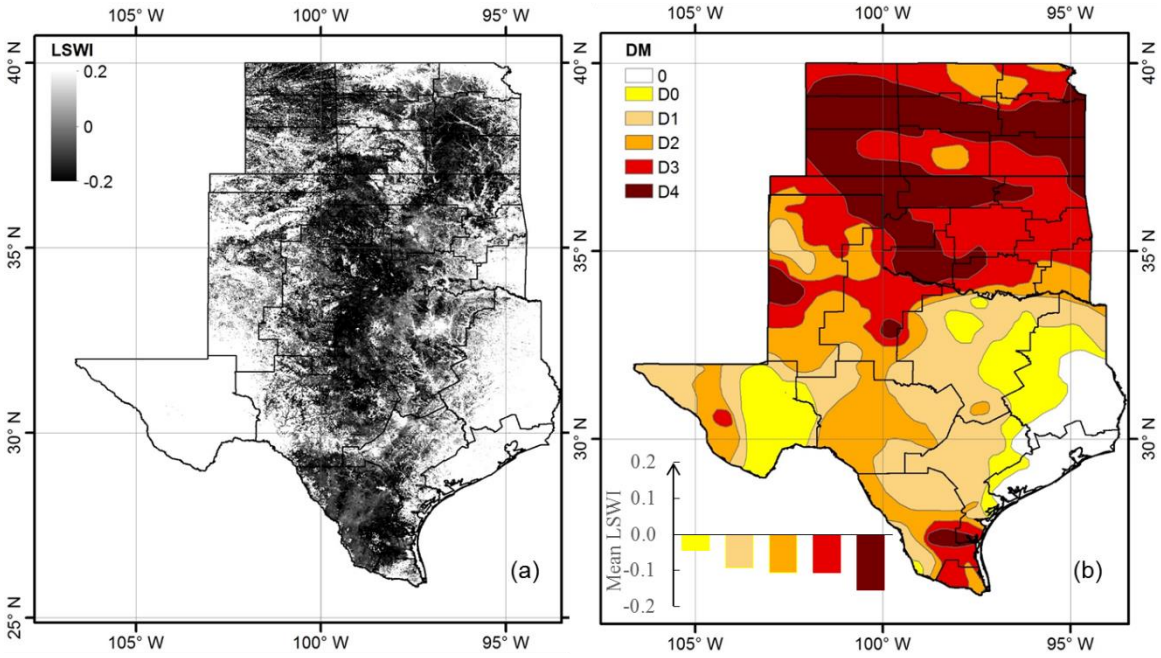


Figure 4.6. LSWI vs. USDM for the last week of August in 2012. The climate division boundaries are indicated by black polygons. Only pixels classified as tallgrass prairie were plotted. The inset in (b) showed the mean LSWI values in each category (D0, D1, D2, D3, and D4).

4.3.2 LSWI-based drought duration patterns in the SGP

Fig. 4.7 shows the dynamics of summer drought duration diagnosed by LSWI in three states (KS, OK, and TX) for 2000-2013. The summer drought pattern was highly variable among years in all three states. TX was affected by summer drought more often than KS and OK. 2012 was the most severe summer drought year in OK, with relatively small area affected by short periods of drought and large areas affected by longer periods of drought (Fig. 4.7b). The frequent occurrence of summer drought indicates the susceptibility of the SGP to agricultural drought. Fig. 4.8 shows the areas affected by WGSD across the region for 2000-2013. The pattern of WGSD in OK and TX were

similar with 2011 as the most severe WGSD year, while it was 2002 in the case of KS. In the most severe WGSD years, the area affected by WGSD was more than double of the mean value.

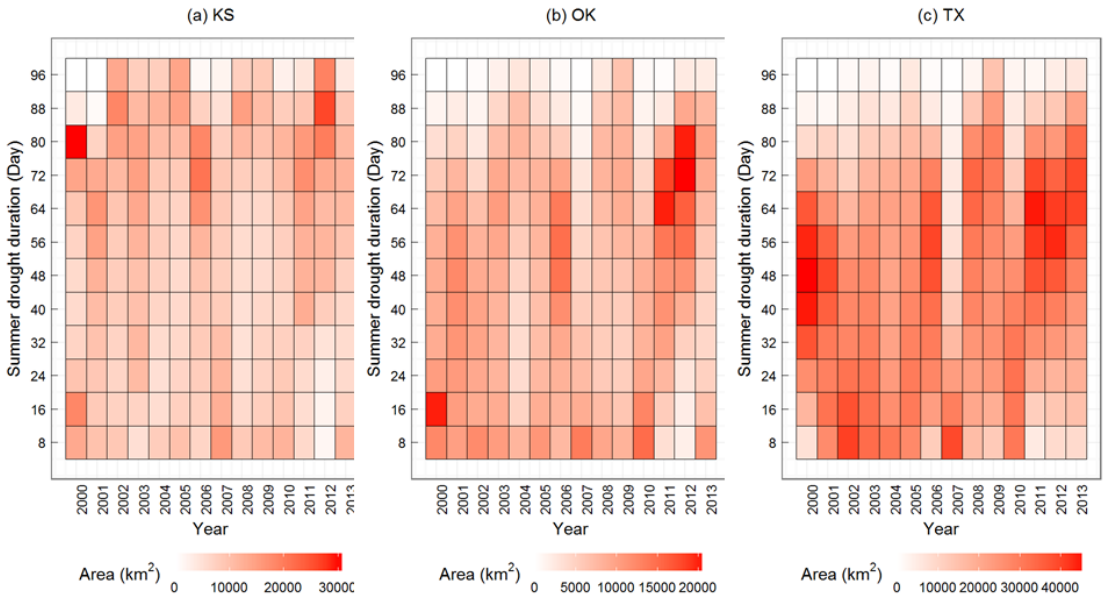


Figure 4.7. Annual summer drought dynamics in three states (KS, OK, and TX) of the SGP for 2000-2013.

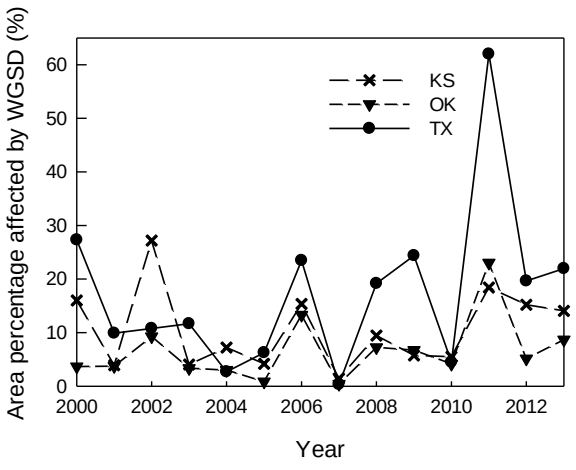


Figure 4.8. Areal percentage of the total tallgrass prairie area affected by the whole growing season drought (WGSD) in three states (KS, OK, and TX) of the SGP for 2000-2013.

Fig. 4.9 shows the mean of summer drought duration, standard deviation of summer drought duration, and frequency of the occurrence of WGSD for 2000-2013. As expected, both summer drought duration and occurrence of WGSD increased from east to west, along the gradient of decreasing precipitation. Mean summer drought duration can be as long as one and a half months (six 8-day periods) (Fig. 4.9a) and WGSD occurred in six years (Fig. 4.9c) in the west of the study area. The variability in summer drought duration was largest in the central part (Fig. 4.9b).

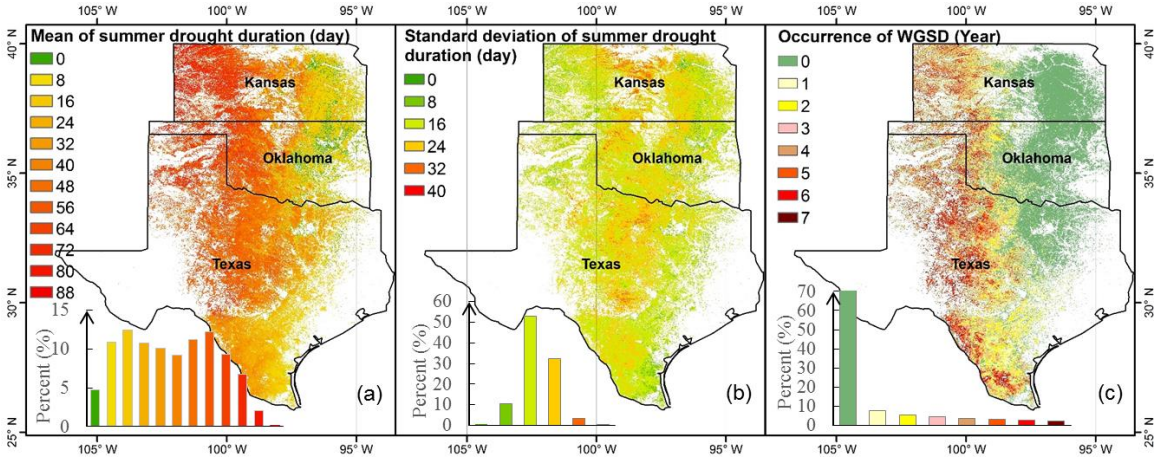


Figure 4.9. Summer drought and WGSD patterns in the SGP for 2000-2013. (a) Mean of summer drought duration for 2000-2013, (b) Standard deviation of summer drought duration, (c) Occurrence of WGSD for 2000-2013. The insert panel shows the frequency distribution of values.

4.3.3 Relationship between LSWI-based drought duration and precipitation

To quantify the contribution of precipitation deficits to drought development, we examined the relationship between precipitation and drought duration during the summer period and the entire year. The variation of the summer drought duration (indicated by error bar) was equally large for all precipitation ranges (Fig. 4.10), suggesting that summer precipitation is not the only factor determining summer drought duration. The cumulative summer precipitation (indicated by the relative frequency of

precipitation) in 2010 (Fig. 4.10a) was slightly higher than in 2012 (Fig. 4.10c), whereas the summer drought duration was quite different, with much longer summer drought duration in 2012. More than 60% percent of the pixels had less than 100 mm of cumulative summer precipitation in 2011 and long periods of summer drought. (Fig. 4.10b).

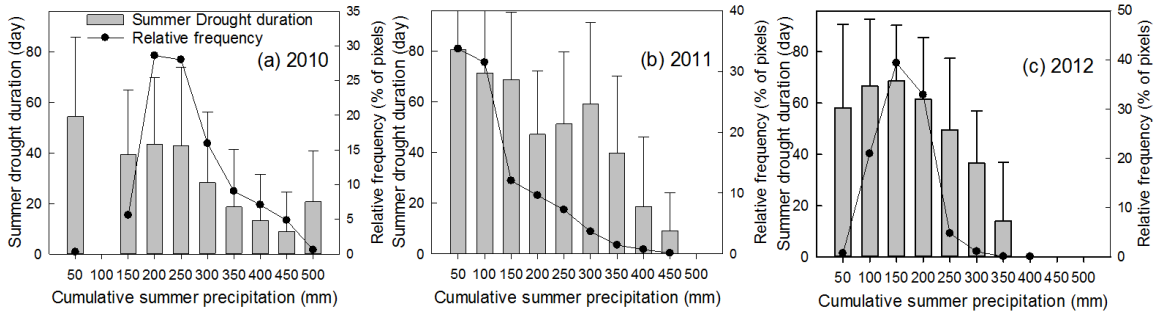


Figure 4.10. LSWI-based summer drought duration vs. summer precipitation in (a) 2010, (b) 2011, and (c) 2012. Relative frequency in the legend indicates the ratio of pixels with certain summer precipitation to the total pixels.

The LSWI anomalies were strongly correlated with summer precipitation anomalies (r^2 = 0.64) for the drought years (2006, 2011, and 2012) over 113 Mesonet stations across Oklahoma (Fig. 4.11). The increasing summer precipitation anomalies resulted in bigger magnitude of anomalies in LSWI at most Mesonet stations.

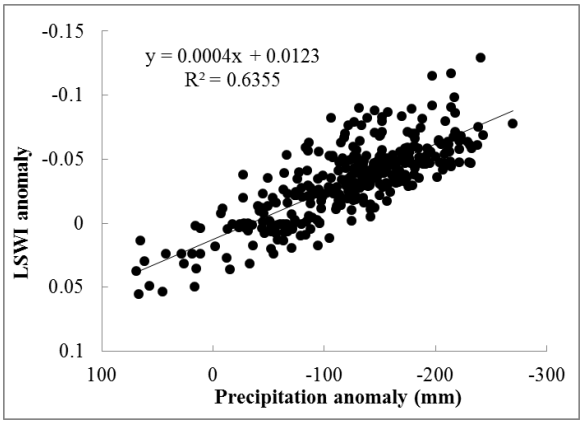


Figure 4.11. Comparison of summer precipitation anomalies and LSWI anomalies in drought years (2006, 2011, and 2012) at 113 Mesonet stations across OK.

Areas affected by WGSD increased from north to south in the SGP in 2011 (Fig. 4.12a). This trend correlates well with the annual precipitation deviation to the mean in 2011 (Fig. 4.12b). The mean value of the annual precipitation deficit in 2011 was 300 mm (Fig. 4.12b inset and Fig. S4.5) which is about one third of the long term mean annual precipitation (Fig. 4.2). Precipitation deviation from the mean (annual anomaly in 2011) in central and southern TX was as high as 400 mm or more. The increasing temperature gradient from north to south might also have exacerbated drought in the southern region.

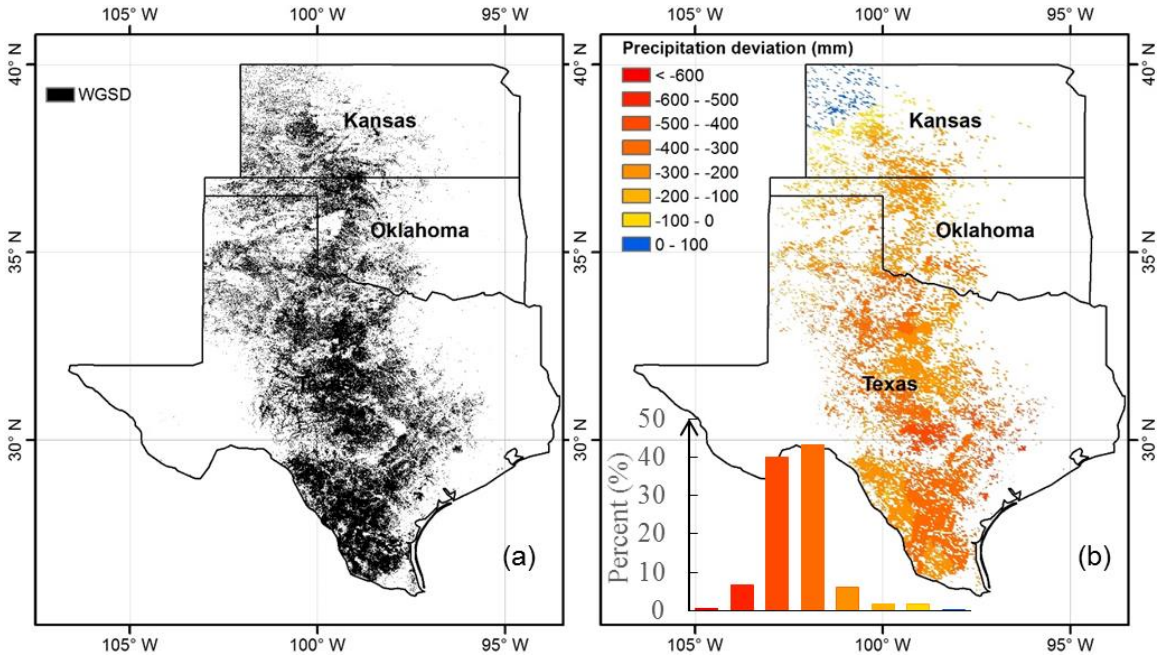


Figure 4.12. WGSD vs. annual precipitation in 2011. (a) Distribution of WGSD in 2011, (b) Annual precipitation deviation from the mean (annual anomaly in 2011). The inset in (b) shows the frequency distribution of precipitation deviation.

Fig. S4.5. Frequency distribution of the annual precipitation deviation from the mean in 2011.

To investigate the relationship between the WGSD affected area and annual precipitation anomalies, we plotted the ratio of WGSD affected areas to total state area

against annual precipitation anomalies for all three states during 2000-2013 (Fig. 4.13). Overall, larger anomalies in annual precipitation resulted in larger areas affected by WGSD. The point in the upper right corner is associated with large annual precipitation anomaly in 2011, demonstrating the severity of 2011 Texas drought.

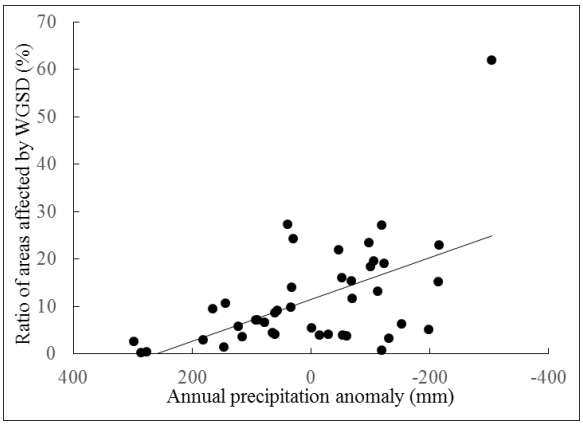


Figure 4.13. Relationship between the WGSD affected area and annual precipitation anomaly.

4.3.4 Validation of LSWI-based drought against forage production

Fig. 4.14 show the relationships between areas affected by drought (summer drought and WGSD) and hay production in each state during 2000-2013. The hay production showed a significant negative relationship with areas affected by drought. The lowest hay production year was 2011 in KS and TX and 2012 in OK. This is consistent with our results that 2011 and 2012 were the most severe drought years.

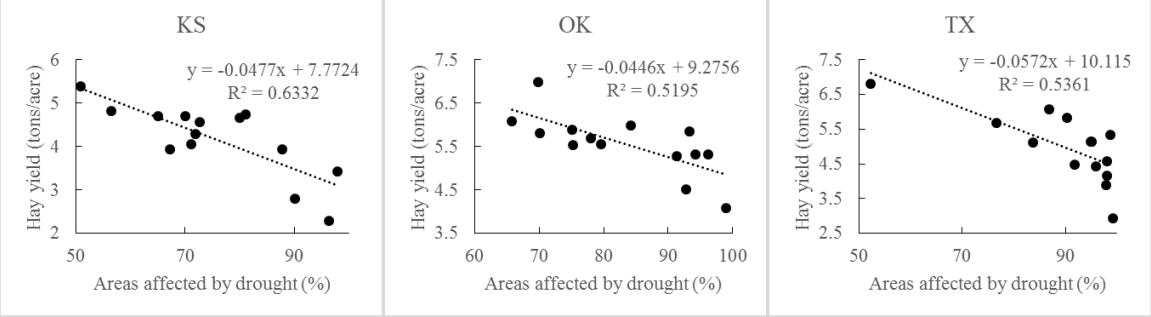


Figure 4.14. Relationship between areas affected by drought and hay production in each state.

4.4. Discussion

4.4.1 Comparison of the LSWI-based drought algorithm with other drought products

The LSWI-based drought algorithm uses LSWI values less than zero during the growing season to identify agricultural drought conditions based on the findings of previous studies at individual sites (Bajgain et al. 2015; Wagle et al. 2014). The SWIR band in LSWI is more sensitive to the canopy water content (high absorption by liquid water) than the red band used in NDVI (Gu et al. 2007; Gu et al. 2008; Jackson et al. 2004). Thus, the LSWI-based algorithm complements well with other NDVI-based drought products, as they together assess the impacts of drought on vegetation canopy from a loss of water to a loss of green leaves (Fig. 4.1). This study expanded the LSWI-based drought algorithm to include three conditions: no drought, summer drought, and WGSD, and then applied the algorithm at the regional scale (tallgrass prairie region in the SGP) to report agricultural drought conditions.

Similar spatial patterns of LSWI-based summer drought maps with ESI and USDM (Fig. 4.4), and strong relationships of low LSWI values with ESI (Fig. 4.5) and USDM categories (Fig. 4.6) during the severe drought indicate that LSWI can be used as a complementary drought index. The significant negative relationship between drought affected areas and hay yield further validated the reliability of the LSWI-based drought mapping. Using LSWI along with other commonly used vegetation indices such as NDVI and EVI can help improve the performance of current drought products. The LSWI-based drought algorithm completely depends on MODIS data and is easy to apply. It could be a complementary method for assessing agricultural drought in the tallgrass prairie at the regional scale with a spatial resolution of 500 m.

4.4.2 Importance of precipitation amount and distribution in the year

As expected, our results show that precipitation is a major factor for the occurrence of severe agricultural drought in tallgrass prairie since the regional agricultural drought pattern (Fig. 4.9a and c) was highly correlated with the decreasing precipitation gradient from east to west. Central SGP had long summer drought durations and large standard deviations (Fig. 4.9a and b) because of large summer precipitation variations (Fig. S4.6). The orthogonal nature of the temperature and precipitation gradients (east-west oriented precipitation gradient and north-south oriented temperature gradient) (Basara et al. 2013) could also generate this pattern in the central part of the SGP where the relative importance of temperature and precipitation varies in different years.

Fig. S4.6. Standard deviation of summer precipitation.

The total amount of precipitation in a year is important for vegetation. Large annual precipitation deficits in 2011 (Fig. 4.12) caused the occurrence of extensive WGSD in the SGP (Fig. 4.4e). The temporal distribution of precipitation is also equally important. The cumulative summer precipitation in 2012 was only a little bit lower than 2010 (Fig. 4.10), however, the drought condition in 2012 was much more severe (Fig. 4.4). The precipitation in early spring (March) was well distributed in 2012 (Fig. 4.15a). The ample precipitation in March 2012 (Fig. S4.2f and Fig. 4.15a) increased soil moisture and facilitated vegetation growth in spring (the anomaly of high NDVI is presented in Fig. S4.7). Summer rainfall was much less than the enhanced ET demand from abundant green vegetation, resulted in rapid depletion of soil moisture and severe summer drought in 2012. This result indicated that it was the joint control of

precipitation and vegetation that generated the severe summer drought in 2012. It suggests the important role of vegetation itself for the occurrence of agricultural drought in addition to total amount of precipitation. This phenomenon has been reported by other studies (Otkin et al. 2013; Otkin et al. 2014; Otkin et al. 2016) and referred as "flash drought" in which vegetation health rapidly deteriorates because the plants quickly exhaust soil moisture. Thus, LSWI-based drought does not only reflect precipitation anomalies to the historical mean as SPI does but is also sensitive to abnormal precipitation distribution in the year.

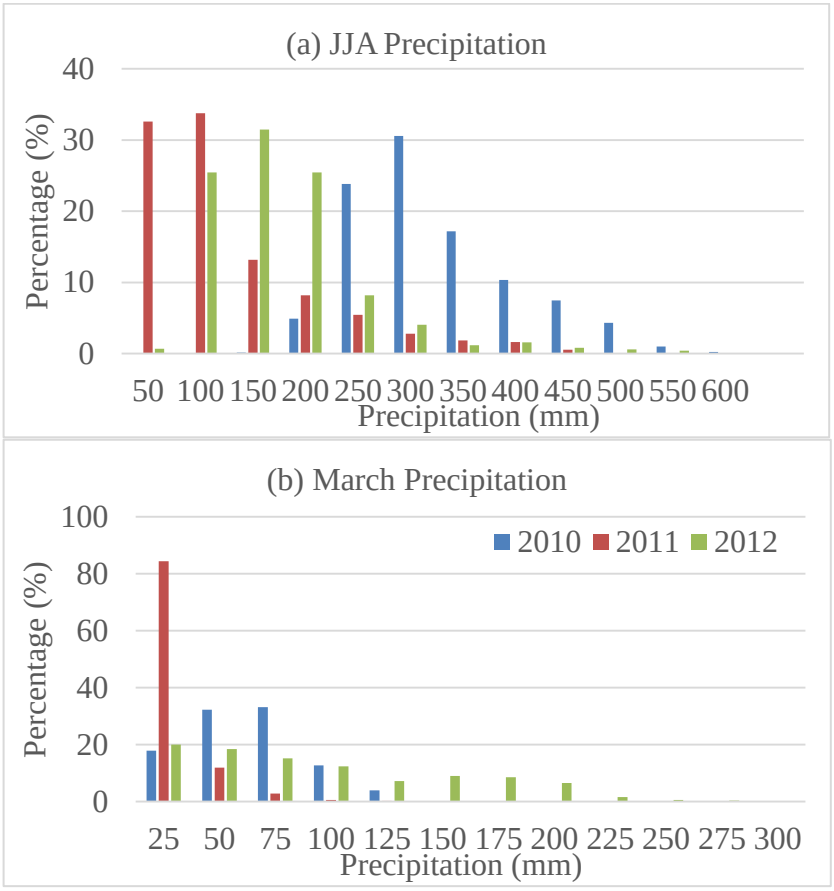


Figure 4.15. Precipitation distribution in early (March) and peak growing season (June-August) according to rainfall events (%) with different rainfall sizes (25 mm rainfall bin size in the graph).

Fig. S4.7. NDVI anomaly in early growing season of 2012 (March-May) relative to the baseline of 2000 - 2011. The inset shows the distribution of area percent of NDVI anomalies.

4.4.3 Future work and challenges

The LSWI-based drought algorithm, which only uses MODIS data as input, is easy to apply and has a higher spatial resolution (~500 m) than current operational versions of ESI, VegDRI, and USDM. Like most visible and thermal remote sensing algorithms, the LSWI-based drought algorithm has limitations during cloudy days when the land surface is not visible to the satellite sensor (Jensen 2009). Combinations of multiple satellite sensors and development of an appropriate gap-filling algorithm are needed to create a continuous dataset (Jin et al. 2013b), thereby reducing the effect of bad observations (e.g., cloud cover). Another concern is the threshold values used in the algorithm. We used LSWI < 0 during the growing season as the indicator of severe agricultural drought in tallgrass prairie based on the findings of site level studies (Bajgain et al. 2015; Wagle et al. 2014). The LSWI threshold for other land cover types and regions might be different, which needs to be further explored. The identification of agricultural drought in sparse vegetation area (e.g. arid region) using LSWI is challenging as soil background can contribute more to the satellite observations and reduce LSWI values. In these cases, the lower threshold of relative change of LSWI values might be better. Also LSWI is related to vegetation water content, it is not able to depict drought during the non-growing season. Additional studies are needed to develop a LSWI-based drought severity scheme based on plant phenology and anomalies. In this study, we evaluated and reported agricultural drought in terms of severe drought

duration in the summer and entire growing season, and drought severity at specific times was not included. Future studies need to compare the LSWI-based drought severity scheme at specific times (Bajgain et al. 2016; Bajgain et al. 2015) with ESI, USDM, and other drought products. Human and natural disturbances (grazing, mowing, and burning etc.) could also affect LSWI, which needs to be incorporated using land use and land management data.

The relationship between precipitation and drought needs to be further investigated as other studies indicated that high temperature can also contribute to the quick onset of drought in the SGP (Basara et al. 2013; Hoerling et al. 2014; Otkin et al. 2013; Otkin et al. 2016). The importance of vegetation in agricultural drought assessment needs to be emphasized in the future as precipitation does not always provide accurate drought assessment without considering the high ET demand by vegetation and available soil moisture in summer. Plant health can deteriorate rapidly during the summer through rapid loss of water because of their high ET. The ESI, an indicator of ET anomaly, is a good indicator to reflect the role of vegetation in agricultural drought development (Anderson et al. 2011; Anderson et al. 2007; Otkin et al. 2016). The importance of vegetation in drought development also emphasizes the necessity of investigating drought from the ecosystem perspective (AghaKouchak et al. 2015).

The duration of summer drought, summer drought variation, and number of years with WGSD present the pattern of agricultural drought in tallgrass prairie in the SGP (Fig. 4.9). The LSWI-based drought algorithm can be used to assess the vulnerability to agricultural drought, and it has the potential to use for several

applications such as vegetation production assessment, water demand/supply analysis, and bird migration and breeding (Brown and Brown 2014; Goddard et al. 2003; Wilhite 2005). The agricultural drought of tallgrass prairie in the SGP reduces hay production (Fig. 4.14), an important feed source for beef cattle production, especially in winter and early spring, which can threaten the beef cattle industry. A follow-up study will use the LSWI-based drought product to investigate the impacts of different drought types (e.g., summer drought and WGSD) and spatial patterns on hay and beef cattle production in the SGP.

4.5. Conclusion

Based on the findings of previous studies about the ability of LSWI to track drought-impacted vegetation in tallgrass prairie, this study expanded and applied a LSWI-based drought algorithm to map agricultural drought of tallgrass prairie in the SGP. The results are comparable to other widely used drought products (ESI, VegDRI, and USDM) in normal, WGSD, and summer drought years. The frequent occurrence of summer drought and WGSD indicates the susceptibility of the SGP to agricultural drought. The spatial pattern of drought duration was highly correlated with the decreasing precipitation gradient from east to west. TX was affected by summer drought more often than KS and OK. In the most severe WGSD years, the area affected by WGSD was more than double of the mean value. LSWI-based drought depictions are sensitive to both precipitation anomalies from the historical mean and abnormal seasonal precipitation distributions. The importance of vegetation in drought assessment needs to be emphasized in future drought studies. Incorporating LSWI other than NDVI into other drought products can help improve their performance. The LSWI-based

drought algorithm, completely depending on MODIS data and with a spatial resolution of 500 m, can be a complement for other drought products for assessment of agricultural drought in the tallgrass prairie region. Future studies need to explore LSWI thresholds to identify agricultural drought and develop LSWI-based drought severity schemes for other land cover types.

Supplementary materials

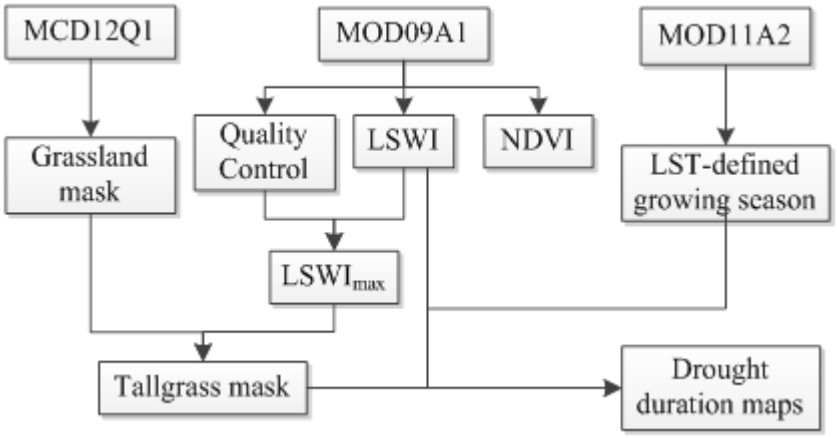


Figure S4.1 Data processing workflow for LSWI-based drought assessment algorithm.

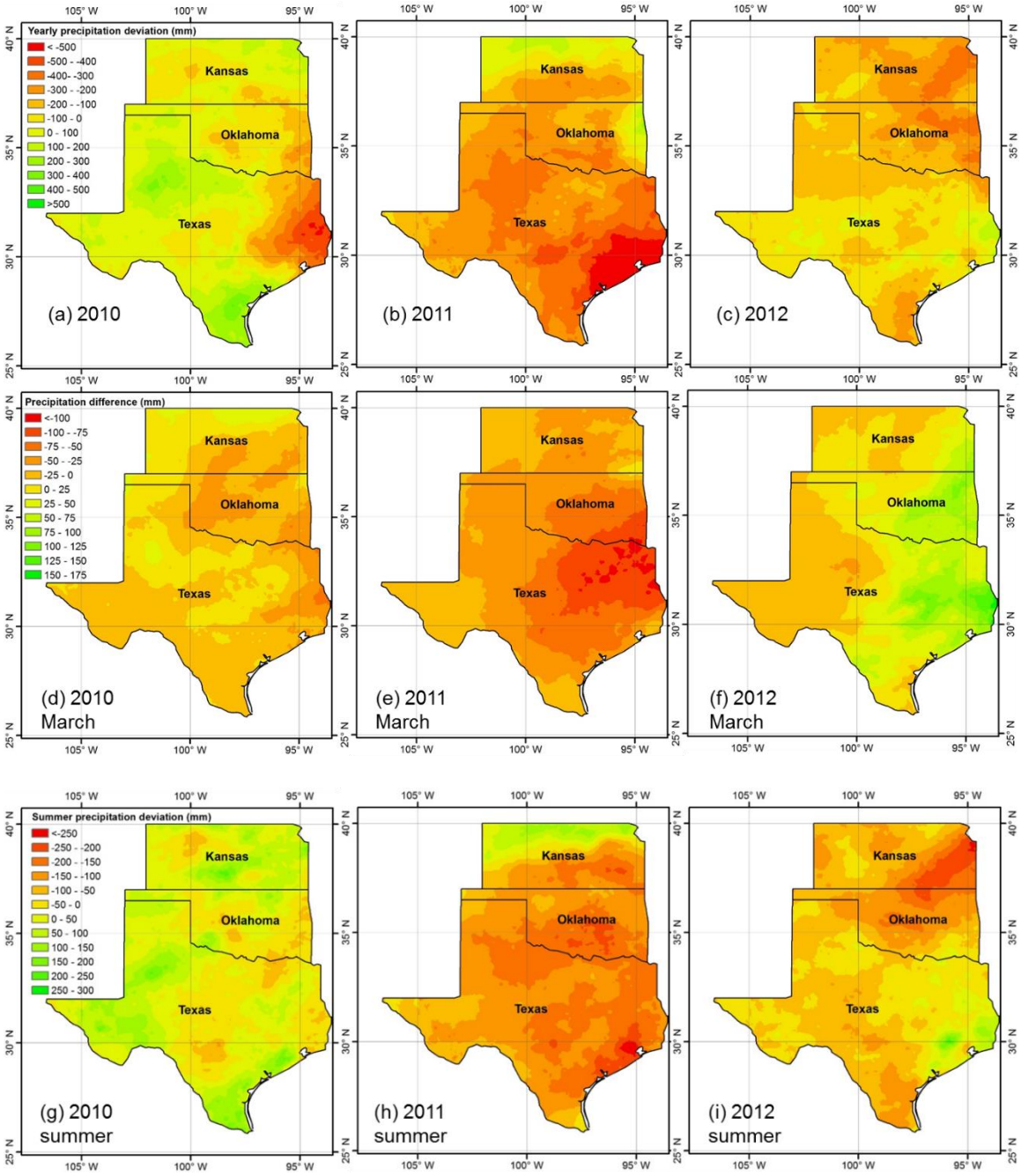


Figure S4.2 Annual, early spring, and summer precipitation deviation to the mean.

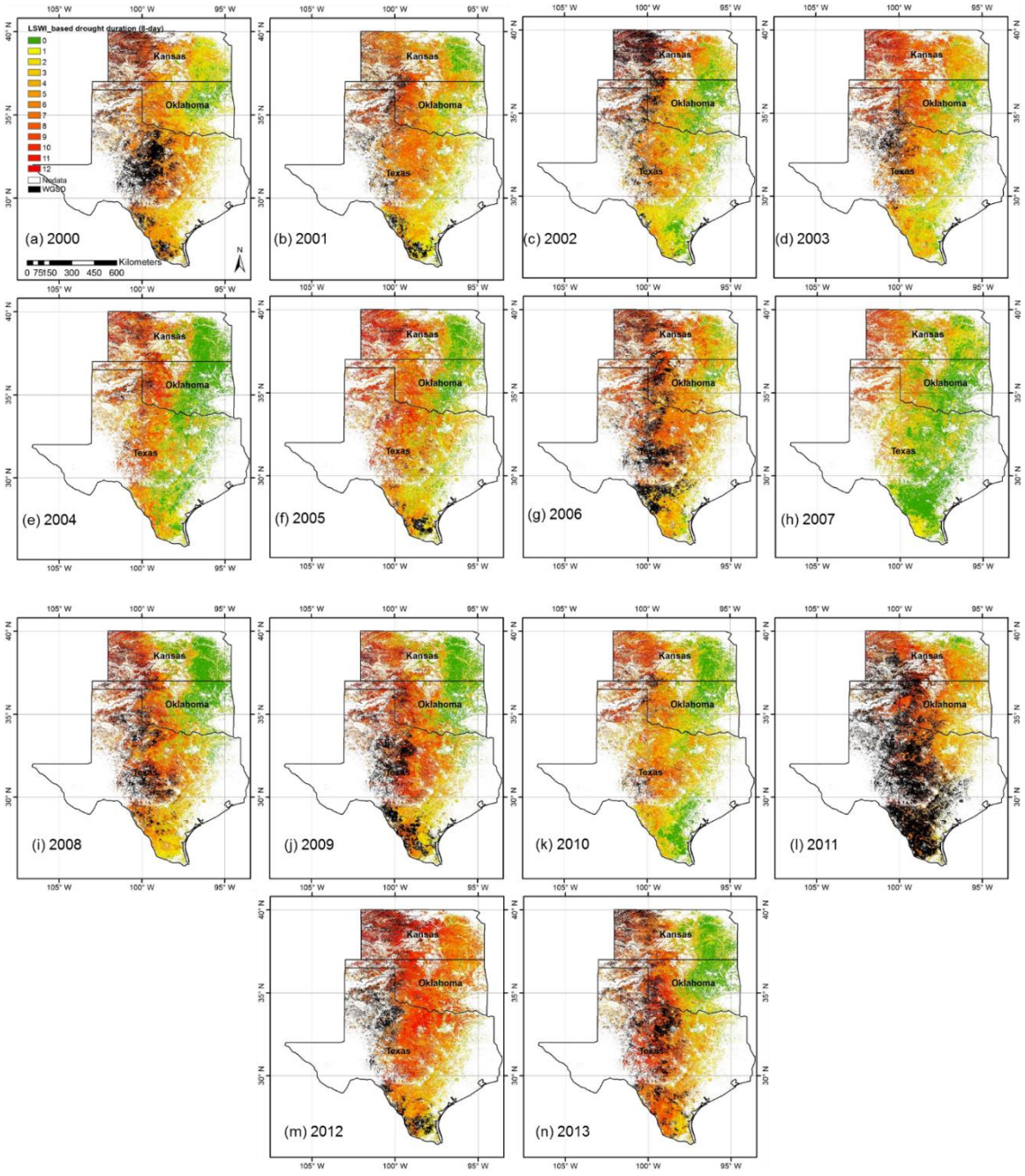


Figure S4.3 Drought dynamics in the SGP for 2000-2013 mean.

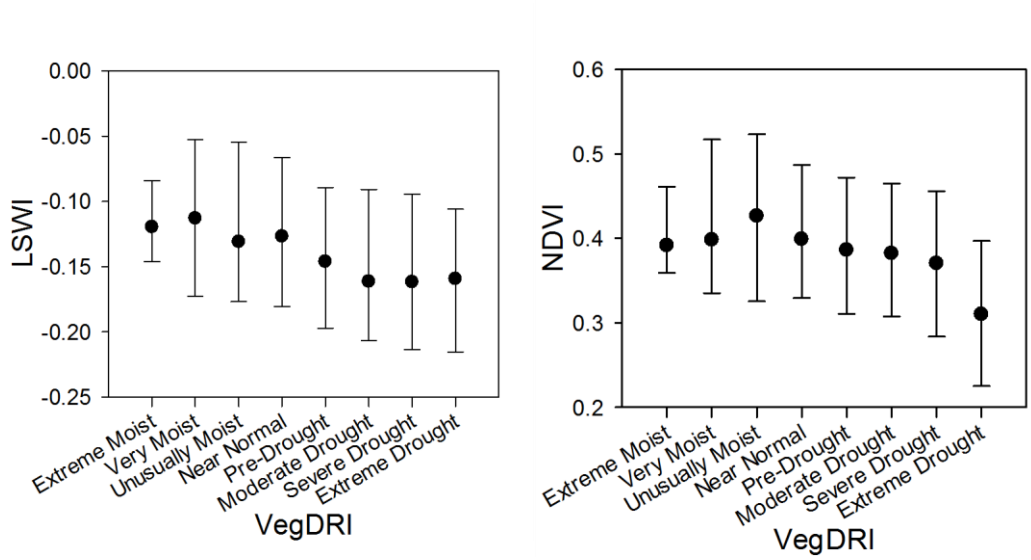


Figure S4.4 LSWI and NDVI vs. VegDRI for the last week of August in 2012.

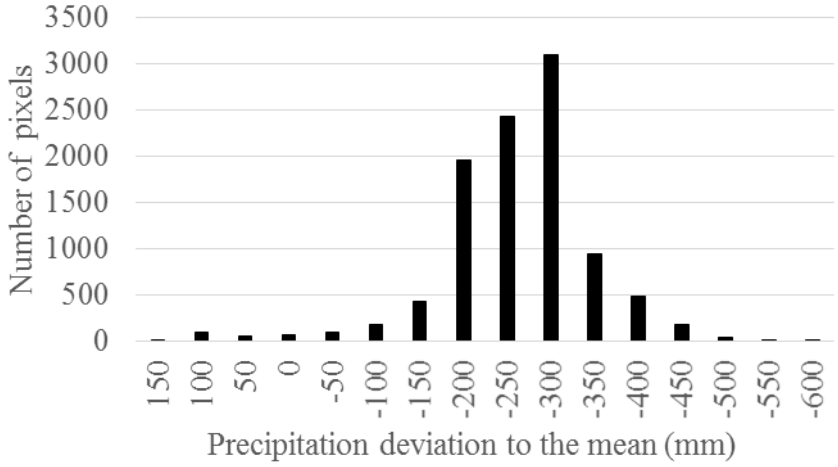


Figure S4.5 Distribution of the annual precipitation deviation from the mean in 2011.

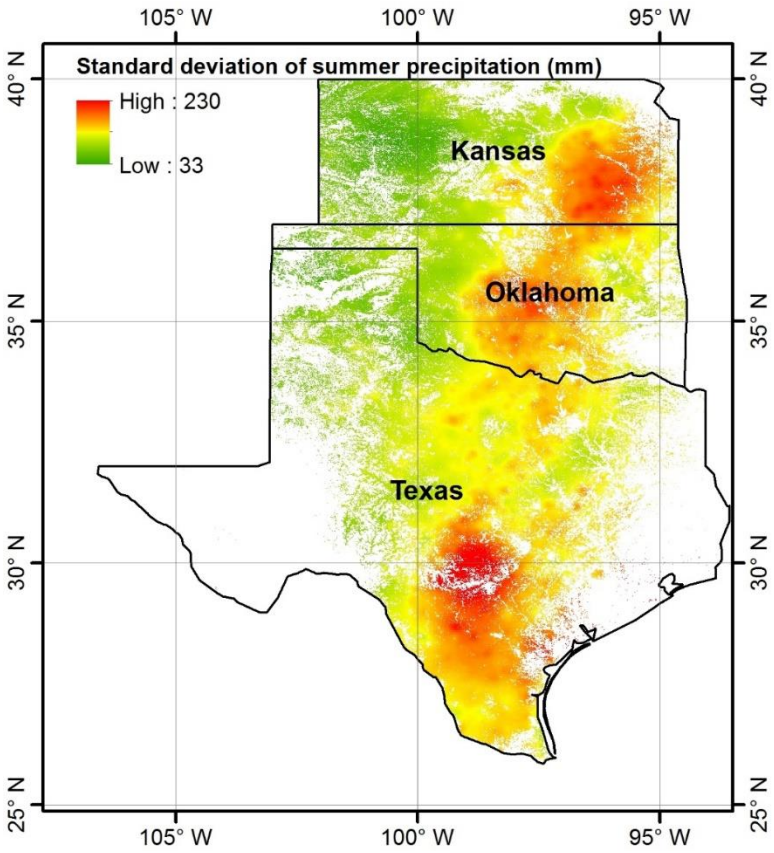


Figure S4.6 Standard deviation of summer precipitation during 2000-2013.

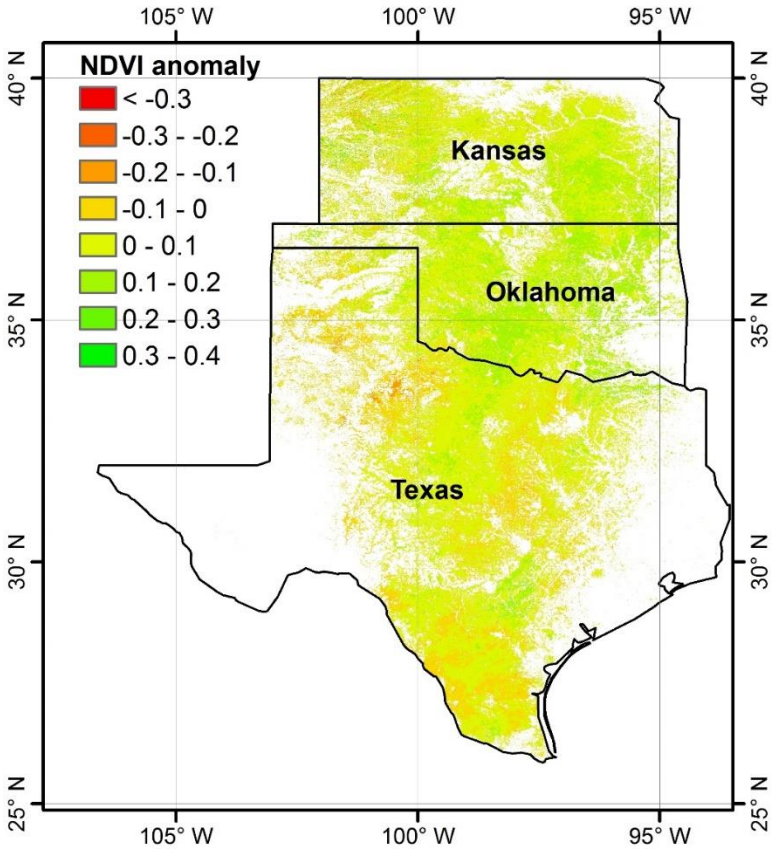


Figure S4.7 NDVI anomaly in early growing season of 2012 (March-May) relative to the baseline of 2000 - 2011. The inset shows the distribution of area percent of NDVI anomalies.

Chapter 5: Consecutive years of agricultural drought and heatwave drove the large losses of cattle production in the U.S. Southern Great Plains

Abstract

Cattle ranching is an important agricultural and economic activity in the Southern Great Plains (SGP: Kansas, Oklahoma, and Texas) of the United States (U.S.) and provides nutritional quality beef for the U.S. and the world. Agricultural drought can harm the cattle production through reducing the feed (forage and grain) production, availability, accessibility, and affordability. In this study, we combine meteorological, remote sensing, and agricultural statistics data to investigate the impacts of drought and heatwave on cattle production in the SGP during 2000-2015. Both 2011 and 2012 were severe drought years in the SGP. Precipitation in 2011 was low for the whole year, which triggered a drought for the entire growing season. High precipitation occurred in the early growing season in 2012, but a lack of precipitation in the summer generated a severe summer drought. Grasslands were mostly affected in 2011 because most ranchers do not have irrigation systems. The decrease in grassland and hay production harmed the cow-calf operators who highly depend on the grasslands in ranches. Cropland (e.g., corn) production was reduced and crop prices increased because of severe summer drought in 2012. Limited availability and the high price of grain (mainly corn) and grain by-products burdened the feedlot operators who depend on grain to quickly finish cattle for slaughter. The high temperature could have slowed cattle's growth and reduced reproductive rates, which increased costs for cattle producers and consumers. We concluded that the consecutive years of agricultural drought and high

temperatues in 2011 and 2012 drove the large losses of cattle production in the SGP because of reduced feed availability, suppressed cattle growth, and low rates of cattle reproduction.

5.1 Introduction

Cattle ranching is of great importance in the Southern Great Plains (SGP: Kansas, Oklahoma, and Texas) of the United States (U.S.). Kansas, Oklahoma, and Texas rank in the top five, according to the all cattle and calves inventory in 2015 (source: United States Department of Agriculture National Agricultural Statistics Service, USDA-NASS). It provides nutritional quality beef for the U.S. and the world. However, frequent agricultural droughts in the area (Andreadis et al. 2005; Bajgain et al. 2016; Basara et al. 2013; Christian et al. 2015; Gu et al. 2007; Gu et al. 2008; Hoerling et al. 2014; Schubert et al. 2004; Worster 1979) affect the crop and forage production which, in turn, threaten the viability of the cattle industry in the SGP (Garbrecht 2015; Osei et al. 2015). Cattle production systems are complex including beef and dairy cattle production systems and with different phases (Fig. 5.1). For example, the beef cattle production systems could include cow-calf phase, backgrounding phase, and finishing/feedlot phase. Cattle production systems are affected by many factors, including the supply and demand of the beef and milk, cattle diseases, vegetation, climate, and government intervention, etc. (Damron 2013). The impacts of these factors on different phases of beef and dairy cattle production systems are various because of their demand on and availability of water and food resources. Thus, it is challenging to isolate the impacts of a single factor such as agricultural drought on cattle production because of the complexity of the problem.

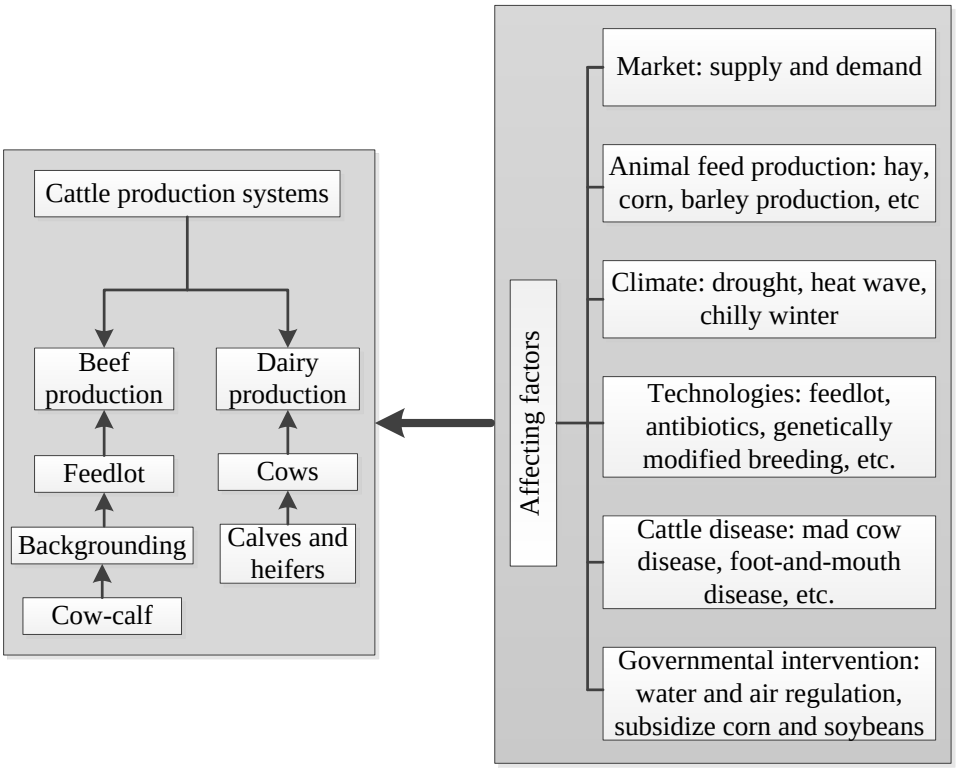


Figure 5.1. A list of major factors affecting cattle production systems

During a short period with little changes in technologies and government intervention for cattle production and no outbreaks of cattle diseases, the major affecting factors are market, animal feed production, and climate. Thus, it is possible to capture the impacts of these factors on cattle production during a short period in which the dynamics of technologies, governmental intervention, and cattle disease are relatively small. The market, in terms of beef and dairy supply and demand, plays an important role in determining cattle production (Delgado 2005; Preston and Willis 2013) as either beef or dairy is a merchandise and is manipulated by the law of value. Animal feed production, especially hay and corn production, is one of the important factors affecting cattle production (Damron 2013; Preston and Willis 2013). Severe agricultural drought can reduce the forage and crop production, thus the feeding for

cattle in the SGP. In addition, evaporative cooling, in the form of sweating and panting, is the principle mechanism for cattle to dissipate heat (Blackshaw and Blackshaw 1994). Following exposure to heat, cattle may increase respiration rate and body temperature, and reduce feed intake (Hahn 1999). The failure of homeostasis caused by heat stress during the severe drought period may lead to reduced productivity or even cattle mortality (Blackshaw and Blackshaw 1994; Vitali et al. 2015).

The objective of this study is twofold: (1) to assess the impacts of agricultural drought and heatwave on cattle production in the SGP; and (2) to build a model to characterize the dynamics of cattle production in the SGP using market, vegetation, and climate factors during 2000-2015. Agricultural statistics data from the USDA-NASS including beef price, beef consumption, hay production, and grain price were used to represent the market and vegetation factors on cattle production. Meteorological data were included to indicate the temperature and water resources stress on cattle. Two drought indices, namely the Standardized Precipitation Index (SPI) (McKee et al. 1993, 1995) and the Evaporative Stress Index (ESI) (Anderson et al. 2013; Anderson et al. 2011; Anderson et al. 2007), were also included to represent drought stress. The multiple linear regression and Random Forests were used to build the model and analyze the importance of those affecting factors.

5.2 Materials and methods

5.2.1 Study area

This study focuses on the Southern Great Plains in the U.S., specifically including Kansas (KS), Oklahoma (OK), and Texas (TX). The mean annual precipitation decrease from the east (1400 mm) to the west (200-400 mm) across the

region. Both inter- and intra-annual precipitation are highly variable (Christian et al. 2015; Flanagan et al. 2017; Weaver et al. 2016). Maximum temperatures in summer are usually coincident with low humidity and strong winds, which in turn generate high rates of soil moisture depletion through ET. Most of the area is covered by sub-humid grassland and semiarid grazing land. Wheat (spring wheat in the north and winter wheat in the south) and corn are the major crop types (Tyler et al. 2015). Soil types are mainly sandy and clay with small surface slopes (Carter 1994).

5.2.2. Data

5.2.2.1. Meteorological data

Annual maximum temperature (T_{max}), minimum temperature (T_{min}), and precipitation (Precip) data were collected from the National Oceanic and Atmospheric Administration (NOAA) National Centers for Environmental Information (NCEI) for KS, OK, and TX during 2000-2015. Cattle consume significantly more water during warmer temperatures and the periods of high temperature can increase the temperature stress and lead to a loss of productivity. Extremely high temperature could result in an increase of cattle mortality (Vitali et al. 2015). Cattle exposed to cold weather require more energy to maintain their body reserves and body temperatures (Belasco et al. 2016). Precipitation is the water source for vegetation growth and surface water bodies, which is the important water supply for cattle in ranches.

5.2.2.2. Standardized Precipitation Index and Evaporative Stress Index

Two widely used drought indices, namely SPI and ESI, were used to characterize drought during 2000-2015. SPI characterizes drought and anomalous wet

periods through depicting the anomaly of precipitation to the historical mean at different time scales(Hayes et al. 1999). Common time scales are 3, 6, and 12 months. The 12 month SPI (SPI-12) reflects long-term precipitation patterns and is used to indicate year long drought. ESI characterizes drought at different time scales (1, 2, and 3 months) through describing temporal anomalies in evapotranspiration (ET) based on surface energy balance model and satellite remote sensing data. The 3-month composite ESI (ESI-3) ending at the last week of August is used to reflect summer drought.

5.2.2.3. Agricultural statistics data from USDA National Agricultural Statistics Service

Cattle production (for each state of the SGP), beef price (for the US), and beef consumption (for the US) data from the USDA-NASS (https://www.nass.usda.gov/Quick_Stats/) were used to reflect the dynamics of cattle industry during 2000-2015. The county level cattle production data were also included to show the spatial distribution of cattle production anomalies in representative years (2010, 2011, and 2012). There are many different categories for cattle statistics such as cattle on feed, beef cows, milk cows, etc. To simplify the problem, only cattle include calves (total cattle number) is used in this study.

Animal feed (forage and grain) production, is affected by drought as most of crop and grass producing fields rely on rainfall. Hay production data for each state during 2000-2015 were collected from the USDA-NASS. As the vast majority of the slaughter cattle in the US are fed on corn-based grain to quickly gain weight in feedlots before they are sent to slaughter houses, the corn price plays an important role in determining the cattle production. We included the dynamics of corn prices in our analysis.

5.2.3. Statistical analysis

To quantitatively describe the impacts of socioeconomic and environmental factors on cattle production, we used the multiple linear regression to build statistical models of cattle production using T_{max}, T_{min}, Precip, SPI-12, ESI-3, hay production, corn production, beef price and beef consumption as independent variables. R-square (R^2) and residual standard error (RSE) were used to evaluate the performance of the model. As some of these variables might be correlated, for example, beef price and beef consumption, we used stepwise linear regression. Another ensemble machine learning method, the Random Forests (Breiman 2001; Liaw and Wiener 2002), is also used in regression models. In addition to the performance evaluation matrix (R^2 and mean squared error (MSE)), the importance of variables was ranked by the Random Forests regression method.

5.3 Results

5.3.1 Spatial distribution and annual dynamics of cattle production in the SGP

Western counties in the SGP had the most of total cattle number (all cattle and calves category from USDA-NASS) which is overlapped with the Ogallala Aquifer. Central OK and eastern TX are another two areas with high density of total cattle number (Fig. 5.2a). The areas with larger total cattle number usually have bigger standard deviation during 2000-2015 (Fig. 5.2b). The anomalies of the total cattle number in 2010 were mostly near zero with TX pan handle seeing a relatively large increase (Fig. 5.3a). In 2011, most of the counties lose a big amount of cattle and calves (more than 6000 head), especially in middle OK and east TX with more than 14000 head decrease. The extent of decrease in western counties in the SGP was less than

central OK and eastern TX (Fig. 5.3b). In 2012, the decrease in the total cattle number continued but with a larger spatial extent (Fig. 5.3c). It is also noteworthy that several counties in KS and western TX even increased the amount of cattle and calves in 2011 and 2012.

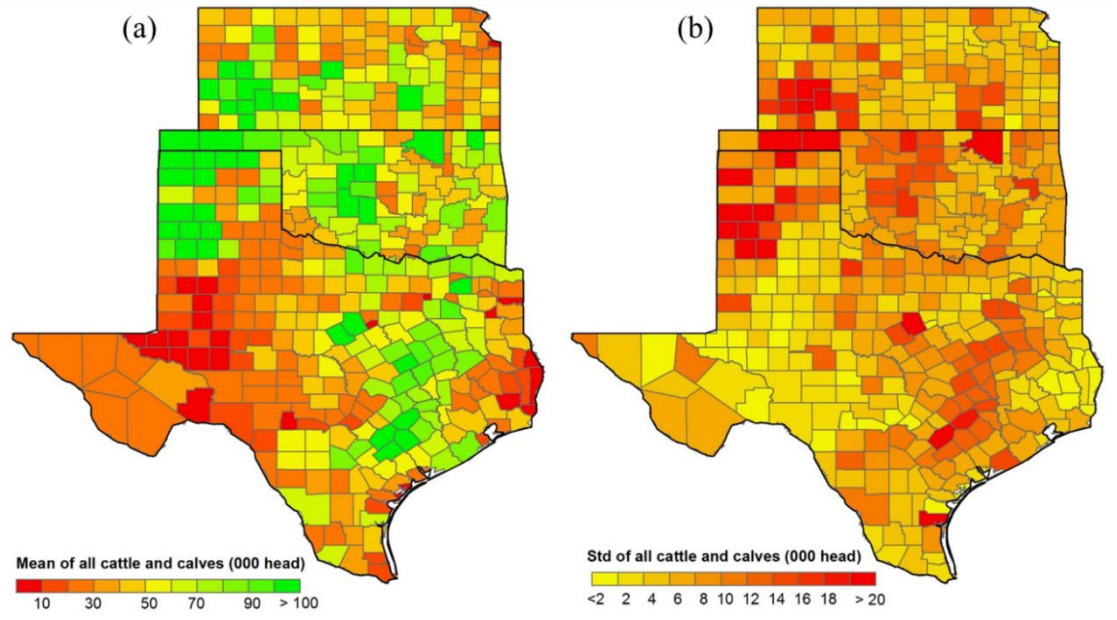


Figure 5.2. Mean and standard deviation of all cattle and calves for 2000-2015

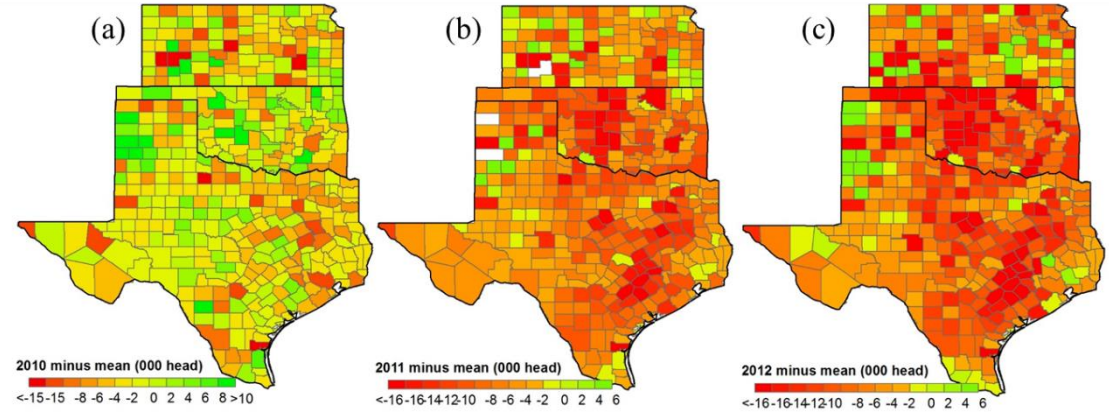


Figure 5.3. Anomalies of all cattle and calves in 2010-2012

For the period between 2000 and 2010, the total cattle number were stable for all three states (Fig. 5.4). However, there was a sharp drop in the total cattle number in 2011 and 2012 for both OK and TX. The total cattle number bounced back after 2012 in OK while it continued to decrease until 2013 in TX. KS also experienced decreasing in the total cattle number in 2011 and 2012. However, the extent was much smaller than the other two states.

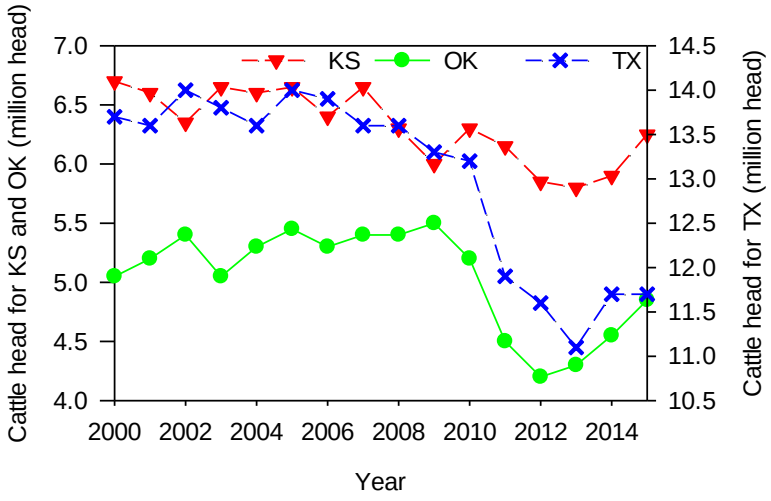


Figure 5.4. Dynamics of cattle production during 2000-2015

5.3.2. Drought and heatwave conditions during 2000-2015

5.3.2.1. Spatial distribution of drought-affected regions in the US in 2010-2012

The SPI-12 values were close to zero for the SGP in 2010 while it ranged from 1 to 2 for the Corn Belt indicating a wet condition for that area (Fig. 5.5a). The ESI-3 values were around zero in summer 2010 for both the SGP and Corn Belt showing no summer drought for both regions (Fig. 5.5b). In 2011, the SPI-12 values were below -2 for most of the SGP indicating severely dry conditions and some of the western region even had SPI-12 values less than -3 indicating extremely dry conditions (Fig. 5.5c). The

ESI-3 values were very low in 2011 in the SGP indicating severe summer drought (Fig. 5.5d), which was caused by abnormally low rainfall for the whole year indicated by the SPI-12 in 2011. In 2012, the SPI-12 values ranged from -1 to 1 in the SGP indicating near normal conditions (Fig. 5.5e). However, the Corn Belt were affected by drought with the SPI-12 values less than -1 (Fig. 5.5e). The ESI-3 indicated summer drought for KS and OK in 2012 while it was near normal in most of the TX (Fig. 5.5f). However, the Corn Belt was affected by extreme drought with ESI-3 less than -2 (Fig. 5.5f). Thus, it is clear that 2011 was a whole growing season drought year for the SGP while 2012 was a summer drought year for the Corn Belt.

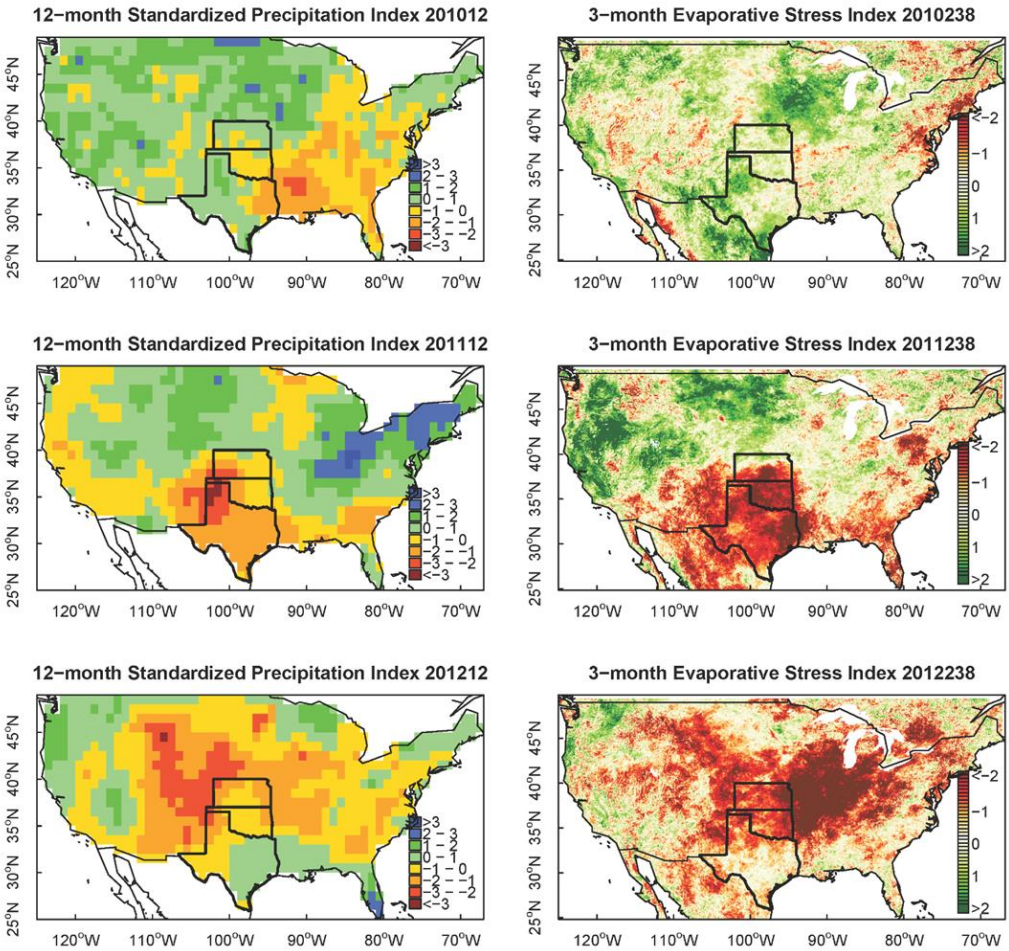


Figure 5.5. SPI-12 and ESI-3 in 2010, 2011, and 2012 (Showing US with SGP outlined)

5.3.2.2. Severe drought and heatwave years from meteorological data at state level

The variation of annual Precip was large for the states in the SGP (Fig. 5.6a). 2012 was the lowest Precip year for KS (30% lower than the mean) and OK (47%) while 2011 had least Precip in TX (47%). T_{max} in 2006 was more than 1˚C higher than the mean in each of the three states. 2011 and 2012 were two continuously hot years for both OK and TX. T_{max} in 2011 was more than 2˚C higher than the mean in KS. T_{max} values were relatively stable for other years (Fig. 5.6b). The dynamics of T_{min} were small with a clear high peak in 2012 for all three states (Fig. 5.6c).

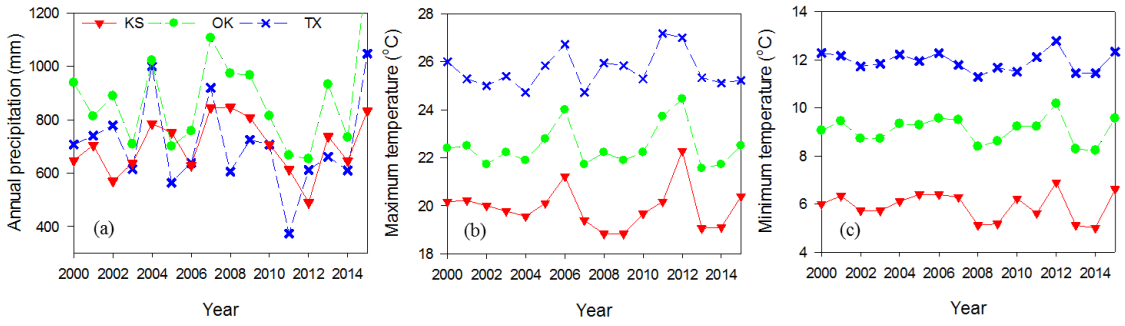


Figure 5.6. Dynamics of annual precipitation (Precip), maximum temperature (Tmax), and minimum temperature (Tmin) during 2000-2013

5.3.3. Dynamics of animal feed production for cattle

The hay production was greatly reduced in 2011 (>50% reduction in OK and TX and 35% reduction in KS) for all three states (Fig. 5.7a). The hay production returned to normal in 2012 in TX while it was still low in OK and KS. The prices of the major grain (corn, wheat, barley, and sorghum) were mostly synchronous with an increasing trend throughout the study years (Fig. 5.7b). Thus, the corn price, major animal feed supply

for feedlot cattle, was used in later analysis. There were two high peaks in the grain prices centered in 2008 and 2012.

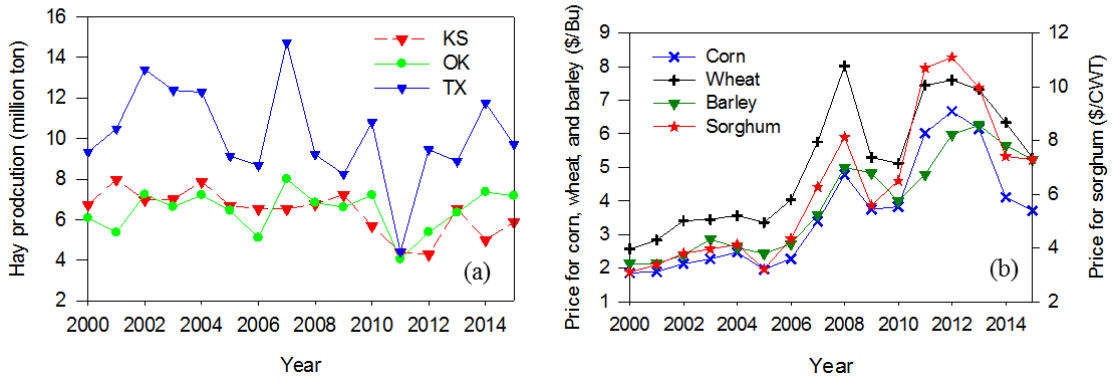


Figure 5.7. Dynamics of hay production and grain prices during 2000-2015

5.3.4. Dynamics of the cattle market

The beef price was continuously increasing during the whole study period (Fig. 5.8a). However, the increasing trend could be divided into two segments: 2000-2010 and 2011-2015. The increasing rate after 2010 was evidently larger than before. With the increasing beef price, the beef consumption decreased dramatically, especially after 2007 (Fig. 5.8b).

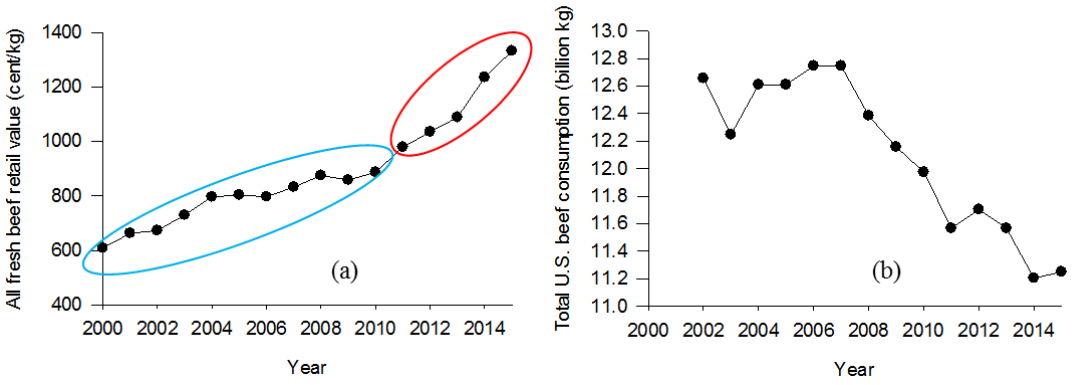


Figure 5.8. Dynamics of the market during 2000-2015. (a) Beef price and (b) beef consumption

5.3.5. Statistical models between cattle production and driving factors over years

The stepwise multiple linear regression models picked up different independent variables for each state (Table. 5.1). Among them, beef consumption and T_{min} were always included in the models. T_{max}, Precip, beef price, and corn price were included in two models. The remaining variables, namely hay production, SPI12, and ESI3 were only included in one model. Along the increasing temperature gradient, the models performed better with increasing R^2 values and significant levels (decreasing P values). MSE was smallest for TX considering the total size of the cattle number.

Table 5.1. Results from stepwise linear regression models for each state

	KS_cattle	OK_cattle	TX_cattle
Intercept	18.2872	10.6457	24.0916
Tmax	-0.3659	-0.0623	
Tmin	0.669	-0.2437	-0.347
Precip	0.0077		-0.0022
Beef price	-0.0044	0.0042	
Beef consuption	-1.5467	0.6623	0.8385
Hay production	0.2568		
Corn price		-0.227	-0.2851
SPI12			0.3424
ESI3	-1.3161		
R^2	0.89	0.91	0.98
P	0.0304	0.0019	<0.0001
RSE	0.0903	0.1233	0.1166

The performances of the Random Forests models (R^2) also increased along the increasing temperature gradient (Fig. 5.9). The values of R^2 were smaller than those from the corresponding stepwise multiple linear regression models. All the Random Forests models ranked beef price, corn price, and beef consumption as the three most important factors. Moreover, we can identify the increased importance of the drought indicators along the increasing temperature gradient. Specifically, ESI3 and SPI12 were ranked closer to the three most important variables in OK and TX than in KS (Fig. 5.9 left panels). Since the Random Forests model is supposed to perform better with larger

datasets, we also run the Random Forests model using all the state-years data. Overall, the new model performed very well with an R^2 equal to 0.96 (Fig. 5.10). However, the importance of variables changed with T_{min}, T_{max}, and hay production ranked as the three most important variables.

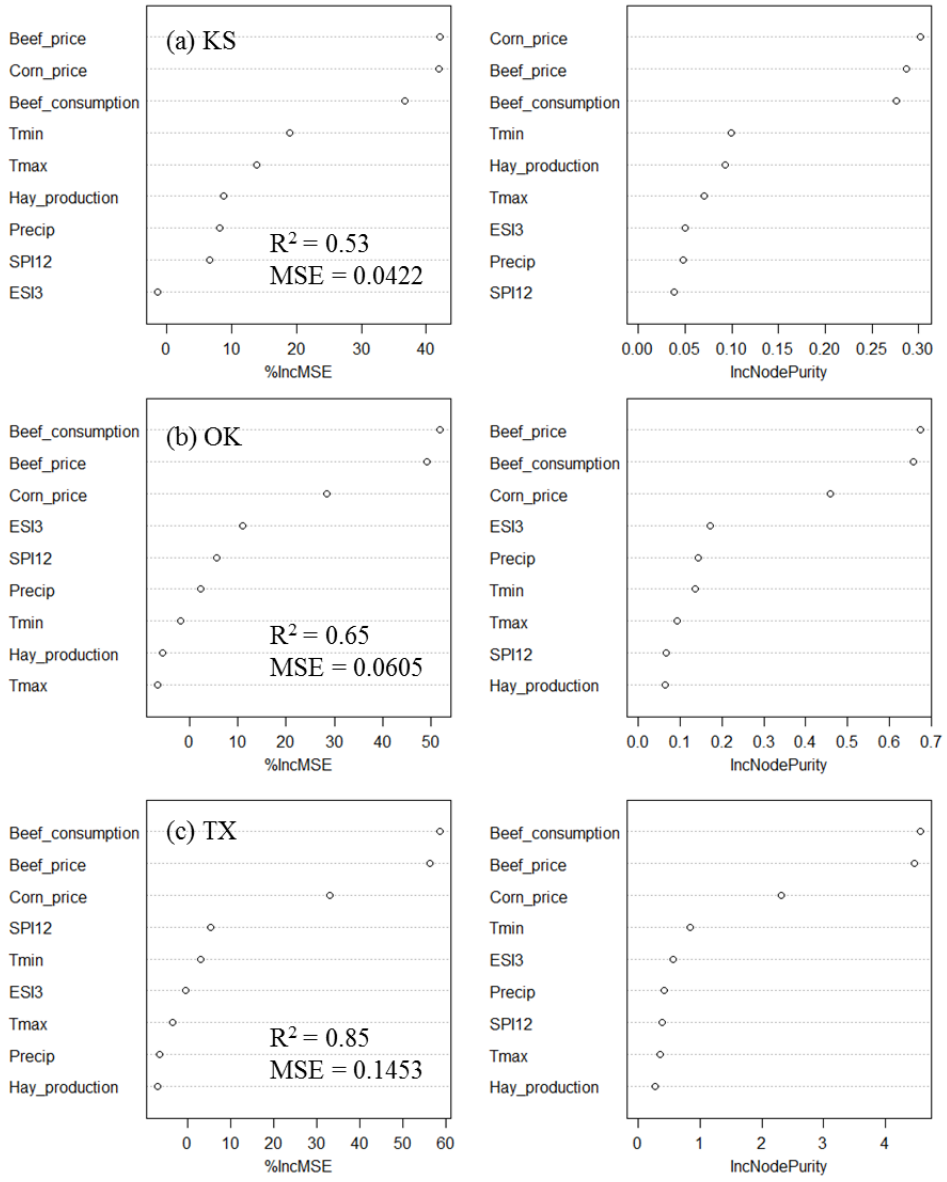


Figure 5.9. Results from the Random Forests for KS (a), OK (b), and TX (c). The graphs show the importance of variables calculated by the Random Forests. Figures in left panels and right panels show the importance of variables from different perspectives. Larger values indicate higher importance. The percent of variance explained (R^2) and mean squared error (MSE) were inserted in the corresponding panels.

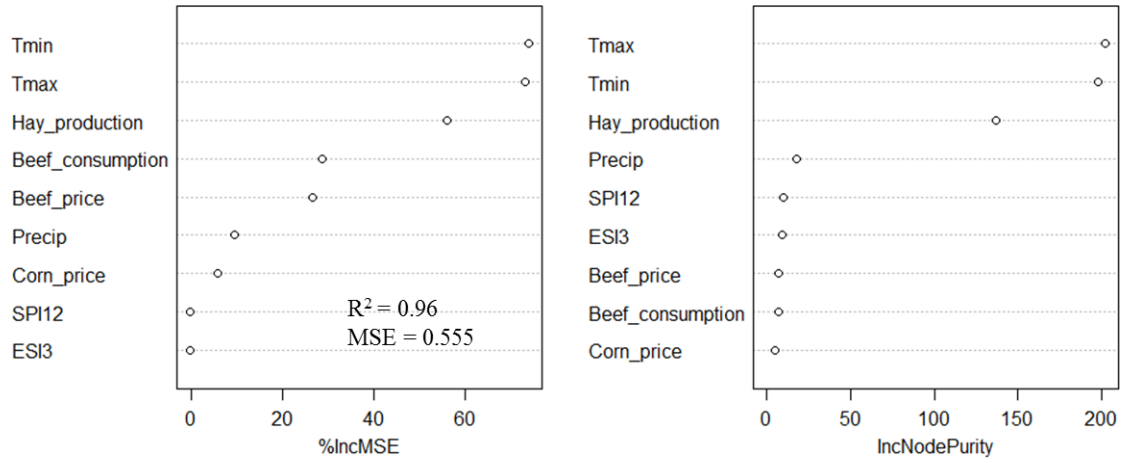


Figure 5.10. Results from the Random Forests using all the state-years data.

5.4 Discussion

5.4.1. Impacts of drought and heatwave on the cattle production

Our results showed that the two consecutive drought years, 2011 and 2012, dramatically decreased the cattle production in the SGP, especially in OK and TX (Fig. 5.4). In 2011, the whole year drought (Fig. 5.5c) reduced the hay production (Fig. 5.7a), the important food supply for cattle ranching, thus leading to the big decrease in the cattle production. In contrast, 2012 was not a very severe drought year in the SGP but the cattle production was still decreased. The reason lies on that severe summer drought happened in the Corn Belt (Fig. 5.5f) increased the corn price (Boyer et al. 2013; Lobell et al. 2014) which is the major food for feedlot cattle. This result demonstrates that droughts can impact the cattle production through different mechanisms because of different spatial and temporal extent. It also indicates the importance of telecoupling (socioeconomic and environmental interactions between coupled human-natural systems over distances) in studying system dynamics (Liu et al. 2007; Liu et al. 2013; Liu et al. 2015).

The cattle production is supposed to be relatively resistant to slight drought conditions. For example, 2006 was a dry year in OK and TX with above normal T_{max} (Fig. 5.6a) and decreased hay production (Fig. 5.7a). However, the cattle production was not clearly different than other years within the 2000-2010 period. When a severe drought happened, like in 2011 and 2012, we see the comprehensive impacts of drought including high maximum temperature, low hay production, and high corn price (Wilhite et al. 2007). Combined together, these factors greatly increased the cost of cattle raising and reduced the profit margin (Belasco et al. 2016; Vitali et al. 2015) which, in turn, dramatically decreased the cattle production. In consecutive years of drought, the impacts are more severe and persistent as it takes time for the cattle industry to recover (Osei et al. 2015). The calf is usually born within a 12-month interval and it takes another year to produce milk or be mature enough for beef production. Our results indicate that drought and the accompanying heatwave caused the large losses of cattle production in the SGP (Belasco et al. 2016; Blackshaw and Blackshaw 1994; Bohmanova et al. 2007; Hahn 1999; Vitali et al. 2015; West 2003).

5.4.2. Model the dynamics of the cattle production

We modeled the dynamics of the cattle production during 2000-2015 using the multiple linear regression and the Random Forests approaches (Table 5.1, Fig. 5.9 and 10). Both methods performed well in terms of the coefficient of determination (high R^2 values). The performances of the Random Forests models were not better than the multiple linear regression models in corresponding states. However, the performance of the Random Forests (R^2 =0.96) was very good when combining all the state-years data (Fig. 5.10). This might be due to the better performance of the Random Forests in

bigger datasets which needs big data samples to build the regression trees. Although the Random Forests did not show the structure of the model, it did give the importance of variables (Breiman 2001; Liaw and Wiener 2002). The beef price, corn price, and beef consumption were ranked as the three most important factors in each state (Fig. 5.9) while T_{max}, T_{min}, and hay production were the most important parameters in determining the cattle production when combining all the state-years (Fig. 5.10). The increasing temperature gradient from KS to OK and TX might cause this difference as the variation of temperatures were relatively small when running the model by state.

Although corn is the major food supply for feedlot cattle, the corn price was not included in all of the stepwise multiple linear regression (Table 5.1) and it was also not an important parameter in the all state-year Random Forests model (Fig. 5.10). The reason is that the corn price was jointly driven by both the market and climate. Fox example, the high prices in 2008 was because of global food crisis (Headey and Fan 2008; Mueller et al. 2011). The high prices in 2011 and 2012 were mostly attributed to drought (Wan et al. 2015). It is apparent that the corn price is important for the cattle production, but we need to find a better way to incorporate it into the model.

5.4.3. Other factors affecting the cattle production beside of droughts

The cattle production systems are complex and affected by many factors (Damron 2013). We demonstrated that the consecutive years of drought drove the big loss of the cattle production in the SGP and modeled the dynamics of the cattle production using climate, animal feed production, and market parameters. This analysis was under the assumption that the dynamics of technologies and governmental intervention for cattle production were small and no outbreak of cattle diseases.

However, this assumption might not hold in some instances. For example, introduce of feedlot significantly boosted the cattle production in 1970 (Damron 2013; Menkhaus et al. 1981).

The sensitivity to drought could be different among regions depending on the availability of the groundwater resources (Hornbeck and Keskin 2014; Peters 2003). KS was mostly depended on groundwater for livestock usage and the ratio of groundwater to surface water increased from 2005 to 2010 (Table 5.2). That might be a good explanation of the much smaller decrease extent for the cattle production in KS than in OK and TX, even under two consecutive years of severe drought. As mentioned before, the cattle production in several counties in KS and western TX even significantly increased during drought (Fig. 5.3b and c) Those counties with increasing cattle numbers were overlapped with the Ogallala Aquifer, one of the world's largest aquifers (Torell et al. 1990). Cattle ranchers with easy access to the groundwater resources (Long et al. 2013; Rosenberg et al. 1999) might increase the cattle stock to utilize the increasing beef price in drought to gain more profit. However, this phenomenon needs to be further explored at the county level.

Table 5.2. Livestock water withdrawals in 2005 and 2010. Values may not sum to totals because of independent rounding.

	Ground water-2005	Surface water-2005	Total-2005	Ratio-2005	Ground water-2010	Surface water-2010	Total-2010	Ratio-2010
KS	84.3	23.8	108	3.5420168	91	23	114	3.9565217
OK	54.7	107	162	0.511215	32.5	56.3	88.8	0.5772647
TX	162	95.9	258	1.6892596	131	127	259	1.0314961

5.5 Conclusion

This study investigated the impacts of drought and heatwave on the cattle production in the SGP during 2000-2015 using meteorological, remote sensing, and agricultural statistical data. The consecutive years of drought and heatwave in 2011 and 2012 dramatically decreased the cattle production in OK and TX. The decrease extent in KS was smaller probably because of its greater accessibility to the groundwater resource than OK and TX. 2011 was a whole growing season drought year in the SGP which decreased the hay production and thus cattle production, while 2012 was a summer drought year in the Corn Belt which dramatically increased the corn price and thus decreased cattle production. It implicates that when studying a local phenomenon, it is necessary to consider the interaction between relevant systems. Using market, animal feed production, and climate factors, we modeled the dynamics of the cattle production using two different statistical models. The factors included in the stepwise multiple linear regression were different for the three states. Along the increasing temperature gradient, the performances of models increased. The Random Forests method performed well for the all state-years data and shows the potential in predicting the dynamics of cattle production. Longer periods of estimation of the cattle production needs to consider other factors including technologies, governmental intervention, and cattle disease.

Chapter 6: Conclusions and perspectives

Remote sensing has been widely used in LULCC and drought monitoring because of its high spatial and temporal resolutions. Eddy covariance technique has been popular in studying ecosystem carbon, water vapor, and energy dynamics. It is important to facilitate the usage of remote sensing and eddy covariance technologies in characterizing cropland, drought and land management. My dissertation aims to strengthen the usage of remote sensing and eddy covariance technologies to characterize cropland, drought and management and their impacts on ecosystem dynamics through four case studies including paddy rice mapping, agricultural drought monitoring, land management effects assessment, and evaluating the impacts of drought on cattle production.

Chapter 2 develop a new phenology-based paddy rice mapping algorithm to map paddy rice planting area from the rice-wetland coexistent area using MODIS and Landsat 8 imagery. The comparison and validation tests indicated the high accuracy of our paddy rice map. There is a need to develop a more accurate Landsat- and/or MODIS-based natural wetland mask in the future to further improve the accuracy of the paddy rice mapping. The combination of Landsat 7, 8, and MODIS imagery can open up many more possibilities for the mapping of paddy rice in complex landscapes.

Chapter 3 used digital repeat photography (PhenoCam), satellite remote sensing, and the eddy covariance technique to investigate the impacts of burning, baling, and grazing on plant phenology and carbon fluxes in an Old World bluestems pasture. Multiple datasets allowed studying intra-annual variations caused by various management practices. The larger increase of GPP after large rain in baled grassland

(photosynthetically more active vegetation) compensated the reduction in GPP caused by baling. This result indicated that the interaction of management practices with climate is important when studying their impacts on GPP. Since management practices are often complex (e.g, grazing and baling in the pasture), we need multiyear data from different sources for a better understanding of individual and confounding impacts of those management practices. Investigation of the dynamics of EC footprint and its relative geolocation to affected area is important when evaluating the impacts of management practices.

Chapter 4 expanded and applied an LSWI-based drought algorithm to map agricultural drought of tallgrass prairie in the SGP. The results are comparable to other widely used drought products. The spatial pattern of drought duration was highly correlated with the decreasing precipitation gradient from east to west. In the most severe WGSD years, the area affected by WGSD was more than double of the mean value. LSWI-based drought depictions are sensitive to both precipitation anomalies from the historical mean and abnormal seasonal precipitation distributions. Future studies should incorporate LSWI into other drought products to improve their performance and further explore LSWI thresholds to identify agricultural drought and develop LSWI-based drought severity schemes for other land cover types.

Chapter 5 found that the consecutive years of drought and heatwave in 2011 and 2012 dramatically decreased the cattle production in OK and TX. The decrease extent in KS was smaller probably because of the greater accessibility to the groundwater resource. 2011 was a whole year drought in the SGP which decreased the hay production and thus cattle production, while 2012 was a summer drought year in the

Corn Belt which increased the corn price and thus cattle production. It implicates that when studying a local phenomenon, it is necessary to consider the interaction between relevant systems. Longer periods of estimation of the cattle production needs to consider other factors including technologies, governmental intervention, and cattle disease.

References

Adler-Golden, S.M., Matthew, M.W., Bernstein, L.S., Levine, R.Y., Berk, A., Richtsmeier, S.C., Acharya, P.K., Anderson, G.P., Felde, G., & Gardner, J. (1999). Atmospheric correction for short-wave spectral imagery based on MODTRAN 4. In, *PROC SPIE INT SOC OPT ENG* (pp. 61-69)

AghaKouchak, A., Farahmand, A., Melton, F., Teixeira, J., Anderson, M., Wardlow, B., & Hain, C. (2015). Remote sensing of drought: Progress, challenges and opportunities. *Reviews of Geophysics, 53*, 452-480

AgriLifeToday (2011). Texas Agricultural Drought Losses Reach Record $5.2 Billion

Anderson, M.C., Hain, C., Otkin, J., Zhan, X., Mo, K., Svoboda, M., Wardlow, B., & Pimstein, A. (2013). An intercomparison of drought indicators based on thermal remote sensing and NLDAS-2 simulations with US Drought Monitor classifications. *Journal of Hydrometeorology, 14*, 1035-1056

Anderson, M.C., Hain, C., Wardlow, B., Pimstein, A., Mecikalski, J.R., & Kustas, W.P. (2011). Evaluation of drought indices based on thermal remote sensing of evapotranspiration over the continental United States. *Journal of Climate, 24*, 2025-2044

Anderson, M.C., Hain, C.R., Frantisek, J., Trnka, M., Hlavinka, P., Dulaney, W., Otkin, J.A., Johnson, D., & Gao, F. (2016a). Relationships between the evaporative stress index and winter wheat and spring barley yield anomalies in the Czech Republic. *Climate Research, 70*, 215-230

Anderson, M.C., Norman, J.M., Mecikalski, J.R., Otkin, J.A., & Kustas, W.P. (2007). A climatological study of evapotranspiration and moisture stress across the continental United States based on thermal remote sensing: 2. Surface moisture climatology. *Journal of Geophysical Research: Atmospheres (1984–2012), 112*

Anderson, M.C., Zolin, C.A., Hain, C.R., Semmens, K., Yilmaz, M.T., & Gao, F. (2015). Comparison of satellite-derived LAI and precipitation anomalies over Brazil with a thermal infrared-based Evaporative Stress Index for 2003–2013. *Journal of Hydrology, 526*, 287-302

Anderson, M.C., Zolin, C.A., Sentelhas, P.C., Hain, C.R., Semmens, K., Yilmaz, M.T., Gao, F., Otkin, J.A., & Tetrault, R. (2016b). The Evaporative Stress Index as an

indicator of agricultural drought in Brazil: An assessment based on crop yield impacts. *Remote sensing of Environment, 174*, 82-99

Andreadis, K.M., Clark, E.A., Wood, A.W., Hamlet, A.F., & Lettenmaier, D.P. (2005). Twentieth-century drought in the conterminous United States. *Journal of Hydrometeorology, 6*, 985-1001

Aselmann, I., & Crutzen, P.J. (1989). Global distribution of natural freshwater wetlands and rice paddies, their net primary productivity, seasonality and possible methane emissions. *Journal of atmospheric chemistry, 8*, 307-358

Bachelet, D. (1995). Rice paddy inventory in a few provinces of China using AVHRR data. *Geocarto International, 10*, 23-38

Bajgain, R., Xiao, X., Basara, J., Wagle, P., Zhou, Y., Zhang, Y., & Mahan, H. (2016). Assessing agricultural drought in summer over Oklahoma Mesonet sites using the water-related vegetation index from MODIS. *International Journal of Biometeorology, 10.1007/s00484-016-1218-8*, 1-14

Bajgain, R., Xiao, X., Wagle, P., Basara, J., & Zhou, Y. (2015). Sensitivity analysis of vegetation indices to drought over two tallgrass prairie sites. *ISPRS Journal of Photogrammetry and Remote Sensing, 108*, 151-160

Baldocchi, D., Falge, E., Gu, L., Olson, R., Hollinger, D., Running, S., Anthoni, P., Bernhofer, C., Davis, K., Evans, R., Fuentes, J., Goldstein, A., Katul, G., Law, B., Lee, X., Malhi, Y., Meyers, T., Munger, W., Oechel, W., Paw, K.T., Pilegaard, K., Schmid, H.P., Valentini, R., Verma, S., Vesala, T., Wilson, K., & Wofsy, S. (2001). FLUXNET: A New Tool to Study the Temporal and Spatial Variability of Ecosystem–Scale Carbon Dioxide, Water Vapor, and Energy Flux Densities. *Bulletin of the American Meteorological Society, 82*, 2415-2434

Basara, J.B., Maybourn, J.N., Peirano, C.M., Tate, J.E., Brown, P.J., Hoey, J.D., & Smith, B.R. (2013). Drought and associated impacts in the Great Plains of the United States—A review. *International Journal of Geosciences, 4*, 72

Beddington, J., Asaduzzaman, M., & Clark, M. (2012). Achieving food security in the face of climate change: Final report from the Commission on Sustainable Agriculture and Climate Change

Belasco, E.J., Cheng, Y., & Schroeder, T.C. (2016). The impact of extreme weather on cattle feeding profits. *Journal of Agricultural and Resource Economics, 40,* 285-305

Blackshaw, J., & Blackshaw, A. (1994). Heat stress in cattle and the effect of shade on production and behaviour: a review. *Australian Journal of Experimental Agriculture, 34*, 285-295

Bohmanova, J., Misztal, I., & Cole, J.B. (2007). Temperature-Humidity Indices as Indicators of Milk Production Losses due to Heat Stress. *Journal of Dairy Science, 90,* 1947-1956

Bouman, B., & Tuong, T.P. (2001). Field water management to save water and increase its productivity in irrigated lowland rice. *Agricultural Water Management, 49*, 11-30

Boyer, J., Byrne, P., Cassman, K., Cooper, M., Delmer, D., Greene, T., Gruis, F., Habben, J., Hausmann, N., & Kenny, N. (2013). The US drought of 2012 in perspective: A call to action. *Global Food Security, 2*, 139-143

Breiman, L. (2001). Random Forests. *Machine Learning, 45*, 5-32

Brisco, B., Li, K., Tedford, B., Charbonneau, F., Yun, S., & Murnaghan, K. (2012). Compact polarimetry assessment for rice and wetland mapping. *International Journal of Remote Sensing, 34*, 1949-1964

Brockway, D.G., Gatewood, R.G., & Paris, R.B. (2002). Restoring fire as an ecological process in shortgrass prairie ecosystems: initial effects of prescribed burning during the dormant and growing seasons. *Journal of Environmental Management, 65*, 135-152

Brown, C.R., & Brown, M.B. (2014). Breeding time in a migratory songbird is predicted by drought severity and group size. *Ecology, 95*, 2736-2744

Brown, J.F., Wardlow, B.D., Tadesse, T., Hayes, M.J., & Reed, B.C. (2008). The Vegetation Drought Response Index (VegDRI): A new integrated approach for monitoring drought stress in vegetation. *GIScience & Remote Sensing, 45,* 16-46

Bureau, L.S. (2014). Liaoning statistical yearbook in 2014. *China Statistical Press*

Burges, C.J. (1998). A tutorial on support vector machines for pattern recognition. *Data mining and knowledge discovery, 2*, 121-167

Campioli, M., Vicca, S., Luyssaert, S., Bilcke, J., Ceschia, E., Chapin III, F., Ciais, P., Fernández-Martínez, M., Malhi, Y., & Obersteiner, M. (2015). Biomass production efficiency controlled by management in temperate and boreal ecosystems. *Nature Geoscience, 8*, 843-846

Carter, M.R. (1994). *Conservation tillage in temperate agroecosystems*. Lewis Publishers Inc.

Chandrasekar, K., Sesha Sai, M., Roy, P., & Dwevedi, R. (2010). Land Surface Water Index (LSWI) response to rainfall and NDVI using the MODIS Vegetation Index product. *International Journal of Remote Sensing, 31*, 3987-4005

Chang, C.-C., & Lin, C.-J. (2001). LIBSVM: A library for support vector machines. *ACM Transactions on Intelligent Systems and Technology (TIST), 2*, 27

Chen, B., Coops, N.C., Fu, D., Margolis, H.A., Amiro, B.D., Barr, A.G., Black, T.A., Arain, M.A., Bourque, C.P.-A., & Flanagan, L.B. (2011a). Assessing eddy-covariance flux tower location bias across the Fluxnet-Canada Research Network based on remote sensing and footprint modelling. *Agricultural and Forest Meteorology, 151*, 87-100

Chen, B., Coops, N.C., Fu, D., Margolis, H.A., Amiro, B.D., Black, T.A., Arain, M.A., Barr, A.G., Bourque, C.P.-A., & Flanagan, L.B. (2012). Characterizing spatial representativeness of flux tower eddy-covariance measurements across the Canadian Carbon Program Network using remote sensing and footprint analysis. *Remote Sensing of Environment, 124*, 742-755

Chen, C.-F., Son, N.-T., Chen, C.-R., & Chang, L.-Y. (2011b). Wavelet filtering of time-series moderate resolution imaging spectroradiometer data for rice crop mapping using support vector machines and maximum likelihood classifier. *Journal of Applied Remote Sensing, 5*, 053525-053525-053515

Cheng, Y.-B., Zarco-Tejada, P.J., Riaño, D., Rueda, C.A., & Ustin, S.L. (2006). Estimating vegetation water content with hyperspectral data for different canopy scenarios: Relationships between AVIRIS and MODIS indexes. *Remote Sensing of Environment, 105*, 354-366

Christian, J., Christian, K., & Basara, J.B. (2015). Drought and pluvial dipole events within the great plains of the United States. *Journal of Applied Meteorology and Climatology, 54*, 1886-1898

Dai, A. (2011). Drought under global warming: a review. *Wiley Interdisciplinary Reviews: Climate Change, 2*, 45-65

Damron, W.S. (2013). *Introduction to animal science*. Pearson Higher Ed

Delgado, C. (2005). Rising demand for meat and milk in developing countries: implications for grasslands-based livestock production. *Grassland: a global resource*, 29-39

Döll, P. (2002). Impact of climate change and variability on irrigation requirements: a global perspective. *Climatic Change, 54*, 269-293

Dong, J., Xiao, X., Sheldon, S., Biradar, C., Duong, N.D., & Hazarika, M. (2012a). A comparison of forest cover maps in Mainland Southeast Asia from multiple sources: PALSAR, MERIS, MODIS and FRA. *Remote Sensing of Environment, 127*, 60-73

Dong, J., Xiao, X., Sheldon, S., Biradar, C., & Xie, G. (2012b). Mapping tropical forests and rubber plantations in complex landscapes by integrating PALSAR and MODIS imagery. *ISPRS Journal of Photogrammetry and Remote Sensing, 74*, 20-33

Dong, J., Xiao, X., Sheldon, S., Biradar, C., Zhang, G., Duong, N.D., Hazarika, M., Wikantika, K., Takeuhci, W., & Moore III, B. (2014). A 50-m Forest Cover Map in Southeast Asia from ALOS/PALSAR and Its Application on Forest Fragmentation Assessment. *PloS one, 9*, e85801

Dong, J.W., Xiao, X.M., Wagle, P., Zhang, G.L., Zhou, Y.T., Jin, C., Torn, M.S., Meyers, T.P., Suyker, A.E., Wang, J.B., Yan, H.M., Biradar, C., & Moore, B. (2015). Comparison of four EVI-based models for estimating gross primary production of maize and soybean croplands and tallgrass prairie under severe drought. *Remote Sensing of Environment, 162*, 154-168

Dong, X., Xi, B., Kennedy, A., Feng, Z., Entin, J.K., Houser, P.R., Schiffer, R.A., L'Ecuyer, T., Olson, W.S., & Hsu, K.l. (2011). Investigation of the 2006 drought and 2007 flood extremes at the Southern Great Plains through an integrative analysis of observations. *Journal of Geophysical Research: Atmospheres, 116*

Ellis, E., & Pontius, R. (2007). Land-use and land-cover change. *Encyclopedia of earth*

Falge, E., Baldocchi, D., Olson, R., Anthoni, P., Aubinet, M., Bernhofer, C., Burba, G., Ceulemans, R., Clement, R., & Dolman, H. (2001). Gap filling strategies for defensible annual sums of net ecosystem exchange. *Agricultural and Forest Meteorology, 107*, 43-69

Fang, H. (1998). Rice crop area estimation of an administrative division in China using remote sensing data. *International Journal of Remote Sensing, 19*, 3411-3419

Fannin, B. (2012). Updated 2011 texas agricultural drought losses total $7.62 billion. *Southwest Farm Press, Retrieved from* *http://search.proquest.com/docview/929437522?accountid=12964*

FAO (2013). Statistical Yearbook 2013: World Food and Agriculture. *FAO (Food and Agriculture Organziation of the United Nations), Rome*

Fischer, M.L., Torn, M.S., Billesbach, D.P., Doyle, G., Northup, B., & Biraud, S.C. (2012). Carbon, water, and heat flux responses to experimental burning and drought in a tallgrass prairie. *Agricultural and Forest Meteorology, 166*, 169-174

Flanagan, P.X., Basara, J.B., & Xiao, X. (2017). Long-term analysis of the asynchronicity between temperature and precipitation maxima in the United States Great Plains. *International Journal of Climatology*

Foley, J.A., DeFries, R., Asner, G.P., Barford, C., Bonan, G., Carpenter, S.R., Chapin, F.S., Coe, M.T., Daily, G.C., & Gibbs, H.K. (2005). Global consequences of land use. *science, 309*, 570-574

Friedl, M.A., McIver, D.K., Hodges, J.C., Zhang, X., Muchoney, D., Strahler, A.H., Woodcock, C.E., Gopal, S., Schneider, A., & Cooper, A. (2002). Global land cover mapping from MODIS: algorithms and early results. *Remote Sensing of Environment, 83*, 287-302

Gao, B.-c. (1996). NDWI—A normalized difference water index for remote sensing of vegetation liquid water from space. *Remote Sensing of Environment, 58*, 257-266

Garbrecht, J.D. (2015). Soil water signature of the 2005-2006 drought under tallgrass prairie at Fort Reno, Oklahoma. In, *Proceedings of the Oklahoma Academy of Science* (pp. 37-44)

Gilabert, M.A., & Melia, J. (1990). Usefulness of the temporal analysis and the normalized difference in the study of rice by means of landsat‐5 TM images: Identification and inventory of rice fields. *Geocarto International, 5*, 17-26

Goddard, S., Harms, S.K., Reichenbach, S.E., Tadesse, T., & Waltman, W.J. (2003). Geospatial decision support for drought risk management. *Communications of the ACM, 46*, 35-37

Godfray, H.C.J., Beddington, J.R., Crute, I.R., Haddad, L., Lawrence, D., Muir, J.F., Pretty, J., Robinson, S., Thomas, S.M., & Toulmin, C. (2010). Food security: the challenge of feeding 9 billion people. *science, 327*, 812-818

Gong, P., Niu, Z., Cheng, X., Zhao, K., Zhou, D., Guo, J., Liang, L., Wang, X., Li, D., & Huang, H. (2010). China's wetland change (1990–2000) determined by remote sensing. *Science China Earth Sciences, 53*, 1036-1042

Gu, Y., Brown, J.F., Verdin, J.P., & Wardlow, B. (2007). A five‐year analysis of MODIS NDVI and NDWI for grassland drought assessment over the central Great Plains of the United States. *Geophysical Research Letters, 34*

Gu, Y., Hunt, E., Wardlow, B., Basara, J.B., Brown, J.F., & Verdin, J.P. (2008). Evaluation of MODIS NDVI and NDWI for vegetation drought monitoring using Oklahoma Mesonet soil moisture data. *Geophysical Research Letters, 35*

Hahn, G.L. (1999). Dynamic responses of cattle to thermal heat loads. *Journal of Animal Science, 77*, 10-20

Hall, D.K., Riggs, G.A., Salomonson, V.V., DiGirolamo, N.E., & Bayr, K.J. (2002). MODIS snow-cover products. *Remote Sensing of Environment, 83*, 181-194

Hayes, M., Svoboda, M., Wardlow, B., Anderson, M., & Kogan, F. (2012). Drought monitoring: Historical and current perspectives. *Remote sensing of drought*, 1-19

Hayes, M.J. (2006). *Drought indices*. Wiley Online Library

Hayes, M.J., Svoboda, M.D., Wilhite, D.A., & Vanyarkho, O.V. (1999). Monitoring the 1996 drought using the standardized precipitation index. *Bulletin of the American Meteorological Society, 80*, 429-438

Headey, D., & Fan, S. (2008). Anatomy of a crisis: the causes and consequences of surging food prices. *Agricultural Economics, 39*, 375-391

Hoerling, M., Eischeid, J., Kumar, A., Leung, R., Mariotti, A., Mo, K., Schubert, S., & Seager, R. (2014). Causes and predictability of the 2012 Great Plains drought. *Bulletin of the American Meteorological Society, 95*, 269-282

Hornbeck, R., & Keskin, P. (2014). The historically evolving impact of the ogallala aquifer: Agricultural adaptation to groundwater and drought. *American Economic Journal: Applied Economics, 6*, 190-219

Huete, A., Didan, K., Miura, T., Rodriguez, E.P., Gao, X., & Ferreira, L.G. (2002). Overview of the radiometric and biophysical performance of the MODIS vegetation indices. *Remote Sensing of Environment, 83*, 195-213

Huke, R., & Huke, E. (1997). Rice area by type of culture: South, Southeast, and East Asia. A review and updated data base. *Rice area by type of culture: South, Southeast, and East Asia. A review and updated data base*

Huke, R.E. (1982). *Rice area by type of culture: South, Southeast, and East Asia*. Int. Rice Res. Inst.

IPCC (2013). Climate Change 2013: The Physical Science Basis, Contribution of Working Group I Contribution to the Fifth Assessment Report of Intergovernmental Panel on Climate

Jackson, T.J., Chen, D., Cosh, M., Li, F., Anderson, M., Walthall, C., Doriaswamy, P., & Hunt, E.R. (2004). Vegetation water content mapping using Landsat data derived normalized difference water index for corn and soybeans. *Remote Sensing of Environment, 92*, 475-482

Jensen, J.R. (2009). *Remote Sensing of the Environment: An Earth Resource Perspective*. Pearson Education India

Jin, C., Xiao, X., Dong, J., Qin, Y., & Wang, Z. (2015). Mapping paddy rice distribution using multi-temporal Landsat imagery in the Sanjiang Plain, northeast China. *Frontiers of Earth Science*, 1-14

Jin, C., Xiao, X., Merbold, L., Arneth, A., Veenendaal, E., & Kutsch, W.L. (2013a). Phenology and gross primary production of two dominant savanna woodland ecosystems in Southern Africa. *Remote Sensing of Environment, 135*, 189-201

Jin, C., Xiao, X., Merbold, L., Arneth, A., Veenendaal, E., & Kutsch, W.L. (2013b). Phenology and gross primary production of two dominant savanna woodland ecosystems in Southern Africa. *Remote Sensing of Environment, 135*, 189-201

Kogan, F. (1995). Application of vegetation index and brightness temperature for drought detection. *Advances in Space Research, 15*, 91-100

Lambin, E.F., Turner, B.L., Geist, H.J., Agbola, S.B., Angelsen, A., Bruce, J.W., Coomes, O.T., Dirzo, R., Fischer, G., & Folke, C. (2001). The causes of land-use and land-cover change: moving beyond the myths. *Global environmental change, 11*, 261-269

Lawlor, D.W. (2002). Limitation to Photosynthesis in Water‐stressed Leaves: Stomata vs. Metabolism and the Role of ATP. *Annals of Botany, 89*, 871-885

Li, R.P., Liu, X.M., & Zhou, G.S. (2006). The characteristics of Phragmites phenology in Panjin wetland and its responses to climate change. *Journal of Meteorology and Environment, 22*, 30-34

Liaoning Statistical Bureau (2013). Liaoning statistical yearbook in 2013. *China Statistical Press*

Liaw, A., & Wiener, M. (2002). Classification and regression by randomForest. *R news, 2*, 18-22

Liu, J., Dietz, T., Carpenter, S.R., Folke, C., Alberti, M., Redman, C.L., Schneider, S.H., Ostrom, E., Pell, A.N., & Lubchenco, J. (2007). Coupled human and natural systems. *AMBIO: a journal of the human environment, 36*, 639-649

Liu, J., Hull, V., Batistella, M., DeFries, R., Dietz, T., Fu, F., Hertel, T., Izaurralde, R.C., Lambin, E., & Li, S. (2013). Framing sustainability in a telecoupled world. *Ecology and Society, 18*

Liu, J., Kuang, W., Zhang, Z., Xu, X., Qin, Y., Ning, J., Zhou, W., Zhang, S., Li, R., Yan, C., Wu, S., Shi, X., Jiang, N., Yu, D., Pan, X., & Chi, W. (2014). Spatiotemporal characteristics, patterns, and causes of land-use changes in China since the late 1980s. *Journal of Geographical Sciences, 24*, 195-210

Liu, J., Liu, M., Tian, H., Zhuang, D., Zhang, Z., Zhang, W., Tang, X., & Deng, X. (2005). Spatial and temporal patterns of China's cropland during 1990–2000: An analysis based on Landsat TM data. *Remote Sensing of Environment, 98*, 442-456

Liu, J., Mooney, H., Hull, V., Davis, S.J., Gaskell, J., Hertel, T., Lubchenco, J., Seto, K.C., Gleick, P., & Kremen, C. (2015). Systems integration for global sustainability. *Science, 347*, 1258832

Lloyd, J., & Taylor, J. (1994). On the temperature dependence of soil respiration. *Functional ecology*, 315-323

Lobell, D.B., Roberts, M.J., Schlenker, W., Braun, N., Little, B.B., Rejesus, R.M., & Hammer, G.L. (2014). Greater sensitivity to drought accompanies maize yield increase in the US Midwest. *Science, 344*, 516-519

Long, D., Scanlon, B.R., Longuevergne, L., Sun, A.Y., Fernando, D.N., & Save, H. (2013). GRACE satellite monitoring of large depletion in water storage in response to the 2011 drought in Texas. *Geophysical Research Letters, 40*, 3395-3401

Luo, G., Han, Q., Zhou, D., Li, L., Chen, X., Li, Y., Hu, Y., & Li, B.L. (2012). Moderate grazing can promote aboveground primary production of grassland under water stress. *Ecological Complexity, 11*, 126-136

Luo, Y., Sherry, R., Zhou, X., & Wan, S. (2009). Terrestrial carbon‐cycle feedback to climate warming: experimental evidence on plant regulation and impacts of biofuel feedstock harvest. *GCB Bioenergy, 1*, 62-74

Maki, M., Ishiahra, M., & Tamura, M. (2004). Estimation of leaf water status to monitor the risk of forest fires by using remotely sensed data. *Remote Sensing of Environment, 90*, 441-450

Matthew, M.W., Adler-Golden, S.M., Berk, A., Richtsmeier, S.C., Levine, R.Y., Bernstein, L.S., Acharya, P.K., Anderson, G.P., Felde, G.W., & Hoke, M.L. (2000). Status of atmospheric correction using a MODTRAN4-based algorithm. In, *AeroSense 2000* (pp. 199-207): International Society for Optics and Photonics

Matthews, E., Fung, I., & Lerner, J. (1991). Methane emission from rice cultivation: Geographic and seasonal distribution of cultivated areas and emissions. *Global Biogeochemical Cycles, 5*, 3-24

Matthews, R., Wassmann, R., Knox, J., & Buendia, L. (2001). Using a crop/soil simulation model and GIS techniques to assess methane emissions from rice fields in Asia. IV. Upscaling to national levels. *Methane Emissions from Major Rice Ecosystems in Asia* (pp. 201-217): Springer

McCloy, K.R., Smith, F.R., & Robinson, M.R. (1987). Monitoring rice areas using LANDSAT MSS data. *International Journal of Remote Sensing, 8*, 741-749

McKee, T.B., Doesken, N.J., & Kleist, J. (1993). The relationship of drought frequency and duration to time scales. In, *Proceedings of the 8th Conference on Applied Climatology* (pp. 179-183): American Meteorological Society Boston, MA

McKee, T.B., Doesken, N.J., & Kleist, J. (1995). Drought monitoring with multiple time scales. In, *Ninth Conference on Applied Climatology. American Meteorological Society, Boston*

McPherson, R.A., Fiebrich, C.A., Crawford, K.C., Kilby, J.R., Grimsley, D.L., Martinez, J.E., Basara, J.B., Illston, B.G., Morris, D.A., & Kloesel, K.A. (2007). Statewide monitoring of the mesoscale environment: A technical update on the Oklahoma Mesonet. *Journal of Atmospheric and Oceanic Technology, 24*, 301-321

Medrano, H., Escalona, J., Bota, J., Gulias, J., & Flexas, J. (2002). Regulation of photosynthesis of C3 plants in response to progressive drought: stomatal conductance as a reference parameter. *Annals of Botany, 89*, 895-905

Menkhaus, D.J., St. Clair, J.S., & Ahmaddaud, A.Z. (1981). The effects of industry structure on price: a case in the beef industry. *Western Journal of Agricultural Economics*, 147-153

Migliavacca, M., Galvagno, M., Cremonese, E., Rossini, M., Meroni, M., Sonnentag, O., Cogliati, S., Manca, G., Diotri, F., Busetto, L., Cescatti, A., Colombo, R., Fava, F.,

Morra di Cella, U., Pari, E., Siniscalco, C., & Richardson, A.D. (2011). Using digital repeat photography and eddy covariance data to model grassland phenology and photosynthetic CO2 uptake. *Agricultural and Forest Meteorology, 151*, 1325-1337

Mishra, A.K., & Singh, V.P. (2010). A review of drought concepts. *Journal of Hydrology, 391*, 202-216

Moffat, A.M., Papale, D., Reichstein, M., Hollinger, D.Y., Richardson, A.D., Barr, A.G., Beckstein, C., Braswell, B.H., Churkina, G., Desai, A.R., Falge, E., Gove, J.H., Heimann, M., Hui, D., Jarvis, A.J., Kattge, J., Noormets, A., & Stauch, V.J. (2007). Comprehensive comparison of gap-filling techniques for eddy covariance net carbon fluxes. *Agricultural and Forest Meteorology, 147*, 209-232

Morison, J.I., & Morecroft, M.D. (2008). *Plant growth and climate change*. John Wiley & Sons

Mountrakis, G., Im, J., & Ogole, C. (2011). Support vector machines in remote sensing: A review. *ISPRS Journal of Photogrammetry and Remote Sensing, 66*, 247-259

Mu, Q., Zhao, M., Kimball, J.S., McDowell, N.G., & Running, S.W. (2013). A remotely sensed global terrestrial drought severity index. *Bulletin of the American Meteorological Society, 94*, 83-98

Mueller, S.A., Anderson, J.E., & Wallington, T.J. (2011). Impact of biofuel production and other supply and demand factors on food price increases in 2008. *Biomass and Bioenergy, 35*, 1623-1632

Narasimhan, B., & Srinivasan, R. (2005). Development and evaluation of Soil Moisture Deficit Index (SMDI) and Evapotranspiration Deficit Index (ETDI) for agricultural drought monitoring. *Agricultural and Forest Meteorology, 133*, 69-88

Niu, S., Sherry, R.A., Zhou, X., & Luo, Y. (2013). Ecosystem carbon fluxes in response to warming and clipping in a tallgrass prairie. *Ecosystems, 16*, 948-961

Okamoto, K., & Fukuhara, M. (1996). Estimation of paddy field area using the area ratio of categories in each mixel of Landsat TM. *International Journal of Remote Sensing, 17*, 1735-1749

Olson, J. (1992). World ecosystems (WE1. 4): Digital raster data on a 10 minute geographic 1080 (2160 grid square). *Global Ecosystem Database, Version, 1*

Osei, E., Steiner, J., & Saleh, A. (2015). Economic Viability of Beef Cattle Grazing Systems under Prolonged Drought

Otkin, J.A., Anderson, M.C., Hain, C., Mladenova, I.E., Basara, J.B., & Svoboda, M. (2013). Examining Rapid Onset Drought Development Using the Thermal Infrared–Based Evaporative Stress Index. *Journal of Hydrometeorology, 14*, 1057-1074

Otkin, J.A., Anderson, M.C., Hain, C., & Svoboda, M. (2014). Examining the relationship between drought development and rapid changes in the evaporative stress index. *Journal of Hydrometeorology, 15*, 938-956

Otkin, J.A., Anderson, M.C., Hain, C., Svoboda, M., Johnson, D., Mueller, R., Tadesse, T., Wardlow, B., & Brown, J. (2016). Assessing the evolution of soil moisture and vegetation conditions during the 2012 United States flash drought. *Agricultural and Forest Meteorology, 218-219*, 230-242

Otkin, J.A., Shafer, M., Svoboda, M., Wardlow, B., Anderson, M.C., Hain, C., & Basara, J. (2015). Facilitating the Use of Drought Early Warning Information through Interactions with Agricultural Stakeholders. *Bulletin of the American Meteorological Society*

Owensby, C.E., Ham, J.M., & Auen, L.M. (2006). Fluxes of CO 2 from grazed and ungrazed tallgrass prairie. *Rangeland Ecology & Management, 59*, 111-127

Palmer, W.C. (1965). *Meteorological drought*. US Department of Commerce, Weather Bureau Washington, DC, USA

Palmer, W.C. (1968). Keeping track of crop moisture conditions, nationwide: The new crop moisture index

Peters, A.J., Walter-Shea, E.A., Ji, L., Vina, A., Hayes, M., & Svoboda, M.D. (2002). Drought monitoring with NDVI-based standardized vegetation index. *Photogrammetric engineering and remote sensing, 68*, 71-75

Peters, E. (2003). *Propagation of drought through groundwater systems*.

Potter, C.S., Randerson, J.T., Field, C.B., Matson, P.A., Vitousek, P.M., Mooney, H.A., & Klooster, S.A. (1993). Terrestrial ecosystem production: a process model based on global satellite and surface data. *Global Biogeochemical Cycles, 7*, 811-841

Preston, T.R., & Willis, M.B. (2013). *Intensive beef production*. Elsevier

Qin, Y., Xiao, X., Dong, J., Zhou, Y., Zhu, Z., Zhang, G., Du, G., Jin, C., Kou, W., Wang, J., & Li, X. (2015). Mapping paddy rice planting area in cold temperate climate region through analysis of time series Landsat 8 (OLI), Landsat 7 (ETM+) and MODIS imagery. *ISPRS Journal of Photogrammetry and Remote Sensing, 105*, 220-233

Rao, P.P.N., & Rao, V.R. (1987). Rice crop identification and area estimation using remotely-sensed data from Indian cropping patterns. *International Journal of Remote Sensing, 8*, 639-650

Reichstein, M., Falge, E., Baldocchi, D., Papale, D., Aubinet, M., Berbigier, P., Bernhofer, C., Buchmann, N., Gilmanov, T., & Granier, A. (2005). On the separation of net ecosystem exchange into assimilation and ecosystem respiration: review and improved algorithm. *Global Change Biology, 11*, 1424-1439

Reinhart, K.O., Dangi, S.R., & Vermeire, L.T. (2016). The effect of fire intensity, nutrients, soil microbes, and spatial distance on grassland productivity. *Plant and Soil*, 1-14

Richardson, A.D., Braswell, B.H., Hollinger, D.Y., Jenkins, J.P., & Ollinger, S.V. (2009). Near-surface remote sensing of spatial and temporal variation in canopy phenology. *Ecological Applications, 19*, 1417-1428

Richardson, A.D., Jenkins, J.P., Braswell, B.H., Hollinger, D.Y., Ollinger, S.V., & Smith, M.-L. (2007). Use of digital webcam images to track spring green-up in a deciduous broadleaf forest. *Oecologia, 152*, 323-334

Richardson, A.D., Keenan, T.F., Migliavacca, M., Ryu, Y., Sonnentag, O., & Toomey, M. (2013). Climate change, phenology, and phenological control of vegetation feedbacks to the climate system. *Agricultural and Forest Meteorology, 169*, 156-173

Rogiers, N., Eugster, W., Furger, M., & Siegwolf, R. (2005). Effect of land management on ecosystem carbon fluxes at a subalpine grassland site in the Swiss Alps. *Theoretical and Applied Climatology, 80*, 187-203

Rosenberg, N.J., Epstein, D.J., Wang, D., Vail, L., Srinivasan, R., & Arnold, J.G. (1999). Possible impacts of global warming on the hydrology of the Ogallala aquifer region. *Climatic change, 42*, 677-692

Rouse Jr, J.W., Haas, R., Schell, J., & Deering, D. (1974). Monitoring vegetation systems in the Great Plains with ERTS. *NASA special publication, 351*, 309

Roy, D.P., Wulder, M., Loveland, T., Woodcock, C., Allen, R., Anderson, M., Helder, D., Irons, J., Johnson, D., & Kennedy, R. (2014). Landsat-8: Science and product vision for terrestrial global change research. *Remote Sensing of Environment, 145*, 154-172

Running, S.W., Nemani, R.R., Heinsch, F.A., Zhao, M., Reeves, M., & Hashimoto, H. (2004). A continuous satellite-derived measure of global terrestrial primary production. *Bioscience, 54*, 547-560

Salmon, J.M., Friedl, M.A., Frolking, S., Wisser, D., & Douglas, E.M. (2015). Global rain-fed, irrigated, and paddy croplands: A new high resolution map derived from remote sensing, crop inventories and climate data. *International Journal of Applied Earth Observation and Geoinformation, 38*, 321-334

Samuel, W.C., & Forbes, T.D.A. (1998). Herbage Characteristics and Performance of Steers Grazing Old World Bluestem. *Journal of Range Management, 51*, 399-407

Schmid, H.P. (1994). Source areas for scalars and scalar fluxes. *Boundary-Layer Meteorology, 67*, 293-318

Schubert, S.D., Suarez, M.J., Pegion, P.J., Koster, R.D., & Bacmeister, J.T. (2004). On the cause of the 1930s Dust Bowl. *Science, 303*, 1855-1859

Sims, D.A., Rahman, A.F., Cordova, V.D., El-Masri, B.Z., Baldocchi, D.D., Bolstad, P.V., Flanagan, L.B., Goldstein, A.H., Hollinger, D.Y., & Misson, L. (2008). A new model of gross primary productivity for North American ecosystems based solely on the enhanced vegetation index and land surface temperature from MODIS. *Remote Sensing of Environment, 112*, 1633-1646

Staff, S.S. (1999). Soil taxonomy: A basic system of soil classification for making and interpreting soil surveys. 2nd edition. *Natural Resources Conservation Service. U.S. Department of Agriculture Handbook 436*

Steiner, J. (2014). Grazing CAP newsletter August, 2014. In, *Available from: http://nebula.wsimg.com/30c933718adcb2a5e6347570dd69cfeb?AccessKeyId=989873E228CAF5DC44BB&disposition=0&alloworigin=1*

Stocker, T.F., Dahe, Q., & Plattner, G.-K. (2013). Climate Change 2013: The Physical Science Basis. *Working Group I Contribution to the Fifth Assessment Report of the Intergovernmental Panel on Climate Change. Summary for Policymakers (IPCC, 2013)*

Suyker, A.E., Verma, S.B., & Burba, G.G. (2003). Interannual variability in net CO2 exchange of a native tallgrass prairie. *Global Change Biology, 9*, 255-265

Svoboda, M., LeComte, D., Hayes, M., Heim, R., Gleason, K., Angel, J., Rippey, B., Tinker, R., Palecki, M., & Stooksbury, D. (2002). The drought monitor. *Bulletin of the American Meteorological Society, 83*, 1181-1190

Tadesse, T., Wardlow, B.D., Brown, J.F., Svoboda, M.D., Hayes, M.J., Fuchs, B., & Gutzmer, D. (2015). Assessing the Vegetation Condition Impacts of the 2011 Drought across the U.S. Southern Great Plains Using the Vegetation Drought Response Index (VegDRI). *Journal of Applied Meteorology and Climatology, 54*, 153-169

Tennakoon, S.B., Murty, V.V.N., & Eiumnoh, A. (1992). Estimation of cropped area and grain yield of rice using remote sensing data. *International Journal of Remote Sensing, 13*, 427-439

Torell, L.A., Libbin, J.D., & Miller, M.D. (1990). The market value of water in the Ogallala aquifer. *Land economics, 66*, 163-175

Tou, J.T., & Gonzalez, R.C. (1974). Pattern recognition principles. *Pattern Recognition in Physics, 1*

Tucker, C.J. (1979). Red and photographic infrared linear combinations for monitoring vegetation. *Remote sensing of Environment, 8*, 127-150

Twidwell, D., Rogers, W.E., Fuhlendorf, S.D., Wonkka, C.L., Engle, D.M., Weir, J.R., Kreuter, U.P., & Taylor, C.A. (2013). The rising Great Plains fire campaign: citizens' response to woody plant encroachment. *Frontiers in Ecology and the Environment, 11*, e64-e71

Tyler, J.L., Salmon, J.M., & Holly, K.G. (2015). Cropland expansion outpaces agricultural and biofuel policies in the United States. *Environmental Research Letters, 10,* 044003

Valkó, O., Török, P., Deák, B., & Tóthmérész, B. (2014). Review: Prospects and limitations of prescribed burning as a management tool in European grasslands. *Basic and Applied Ecology, 15,* 26-33

Vermote, E., & Vermeulen, A. (1999). Atmospheric correction algorithm: spectral reflectances (MOD09). *ATBD version, 4*

Vitali, A., Felici, A., Esposito, S., Bernabucci, U., Bertocchi, L., Maresca, C., Nardone, A., & Lacetera, N. (2015). The effect of heat waves on dairy cow mortality. *Journal of Dairy Science, 98,* 4572-4579

Wagle, P., & Kakani, V.G. (2014). Seasonal variability in net ecosystem carbon dioxide exchange over a young Switchgrass stand. *GCB Bioenergy, 6,* 339-350

Wagle, P., Xiao, X., & Suyker, A.E. (2015). Estimation and analysis of gross primary production of soybean under various management practices and drought conditions. *ISPRS Journal of Photogrammetry and Remote Sensing, 99,* 70-83

Wagle, P., Xiao, X., Torn, M.S., Cook, D.R., Matamala, R., Fischer, M.L., Jin, C., Dong, J., & Biradar, C. (2014). Sensitivity of vegetation indices and gross primary production of tallgrass prairie to severe drought. *Remote Sensing of Environment, 152,* 1-14

Wan, J., Qu, M., Hao, X., Motha, R., & Qu, J.J. (2015). Assessing the Impact of Year 2012 Drought on Corn Yield in the US Corn Belt Using Precipitation Data. *Journal of Earth Science and Engineering, 5,* 333-337

Wan, Z., & Dozier, J. (1996). A generalized split-window algorithm for retrieving land-surface temperature from space. *Geoscience and Remote Sensing, IEEE Transactions on, 34,* 892-905

Wan, Z., Wang, P., & Li, X. (2004). Using MODIS Land Surface Temperature and Normalized Difference Vegetation Index products for monitoring drought in the southern Great Plains, USA. *International Journal of Remote Sensing, 25,* 61-72

Wan, Z., Zhang, Y., Zhang, Q., & Li, Z.-l. (2002). Validation of the land-surface temperature products retrieved from Terra Moderate Resolution Imaging Spectroradiometer data. *Remote Sensing of Environment, 83*, 163-180

Wang, J., Xiao, X., Qin, Y., Dong, J., Zhang, G., Kou, W., Jin, C., Zhou, Y., & Zhang, Y. (2015). Mapping paddy rice planting area in wheat-rice double-cropped areas through integration of Landsat-8 OLI, MODIS, and PALSAR images. *Sci. Rep., 5*

Wardlow, B.D., Anderson, M.C., & Verdin, J.P. (2012a). *Remote sensing of drought: Innovative monitoring approaches*. CRC Press

Wardlow, B.D., Tadesse, T., Brown, J.F., Callahan, K., Swain, S., & Hunt, E. (2012b). The Vegetation Drought Response Index (VegDRI): An integration of satellite, climate, and biophysical data

Weaver, S., Baxter, S., & Harnos, K. (2016). Regional Changes in the Interannual Variability of U.S. Warm Season Precipitation. *Journal of Climate, 29*, 5157-5173

West, J. (2003). Effects of heat-stress on production in dairy cattle. *Journal of Dairy Science, 86*, 2131-2144

Wilhite, D.A. (2005). *Drought and water crises: science, technology, and management issues*. CRC Press

Wilhite, D.A., Svoboda, M.D., & Hayes, M.J. (2007). Understanding the complex impacts of drought: a key to enhancing drought mitigation and preparedness. *Water Resources Management, 21*, 763-774

Wilson, D.M., Dalluge, D.L., Rover, M., Heaton, E.A., & Brown, R.C. (2013). Crop management impacts biofuel quality: influence of switchgrass harvest time on yield, nitrogen and ash of fast pyrolysis products. *Bioenergy Research, 6*, 103-113

Worster, D. (1979). *Dust bowl: the southern plains in the 1930s*. Oxford University Press

Wu, C., Niu, Z., & Gao, S. (2010). Gross primary production estimation from MODIS data with vegetation index and photosynthetically active radiation in maize. *Journal of Geophysical Research: Atmospheres, 115*

Xiao, X., Boles, S., Frolking, S., Salas, W., Moore, B., Li, C., He, L., & Zhao, R. (2002a). Observation of flooding and rice transplanting of paddy rice fields at the site to landscape scales in China using VEGETATION sensor data. *International Journal of Remote Sensing, 23*, 3009-3022

Xiao, X., Boles, S., Frolking, S., Salas, W., Moore Iii, B., Li, C., He, L., & Zhao, R. (2002b). Landscape-scale characterization of cropland in China using Vegetation and Landsat TM images. *International Journal of Remote Sensing, 23*, 3579-3594

Xiao, X., Boles, S., Frolking, S., Salas, W., Moore Iii, B., Li, C., He, L., & Zhao, R. (2002c). Observation of flooding and rice transplanting of paddy rice fields at the site to landscape scales in China using VEGETATION sensor data. *International Journal of Remote Sensing, 23*, 3009-3022

Xiao, X., Hollinger, D., Aber, J., Goltz, M., Davidson, E.A., Zhang, Q., & Moore Iii, B. (2004a). Satellite-based modeling of gross primary production in an evergreen needleleaf forest. *Remote Sensing of Environment, 89*, 519-534

Xiao, X.M., Boles, S., Frolking, S., Li, C.S., Babu, J.Y., Salas, W., & Moore, B. (2006). Mapping paddy rice agriculture in South and Southeast Asia using multi-temporal MODIS images. *Remote Sensing of Environment, 100*, 95-113

Xiao, X.M., Boles, S., Liu, J.Y., Zhuang, D.F., Frolking, S., Li, C.S., Salas, W., & Moore, B. (2005). Mapping paddy rice agriculture in southern China using multi-temporal MODIS images. *Remote Sensing of Environment, 95*, 480-492

Xiao, X.M., Hollinger, D., Aber, J., Goltz, M., Davidson, E.A., Zhang, Q.Y., & Moore, B. (2004b). Satellite-based modeling of gross primary production in an evergreen needleleaf forest. *Remote Sensing of Environment, 89*, 519-534

Xiao, X.M., Zhang, Q.Y., Braswell, B., Urbanski, S., Boles, S., Wofsy, S., Berrien, M., & Ojima, D. (2004c). Modeling gross primary production of temperate deciduous broadleaf forest using satellite images and climate data. *Remote Sensing of Environment, 91*, 256-270

Xie, Y., Sha, Z., & Yu, M. (2008). Remote sensing imagery in vegetation mapping: a review. *Journal of Plant Ecology, 1*, 9-23

Xu, L., Zhang, Y., Pengshi, C., & Mao, L. (2009). Analysis on the Changing Characteristics and Influencing Factors of Panjin Wetland During the Past 20 Years [J]. *Journal of Natural Resources, 24*, 483-490

Yang, S.B., Shen, S.H., Li, B.B., Le Toan, T., & He, W. (2008). Rice mapping and monitoring using ENVISAT ASAR data. *Ieee Geoscience and Remote Sensing Letters, 5*, 108-112

Yu, X.F., & Zhuang, D.F. (2006). Monitoring Forest Phenophases of Northeast China based on MODIS NDVI Data. *Resources Science, 28*, 111-117

Yuan, W., Liu, S., Zhou, G., Zhou, G., Tieszen, L.L., Baldocchi, D., Bernhofer, C., Gholz, H., Goldstein, A.H., & Goulden, M.L. (2007). Deriving a light use efficiency model from eddy covariance flux data for predicting daily gross primary production across biomes. *Agricultural and Forest Meteorology, 143*, 189-207

Zargar, A., Sadiq, R., Naser, B., & Khan, F.I. (2011). A review of drought indices. *Environmental Reviews, 19*, 333-349

Zeeman, M.J., Hiller, R., Gilgen, A.K., Michna, P., Plüss, P., Buchmann, N., & Eugster, W. (2010). Management and climate impacts on net CO2 fluxes and carbon budgets of three grasslands along an elevational gradient in Switzerland. *Agricultural and Forest Meteorology, 150*, 519-530

Zhang, G., Xiao, X., Dong, J., Kou, W., Jin, C., Qin, Y., Zhou, Y., Wang, J., Menarguez, M.A., & Biradar, C. (2015). Mapping paddy rice planting areas through time series analysis of MODIS land surface temperature and vegetation index data. *ISPRS Journal of Photogrammetry and Remote Sensing, 106*, 157-171

Zhang, Q., Cheng, Y.-B., Lyapustin, A.I., Wang, Y., Xiao, X., Suyker, A., Verma, S., Tan, B., & Middleton, E.M. (2014a). Estimation of crop gross primary production (GPP): I. impact of MODIS observation footprint and impact of vegetation BRDF characteristics. *Agricultural and Forest Meteorology, 191*, 51-63

Zhang, Y., Wang, C., Wu, J., Qi, J., & Salas, W.A. (2009). Mapping paddy rice with multitemporal ALOS/PALSAR imagery in southeast China. *International Journal of Remote Sensing, 30*, 6301-6315

Zhang, Z., Wang, X., Zhao, X., Liu, B., Yi, L., Zuo, L., Wen, Q., Liu, F., Xu, J., & Hu, S. (2014b). A 2010 update of National Land Use/Cover Database of China at 1:100000

scale using medium spatial resolution satellite images. *Remote Sensing of Environment, 149*, 142-154

Zhou, Y., Xiao, X., Qin, Y., Dong, J., Zhang, G., Kou, W., Jin, C., Wang, J., & Li, X. (2016). Mapping paddy rice planting area in rice-wetland coexistent areas through analysis of Landsat 8 OLI and MODIS images. *International Journal of Applied Earth Observation and Geoinformation, 46*, 1-12

Zhuang, Q., Melack, J.M., Zimov, S., Walter, K.M., Butenhoff, C.L., & Khalil, M.A.K. (2009). Global methan emissions from wetlands, rice paddies, and lakes. *Eos, Transactions American Geophysical Union, 90*, 37-38

Ziolkowska, J. (2016). Socio-Economic Implications of Drought in the Agricultural Sector and the State Economy. *Economies*, *4*, 19